Robust Wireless Skin Sensor Networks for Long-Term Fatigue Crack Monitoring of Bridges (Phase I)

Final Report
May 2024

IOWA STATE UNIVERSITY
Institute for Transportation

Sponsored by
Iowa Department of Transportation
(InTrans Project 20-736)
Transportation Pooled Fund TPF-5(449)
Federal Highway Administration

About the Institute for Transportation

The mission of the Institute for Transportation (InTrans) at Iowa State University is to save lives and improve economic vitality through discovery, research innovation, outreach, and the implementation of bold ideas.

Iowa State University Nondiscrimination Statement

Iowa State University does not discriminate on the basis of race, color, age, ethnicity, religion, national origin, pregnancy, sexual orientation, gender identity, genetic information, sex, marital status, disability, or status as a US veteran. Inquiries regarding nondiscrimination policies may be directed to the Office of Equal Opportunity, 3410 Beardshear Hall, 515 Morrill Road, Ames, Iowa 50011, telephone: 515-294-7612, hotline: 515-294-1222, email: eooffice@iastate.edu.

Disclaimer Notice

The contents of this report reflect the views of the authors, who are responsible for the facts and the accuracy of the information presented herein. The opinions, findings and conclusions expressed in this publication are those of the authors and not necessarily those of the sponsors.

The sponsors assume no liability for the contents or use of the information contained in this document. This report does not constitute a standard, specification, or regulation.

The sponsors do not endorse products or manufacturers. Trademarks or manufacturers' names appear in this report only because they are considered essential to the objective of the document.

Quality Assurance Statement

The Federal Highway Administration (FHWA) provides high-quality information to serve Government, industry, and the public in a manner that promotes public understanding. Standards and policies are used to ensure and maximize the quality, objectivity, utility, and integrity of its information. The FHWA periodically reviews quality issues and adjusts its programs and processes to ensure continuous quality improvement.

Iowa DOT Statements

Federal and state laws prohibit employment and/or public accommodation discrimination on the basis of age, color, creed, disability, gender identity, national origin, pregnancy, race, religion, sex, sexual orientation or veteran's status. If you believe you have been discriminated against, please contact the Iowa Civil Rights Commission at 800-457-4416 or the Iowa Department of Transportation affirmative action officer. If you need accommodations because of a disability to access the Iowa Department of Transportation's services, contact the agency's affirmative action officer at 800-262-0003.

The preparation of this report was financed in part through funds provided by the Iowa Department of Transportation through its "Second Revised Agreement for the Management of Research Conducted by Iowa State University for the Iowa Department of Transportation" and its amendments.

The opinions, findings, and conclusions expressed in this publication are those of the authors and not necessarily those of the Iowa Department of Transportation or the U.S. Department of Transportation Federal Highway Administration.

Technical Report Documentation Page

1. Report No. InTrans Project 20-736	**2. Government Accession No.**	**3. Recipient's Catalog No.**

4. Title and Subtitle Robust Wireless Skin Sensor Networks for Long-Term Fatigue Crack Monitoring of Bridges (Phase I)	**5. Report Date** May 2024
	6. Performing Organization Code
7. Author(s) Simon Laflamme, Ph.D. (orcid.org/0000-0001-5666-3215), Han Liu, Ph.D. (orcid.org/0000-0003-3057-522X), Jian Li, Ph.D., P.E. (orcid.org/0000-0003-3439-7539), Caroline Bennett, Ph.D., P.E. (orcid.org/0000-0002-2713-0011), William Collins, Ph.D., P.E. (orcid.org/0000-0002-2835-6389), Austin R. J. Downey, Ph.D. (/orcid.org/0000-0002-5524-2416), and Hongki Jo, Ph.D. (orcid.org/0000-0001-5056-1154)	**8. Performing Organization Report No.** InTrans Project 20-736
9. Performing Organization Name and Address Department of Civil, Construction and Environmental Engineering Iowa State University 813 Bissell Road Ames, IA 50011	**10. Work Unit No. (TRAIS)**
	11. Contract or Grant No.
12. Sponsoring Organization Name and Address Iowa Department of Transportation Transportation Pooled Fund TPF-5(449) 800 Lincoln Way Ames, IA 50010 Federal Highway Administration 1200 New Jersey Avenue, SE Washington, DC 20590	**13. Type of Report and Period Covered** Final Report
	14. Sponsoring Agency Code TPF-5(449)

15. Supplementary Notes

Visit https://intrans.iastate.edu for color pdfs of this and other research reports.

16. Abstract

In this project, we extended research and development of a novel sensing technology previously investigated in the pooled fund initiative TPF-5(328). The technology is a soft elastomeric capacitor (SEC) developed at Iowa State University. It is a geometrically large strain gauge, and its measurement principle is based on transducing changes in strain into measurable changes in capacitance. Arranged in a network configuration, it can monitor strain over a large area at a given resolution. The SEC technology is inexpensive and easy to deploy and is therefore highly scalable. It follows that the technology can be used to discover new fatigue cracks and to track and quantify damage, an important challenge to numerous departments of transportation.

The overarching objective of our project was to enable large-scale deployments in the United States by addressing further essential development needs uncovered during the previous research to achieve more robust, accurate, and flexible crack monitoring using the wireless skin sensor network. In particular, within this three-year research phase (Phase 1), we have (1) designed the SEC for robust long-term field deployment, (2) provided the technology with improved wireless and augmented sensing capabilities, (3) formulated a crack detection algorithm that accommodates diverse structural configurations and can be directly used by engineers for decision making, (4) improved damage quantification capabilities for complex geometries and composite materials, and (5) validated and demonstrated the improved version of the wireless crack sensing technology on a bridge in the field through long-term deployment.

17. Key Words fatigue cracking—fillet welds—soft elastomeric capacitor—steel bridge—strain sensing—structural health monitoring—wireless sensing	**18. Distribution Statement** No restrictions.

19. Security Classification (of this report) Unclassified.	**20. Security Classification (of this page)** Unclassified.	**21. No. of Pages** 127	**22. Price** NA

Form DOT F 1700.7 (8-72) **Reproduction of completed page authorized**

ROBUST WIRELESS SKIN SENSOR NETWORKS FOR LONG-TERM FATIGUE CRACK MONITORING OF BRIDGES (PHASE I)

Final Report
May 2024

Principal Investigator
Simon Laflamme, Professor, Iowa State University

Co-Principal Investigators
Jian Li, Associate Professor, The University of Kansas
Caroline Bennett, Associate Professor, The University of Kansas
William Collins, Associate Professor, The University of Kansas
The University of Kansas, The University of Kansas
Austin R. J. Downey, University of South Carolina
Hongki Jo, The University of Arizona

Research Assistants
Han Liu, Sdiq Anwar Taher, Rushil Mojidra, Emmanuel Ogunniyi,
Jong-Hyun Jeong, and Tahsin Afroz Hoque Nishat

Authors
Simon Laflamme, Han Liu, Jian Li, Caroline Bennett,
William Collins, Austin R. J. Downey, and Hongki Jo

Sponsored by
Federal Highway Administration
Transportation Pooled Fund TPF-5(449)

Preparation of this report was financed in part
through funds provided by the Iowa Department of Transportation
through its Research Management Agreement with the
Institute for Transportation
(InTrans Project 17-629)

A report from
Institute for Transportation
Iowa State University
2711 South Loop Drive, Suite 4700
Ames, IA 50010-8664
Phone: 515-294-8103 / Fax: 515-294-0467
https://intrans.iastate.edu

TABLE OF CONTENTS

LIST OF FIGURES

LIST OF TABLES

ACKNOWLEDGMENTS

The research team would like to acknowledge the Federal Highway Administration (FHWA) for sponsoring this Transportation Pooled Fund study: TPF-5(449). The authors would also like to thank the state pooled fund department of transportation (DOT) partners for their support:

- Iowa DOT (lead state)
- Kansas DOT (KDOT)
- South Carolina DOT (SCDOT)
- North Carolina DOT (NCDOT)

The authors are especially grateful to the lead agency, Iowa DOT, for sponsoring this research and the FHWA for state planning and research (SPR) funds used for this project.

The authors would also like to thank the representatives from state DOTs for providing valuable feedback through emails and our regular quarterly project meetings, including Michael Todsen (Iowa DOT), Mark Hurt (KDOT), David Snoke (NCDOT), Rodrick Tucker (NCDOT), and Hoda Azari (FHWA).

The authors also want to thank Doug Wood, Owen Steffens, and Andrew Goreczny at Iowa State University for their assistance on the experimental work in this project.

EXECUTIVE SUMMARY

In this project, we extended research and development of a novel sensing technology previously investigated in the pooled fund initiative TPF-5(328). The technology is a soft elastomeric capacitor (SEC) developed at Iowa State University. It is a geometrically large strain gauge, and its measurement principle is based on transducing changes in strain into measurable changes in capacitance. Arranged in a network configuration, it can monitor strain over a large area at a given resolution. The SEC technology is inexpensive and easy to deploy and is therefore highly scalable. It follows that the technology can be used to discover new fatigue cracks and to track and quantify damage, an important challenge to numerous departments of transportation.

The overarching objective of our project was to enable large-scale deployments in the United States by addressing further essential development needs uncovered during the previous research to achieve more robust, accurate, and flexible crack monitoring using the wireless skin sensor network. In particular, within this three-year research phase (Phase 1), we have (1) designed the SEC for robust long-term field deployment, (2) provided the technology with improved wireless and augmented sensing capabilities, (3) formulated a crack detection algorithm that accommodates diverse structural configurations and can be directly used by engineers for decision making, (4) improved damage quantification capabilities for complex geometries and composite materials, and (5) validated and demonstrated the improved version of the wireless crack sensing technology on a bridge in the field through long-term deployment.

CHAPTER 1: INTRODUCTION

Fatigue Crack on Steel Bridges

Fatigue is the weakening of steel materials or the accumulation of damage at a localized region caused by cyclic loading or repeatedly applied loads. Fatigue-induced cracks are of great concern to departments of transportation (DOTs). A significant number of bridges in the country are fracture-critical bridges that are vulnerable to fatigue cracks due to the brittle nature of their failure modes. In 2020, 37% of bridges totaling 231,000 in the United States needed repair work, and 7.5% of the nation's 617,000 bridges subjected to federal inspection requirements were rated in poor condition and classified as structurally deficient (ARTBA 2020, ASCE 2021).

Challenges for Fatigue Detection and Monitoring

The timely discovery and monitoring of fatigue cracks in steel structures is an important task to ensure their structural integrity. Visual inspection is currently the most popular approach used in detecting fatigue cracks, but the process is time-consuming, labor-intensive, and reliant on the inspector's judgment (Campbell et al. 2020). A recent study revealed that early-stage cracks have a low probability of detection through visual inspection (Campbell et al. 2021). Various nondestructive evaluation (NDE) techniques for crack detection and quantification have been proposed to assist visual inspections. Examples include ultrasonic (Geathers et al. 2015, Liu et al. 2017), magnetic particle (Zolfaghari et al. 2018), acoustic emission (Pascoe et al. 2018, Ren et al. 2020), computer vision (Kong and Li 2019, Dellenbaugh et al. 2020), and piezoelectric-based (Yu et al. 2016, Wang et al. 2020, Roy et al. 2021) methods. Aside from piezoelectric-based methods that may be applied more permanently, NDE methods are typically temporary and conducted manually over limited components and sections of the structure, thus spatiotemporally limiting crack discovery. Automatic fatigue crack detection using commercial sensing technologies is difficult due to the highly localized nature of crack monitoring sensors and the randomness of crack initiation and propagation.

To improve accuracy and prevent catastrophic failures, a more effective and efficient technique for monitoring fatigue cracks is critical to ensure timely actions. To this end, structural health monitoring (SHM) has attracted significant attention since it can provide continuous, reliable, and accurate monitoring at a lower cost. In particular, by integrating sensors for measuring structural responses, data processing and modeling algorithms for diagnosing structural conditions, and presenting a prognosis of future status, SHM has shown great success in global structural assessment through system/modal identification (Pakzad et al. 2008), model updating (Mottershead et al. 2011), and input and state estimation (Taher et al. 2021) using acceleration and strain measurements. However, SHM in field applications, particularly for local damage such as fatigue crack monitoring, is still lacking due to the lack of appropriate sensors, its integration with energy-efficient wireless sensing platforms for long-term autonomous monitoring, and effective algorithms for the prognosis and diagnosis of local fatigue damage.

Strain-Based Crack Sensing Technology

Strain-based crack sensing relies on the fact that when a material undergoes deformation due to external forces or internal stresses, it alters the strain distribution in the material. Therefore, direct strain measurement can be used for effective crack sensing, especially for scenarios where a crack occurs underneath or in close proximity to the sensor, where an abrupt change in strain at the localized area can be detected when a crack begins to form or propagate within the structure. Strain sensors, often in the form of traditional metal foil strain gauges (Tikka et al. 2003) or fiber optic sensors (Casas and Cruz 2003, Minardo et al. 2012), are commonly used techniques that are strategically deployed on the surface of the monitored structure for strain sensing. However, strain sensors present limitations for monitoring cracks across a large-scale structure because of their relatively small footprint, which hinders their ability to cover adequate crack-prone areas, and the structure's limited ductility, which can cause failure under the extreme strain demands due to crack formation (Kong et al. 2017a, Kumar et al. 2021). Therefore, it is difficult to use them to successfully locate new crack formation or growth with acceptable confidence, and developing innovative technologies with broader coverage and enhanced durability is essential to overcome these limitations and ensure effective monitoring of structural health.

Capacitance Measurement Methods

Capacitance measurement methods are integral to strain-based crack sensing, offering precise monitoring capabilities by transferring mechanical strain into a measurable change in electric properties. These methods typically involve using parallel plate capacitive sensors where the capacitance changes when the distance between the plates change, making the sensors capable of detecting minor variations in capacitance resulting from structural deformations. Therefore, the strain variation caused by the opening and closing of the crack can be monitored by deploying these capacitive sensors onto the surface of a structure. Compared to the metal foil strain gauges and fiber optic sensors, capacitance-based crack sensing is preferred due to its higher sensitivity—making it more effective in detecting cracks in metallic and composite materials—enhanced durability, nonintrusive properties, ease of installation, and cost effectiveness. Currently, the resistor-capacitor (RC) circuit suitable for wide-range capacitive sensor interfaces and the Wheatstone bridge-based sensing approach, which measures the electrical capacitance by balancing two legs of a bridge circuit, are the two main techniques available for measuring capacitance. However, the RC circuit usually requires high performance, high frequency, and an extremely low-jitter clock for small range capacitance variation measurement (Mantenuto et al. 2014), and the complexity of calibration and the demand of low-level capacitance measurement with a high sampling frequency in wireless communication hinder their application in civil infrastructure monitoring applications.

Therefore, as part of a previous related project, we developed a capacitance-based flexible strain sensor technology based on a soft elastomeric capacitor (SEC) for SHM and investigated an alternating current (AC) bridge-based method to transform the strain-induced dynamic capacitance changes in the SEC into analog voltage signals.

Sensing Skin Technology

It is possible to automate the fatigue crack monitoring process using SHM technology. In particular, data collected by strain sensors can be directly related to fatigue crack activities by capturing surface deformations caused by cracking (Burton et al. 2017, Jo et al. 2013). Off-the-shelf strain sensors are typically small and their deployment is too spatially localized, which poses challenges to reliably locate new crack formation or growth with acceptable confidence. To address these issues, researchers have recently proposed large-area electronics (LAE) that can be deployed as a dense sensor network, enabling the discovery of local damage over a global area. Examples of LAE, or “sensing skin,” applications to strain and fatigue crack monitoring include a carbon nanotube (CNT)-based adhesive film (Sánchez-Romate et al. 2020), CNT-based sensing sheets (Dai et al. 2015, Ahmed et al. 2020), a flexible polyimide sheet of strain gauges (Yao and Glisic 2015, Glišić et al. 2016), and a stretchable guided wave sensor network (Wang et al. 2022).

In an effort to produce a large-scale deployable sensing skin system, we previously developed a sensing skin solution. Our previously developed sensing skin is formed by an array of SECs, with each SEC acting as a capacitive-based strain gauge. The SEC technology has been proposed as a low-cost alternative to traditional strain gauges while allowing for a broader range of applications. The SECs are flexible and can be modeled with different dimensions based on the monitored structure. Experimental tests showed that the sensing skin can measure large strains (20%) and has the resolution (25 με) necessary for crack detection. As part of the current research, we developed a new generation of SEC technology by corrugating the top surface of the dielectric layer to tune the in-plane stiffness, lowering the sensor’s Poisson’s ratio and improving its mechanical stability. Additionally, we evaluated the sensing performance of the corrugated SEC (cSEC) through a series of laboratory tests and applied a dense cSEC sensor network as a sensing skin for long-term fatigue crack monitoring on steel bridges in this project.

Wireless Sensing Technology

Thin film-based flexible strain sensors have various advantages for SHM because of their capability to sustain large deformations and cover large surface areas of structures, making them ideal candidates for applications with complex geometries and structural crack monitoring. Experimental works on the SEC and cSEC used a wired commercial capacitance measurement device termed PCAP (model PCAP02). However, the use of a wired data acquisition (DAQ) system impedes the practicality of any field application because of the added difficulties of installation, costly cabling, inefficient data transmission, high energy dissipation, and poor accessibility (Spencer et al. 2017). Wireless smart sensors (WSS) are an attractive solution for SHM in that they enable wireless communication among sensor nodes distributed over large-scale structural systems without costly cabling (Spencer et al. 2004). Many WSS platforms have been developed and applied for SHM applications such as the Mica series, iMote series, and Xnode. However, capacitance-based strain sensing methods have not benefited from these advantages of WSS networks for SHM because of the lack of accompanying sensor boards that can interact with the wireless sensing platforms to achieve diverse sensing capabilities.

To address this issue, we previously developed an AC bridge-based method to transform the strain-induced dynamic capacitance changes in the SEC into analog voltage signals (Jeong et al. 2018a). Previous experiments have verified the capability of the SEC and the AC bridge-based signal converter for structural strain sensing applications. However, the careful manipulation requirements for precise AC bridge balancing, signal amplification control, and shunt calibration limits its practical use for full-scale SHM in field conditions. In this project, we developed a low-cost microcontroller-based c-strain sensor board for wireless SHM applications, which interfaces with the Xnode wireless sensor platform for basic capacitance measurement while enabling automated AC bridge balancing, amplification, and shunt calibration.

Research Objectives

The prior pooled fund initiative project TPF-5(328) demonstrated the capability of the sensing skin technology both in a laboratory environment and in the field and concluded further essential development was needed in order to fully enable the technology for a nationwide deployment. In this project, we extended the research and development of the previously investigated novel sensing technology. The technology is a new generation of SEC developed at Iowa State University. It is a geometrically large strain gauge, and its measurement principle is based on transducing changes in strain into measurable changes in capacitance. Arranged in a network configuration, it can monitor strain over a large area at a given resolution. The SEC technology is inexpensive and easy to deploy and is therefore highly scalable. The technology can be used to discover new fatigue cracks and track and quantify damage, a significant challenge for numerous DOTs.

The overarching objective of this project was to enable large-scale deployments of the new technology in the United States by addressing further essential development needs uncovered during the previous research to achieve more robust, accurate, and flexible crack monitoring using the wireless skin sensor network. In particular, within this three-year research phase (Phase I), we (1) designed the SEC for robust long-term field deployment, (2) provided the technology with improved wireless and augmented sensing capabilities, (3) formulated a crack detection algorithm that accommodates more diverse structural configurations and can be directly used by engineers for decision making, (4) improved fatigue damage quantification capabilities for complex geometries and composite materials, and (5) validated and demonstrated the improved version of the wireless crack sensing technology on a bridge in the field through long-term deployment.

Project Video

A YouTube video titled “Pooled Fund Project - Fatigue Crack Monitoring” has been posted to provide a visual demonstration of Phase I, including field deployment, the sensing mechanism, laboratory tests, tests on concrete, and sensor fabrication. The video is available at https://www.youtube.com/watch?v=U9LEglPvp3g.

Organization of the Report

This report is organized as follows:

- Chapter 2 demonstrates the sensing skin technologies proposed for fatigue crack monitoring.
- Chapter 3 illustrates and experimentally validates the capability of cSEC for monitoring fatigue crack growth through small-scale compact tension (C(T)) specimens, for angular rotation sensing in steel components, and for fatigue cracks sensing on fillet welds.
- Chapter 4 illustrates the development of a wireless capacitive sensing board for high-sensitive capacitive strain sensing.
- Chapter 5 validates the entire monitoring system through a field deployment on a steel bridge.
- Chapter 6 concludes the report.

Figure 1.1 illustrates the organization of this report.

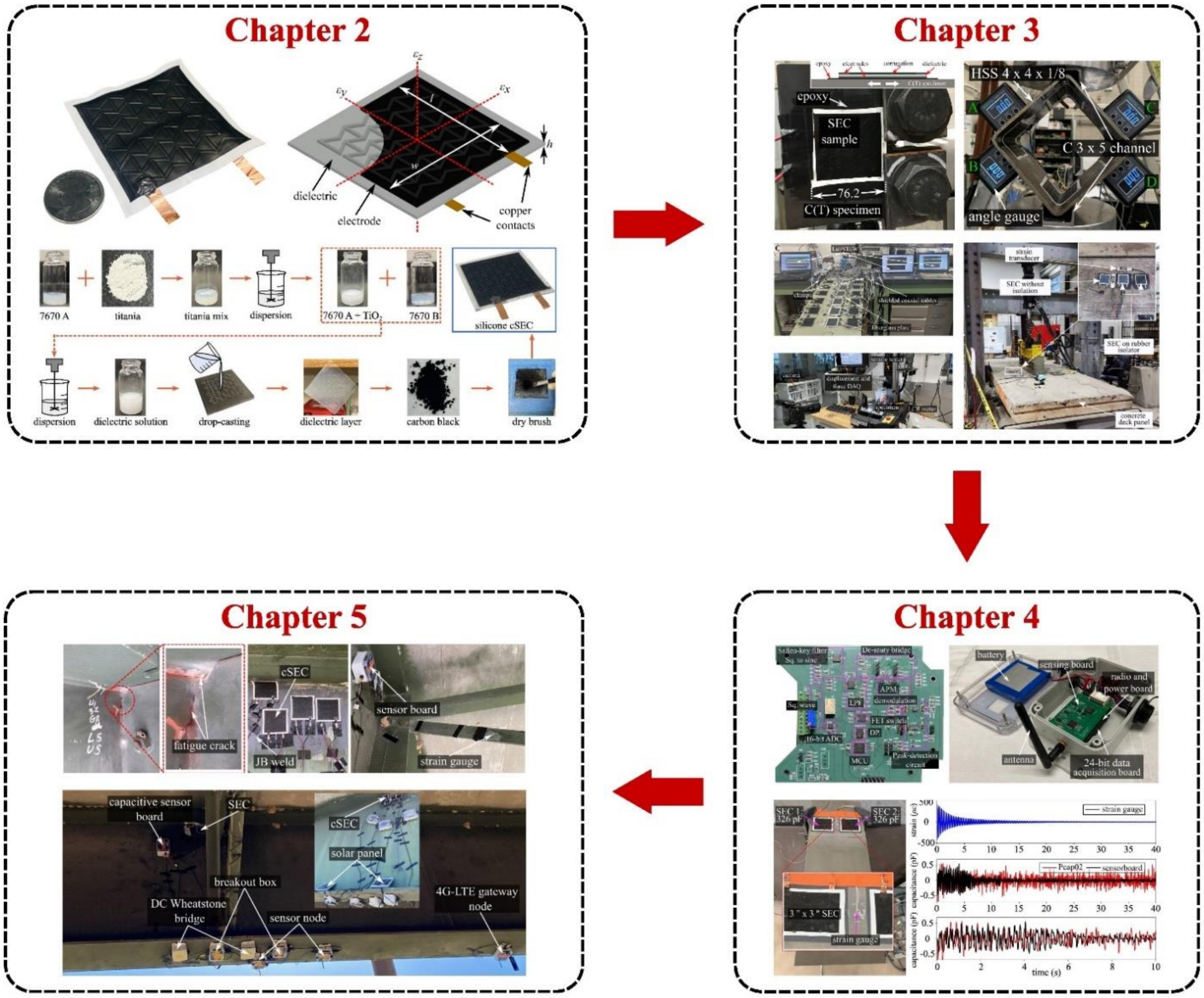

Figure 1.1. Organization of Chapters 2 through 5 of the report

The content of each chapter is constructed from information already digested by the scientific and engineering community, as summarized below.

Chapter 2 is extracted from the following publications:

- Liu, H., S. Laflamme, J. Li, C. Bennett, W. Collins, A. Downey, P. Ziehl, and H. Jo. 2021. Investigation of Surface Textured Sensing Skin for Fatigue Crack Localization and Quantification. *Smart Materials and Structures*, Vol. 30, No. 10.
- Liu, H., S. Laflamme, and M. Kollosche. 2023. Paintable Silicone-Based Corrugated Soft Elastomeric Capacitor for Area Strain Sensing. *Sensors*, Vol. 23, No. 13.
- Liu, H., M. Kollosche, S. Laflamme, and D. Clarke. 2023.Multifunctional Soft Stretchable Strain Sensor for Complementary Optical and Electrical Sensing of Fatigue Cracks. *Smart Materials and Structures*, Vol. 32, No.4.
- Ogunniyi, E. A., H. Liu, A. R. Downey, S. Laflamme, J. Li, C. Bennett, W. Collins, H. Jo, and P. Ziehl. 2023. Soft Elastomeric Capacitors with an Extended Polymer Matrix for Strain Sensing on Concrete. *Sensors and Smart Structures Technologies for Civil, Mechanical, and Aerospace Systems 2023* (Vol. 12486, pp. 262–270). SPIE, Bellingham, WA.

Chapter 3 is extracted from the following publications:

- Liu, H., S. Laflamme, J. Li, C. Bennett, W. Collins, A. Downey, P. Ziehl, and H. Jo. 2021. Investigation of Surface Textured Sensing Skin for Fatigue Crack Localization and Quantification. *Smart Materials and Structures*, Vol. 30, No. 10.
- Liu, H., S. Laflamme, J. Li, C. Bennett, W. N. Collins, A. Downey, P. Ziehl, and H. Jo. 2021. Soft Elastomeric Capacitor for Angular Rotation Sensing in Steel Components. *Sensors*, Vol. 21, No. 21, Article No. 7017.
- Liu, H., S. Laflamme, J. Li, C. Bennett, W. N. Collins, D. J. Eisenmann, A. Downey, P. Ziehl, and H. Jo. 2022. Investigation of Textured Sensing Skin for Monitoring Fatigue Cracks on Fillet Welds. *Measurement Science and Technology*, Vol. 33, No. 8.

Chapter 4 is extracted from the following publication:

- Jeong, J.-H., H. Jo, S. Laflamme, J. Li, A. Downey, C. Bennett, W. Collins, S. A. Taher, H. Liu, and H.-J. Jung. 2022. Automatic Control of AC Bridge-Based Capacitive Strain Sensor Interface for Wireless Structural Health Monitoring. *Measurement*, Vol. 202.

Chapter 5 is extracted from the following publication:

- Taher, S. A., J. Li, J.-H. Jeong, S. Laflamme, H. Jo, C. Bennett, W. Collins, and A. R. Downey. 2022. Structural Health Monitoring of Fatigue Cracks for Steel Bridges with Wireless Large-Area Strain Sensors. *Sensors*, Vol. 22, No. 14.

CHAPTER 2: SENSING SKIN TECHNOLOGY

Overview

The concept of using a capacitive-based sensing skin for SHM applications was proposed more than a decade ago. The sensing principle is to form a dense sensor network by assembling numerous sensors in a matrix form, with each sensor acting as an independent strain gauge, resulting in a sensor network measuring local strain information over a global area analogous to biological skin. This chapter introduces the three different SEC-based sensing skin technologies we developed for fatigue crack monitoring, along with the future direction in SEC sensing.

SEC

The SEC is a robust large-area capacitor that transduces strain into a measurable change in capacitance. Its design, fabrication, and sensing principle are described in detail in Laflamme et al. (2013). Figure 2.1a presents a square-shaped SEC with a size of 76 mm × 76 mm. The technology is a flexible and stretchable parallel capacitor constituted by a dielectric layer sandwiched between conductive plates, as shown in Figure 2.1b.

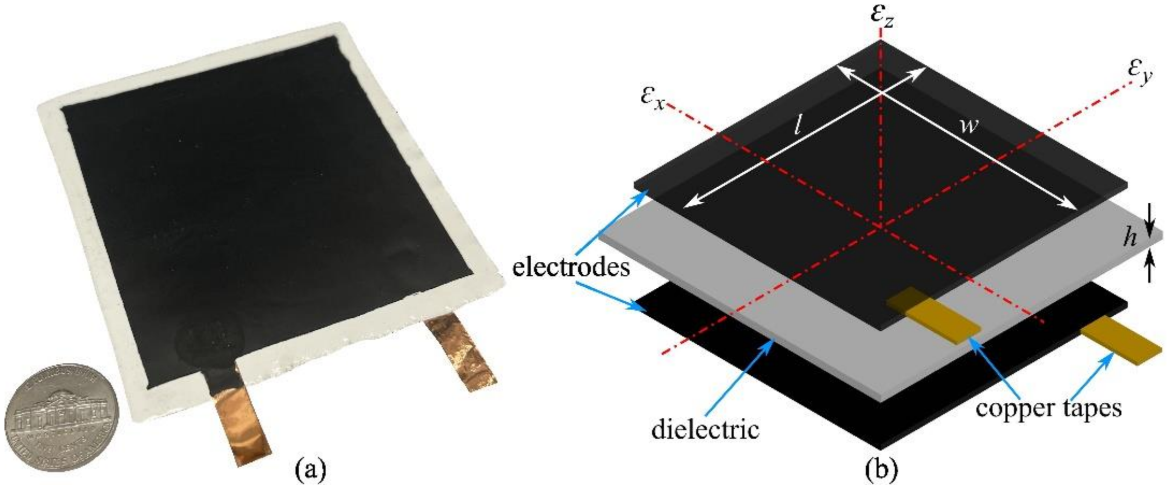

Figure 2.1. (a) A 76 mm × 76 mm SEC with a nickel for scale and (b) an exploded view of the sensor architecture with key components annotated

Fabrication Process

The dielectric layer of the sensor is fabricated by doping titania (TiO_2) particles into a block copolymer matrix of styrene-ethylene/butylene-styrene (SEBS), used to increase the permittivity and durability. The conductive plates (i.e., electrodes) are also constructed from a SEBS matrix but doped with carbon black particles to provide conductivity while improving the stability of SEBS against ultraviolet (UV) degradation. Two adhesive copper tapes are installed onto the top and bottom electrodes to enable the mechanical connection. Here, the top electrode is used as an input to the DAQ system, and the bottom electrode is used for grounding. The inclusion of the titania and carbon black are critical in providing the sensor with high durability and weatherability protection for field implementation (Downey et al. 2019).

Electromechanical Model

The SEC is an excellent technology for fatigue crack detection, localization, and monitoring on metallic structures. It can cover large areas in a networked configuration due to its high scalability provided by its low cost and easy fabrication. Its ultra-compliance guarantees robustness and durability with respect to fatigue crack quantification and long-term monitoring. Assuming under a low measurement frequency (<1 kHz), the initial capacitance C_0 of the SEC is formulated as follows:

$$C_0 = e_0 e_r \frac{A}{h} \tag{1}$$

where $e_0 = 8.854 \text{ pFm}^{-1}$ is the vacuum permittivity, e_r is the dielectric permittivity, $A = w \times l$ is the sensing area of the SEC, with w and l being the width and length of the electrode, and h is the thickness of the dielectric, as denoted previously in Figure 2.1b. Assuming small strains, an expression for the relative change in capacitance $\Delta C / C_0$ can be obtained by differentiating equation 1 as follows:

$$\frac{\Delta C}{C_0} = \left(\frac{\Delta l}{l} + \frac{\Delta w}{w} - \frac{\Delta h}{h} \right) = \varepsilon_x + \varepsilon_y - \varepsilon_z \tag{2}$$

where Δ denotes a change in the variable due to strain, subscript *0* represents the initial value of the variable, and ε represents strain along the axis in subscript. For surface strain monitoring, an SEC is deployed along the *x*-*y* plane. Assuming plane stress and applying Hooke's Law, one obtains the following:

$$\varepsilon_z = -\frac{\nu}{1-\nu} (\varepsilon_x + \varepsilon_y) \tag{3}$$

Substituting equation 3 into equation 2, the capacitance response of a free-standing SEC is written as follows:

$$\frac{\Delta C}{C_0} = \frac{1}{1-\nu_0} (\varepsilon_x + \varepsilon_y) = \lambda_0 (\varepsilon_x + \varepsilon_y) \tag{4}$$

where $\nu_0 = \nu_x = \nu_y = \nu_z$, and ν_0 is the Poisson's ratio for an isotropic SEC, and λ_0 is the gauge factor. Equation 4 reveals that ΔC varies linearly with the in-plane strains ε_x and ε_y. When the sensor is installed over a fatigue crack, the opening and closing of the crack causes a geometric deformation of the sensor, thus its signal can be used to measure fatigue crack growth.

cSEC

This subsection is extracted from the following publication:

Liu, H., S. Laflamme, J. Li, C. Bennett, W. Collins, A. Downey, P. Ziehl, and H. Jo. 2021. Investigation of Surface Textured Sensing Skin for Fatigue Crack Localization and Quantification. *Smart Materials and Structures*, Vol. 30, No. 10.

The design of the SEC has been altered recently to improve signal stability and sensitivity in order to facilitate field implementation. This was done by corrugating the top surface of the dielectric to tune the sensor's stiffness, resulting in lowering the sensor's Poisson's ratio and improving its mechanical stability, termed cSEC. This new generation cSEC is shown in Figures 2.2a and 2.2b.

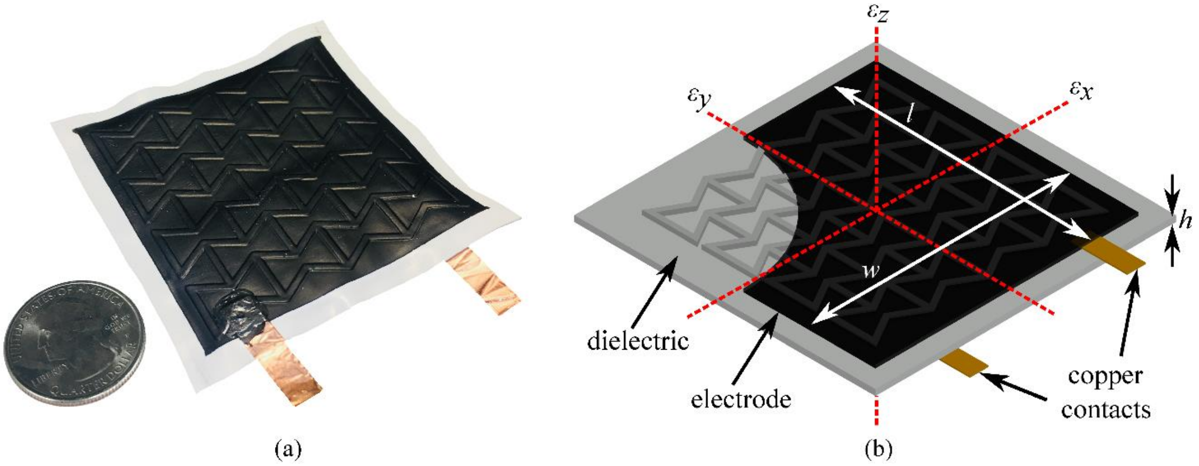

Figure 2.2. (a) A 76 mm × 76 mm textured SEC (re-entrant hexagonal honeycomb pattern) with a quarter for scale and (b) an annotated schematic of a textured SEC

Fabrication Process

A cSEC is composed of a corrugated dielectric layer sandwiched between two conductive layers. Its fabrication process is illustrated in Figure 2.3.

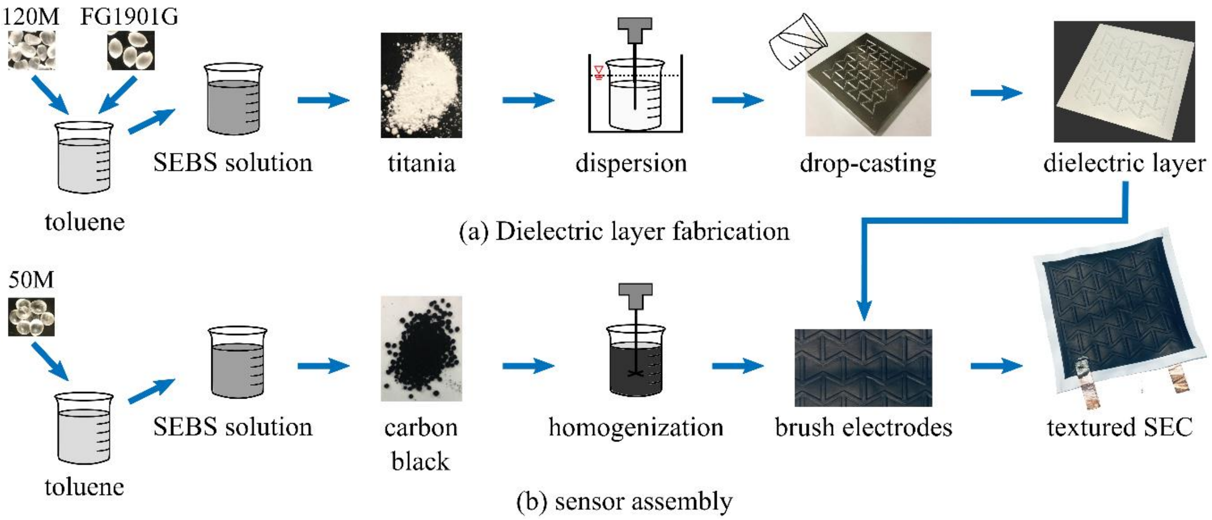

Figure 2.3. Fabrication process of a textured SEC: (a) dielectric layer fabrication and (b) sensor assembly

The dielectric is fabricated by using SEBS FG1901G (KRATON, United States, ρ = 1400 kg/m^3, 30%w styrene, permittivity 2.4) and SEBS 500120M (VTC Elastoteknik AB, Sweden, ρ = 930 kg/m^3). Polydimethylsiloxane (PDMS)-coated titania $TiO_2(-OSI(CH_3)_2-)$ (TPL, Inc., Albuquerque, New Mexico) particles with an average diameter of 100 nm are mixed into the SEBS matrix to increase both the durability and permittivity of the dielectric layer (Stoyanov et al. 2011). The fabrication of the dielectric layer (Figure 2.3a) is described as follows:

- A SEBS/toluene solution is prepared by mixing SEBS FG1901G and SEBS 500120M with a weight ratio of 1:3 and dissolving in toluene at a concentration of 160 g/L. A mass of TiO_2 particles are added to the SEBS stock solution to achieve a concentration of 75 g/L.
- Titania TiO_2 particles are uniformly dispersed using a sonic dismembrator (high-intensity ultrasonic processor Vibracell 75 041, Sonics & Materials, Inc., United States) for 5 minutes at 20 kHz and 120 W while the solution sits in an iced water bath for cooling.
- A volume of 20 ml of the SEBS-titania solution is drop-cast directly onto an 80 mm × 80 mm nonstick square steel mold (H13 steel with HRC48-50 hardness, 1 µm peak-to-valley accuracy, and surface roughness of 0.85 µm). The grooved mold yields a corrugated dielectric that gives rise to the texture of the top layer. The drop-casted solution is covered to control the evaporation rate and left in a fume hood to dry over 24 hours.
- The film is peeled from the mold and left to dry for another 24 hours at room temperature. The resulting film has an approximate mean thickness of 0.30 mm over the noncorrugated area, a corrugation height of 0.35 mm, and permittivity of 5.56.

The electrode layers are fabricated using SEBS 500050M (VTC Elastoteknik AB, Sweden) and filled with carbon black particles (Orion Engineered Carbons, Kingwood, Texas). The use of carbon black provides the sensor with the required conductivity and environmental robustness (Downey et al. 2019). The fabrication of the electrodes (Figure 2.3b) is described as follows:

- SEBS 500050M raw material is dissolved in toluene at a concentration of 380 g/L, and carbon black particles are added to the stock solution to have a concentration of 25 g/L. A low-speed homogenizer is used for 1 hour at 650 to 850 rpm to obtain a uniform dispersion.
- Four layers of the conductive solution are brushed onto both the top and bottom surfaces of the dielectric layer with 30 minutes drying time between placement of each layer and 24 hours of drying time after four iterations of brushing, both at room temperature. The resulting conductive electrode has a sheet resistance of approximately 2.6 kΩ/Sq and a thickness of approximately 25 µm.
- Adhesive copper tapes are glued on each side of the film to achieve electrical connections for the DAQ. PELCO conductive carbon glue (Ted Pella, Inc., United States) is used to coat the exposed parts of the copper tapes at the electrode layer to enhance mechanical durability and minimize added noise.

Electromechanical Model

Adopted from the untextured SEC, the use of a textured surface results in an orthotropic composite, and the Poisson's ratio in the *x*-*y* is given as follows:

$$\nu_{xy} = -\frac{\varepsilon_y}{\varepsilon_x} \tag{5}$$

Substituting equation 5 into equation 4 provides the electromechanical model for the cSEC under uniaxial strain (along the *x*-direction).

$$\frac{\Delta C}{C_0} = \frac{1-\nu_{xy}}{1-\nu}\varepsilon_x = \lambda\varepsilon_x \tag{6}$$

where $\nu_0 = \nu_{xz} = \nu_{yz} = \nu_0$, and λ is the gauge factor of a cSEC under uniaxial strain.

Equation 6 shows that λ is a function of the transverse Poisson's ratio and increases with decreasing ν_{xy}. When the sensor is adhered onto a monitored material, the transverse Poisson's ratio is altered due to the composite effect. The composite transverse Poisson's ratio $\nu_{xy,c}$ can be written as follows:

$$\nu_{xy,c} = \frac{a\nu_{xy}+b\nu_m}{a+b} \tag{7}$$

where ν_m is the Poisson's ratio of the monitored material, and *a* and *b* are weight coefficients that represent the composite effect with values between 0 and 1, with *a* + *b* = 1. Therefore, the resulting gauge factor under composite effect is given by the following:

$$\lambda = \frac{1-\frac{a\nu_{xy}+b\nu_m}{a+b}}{1-\nu} \tag{8}$$

When subjected to a fatigue crack, part of the sensor will be detached from the surface and the strain effect localized over a small region of the sensor. It follows that the resulting signal is nonlinear, and that the localized strain significantly boosts the signal's magnitude.

Electrically Isolated Capacitive Sensing Skin

This subsection is extracted from the following publication:

Ogunniyi, E. A., H. Liu, A. R. Downey, S. Laflamme, J. Li, C. Bennett, W. Collins, H. Jo, and P. Ziehl. 2023. Soft Elastomeric Capacitors with an Extended Polymer Matrix for Strain Sensing on Concrete. *Sensors and Smart Structures Technologies for Civil, Mechanical, and Aerospace Systems 2023* (Vol. 12486, pp. 262–270). SPIE, Bellingham, WA.

Investigations on concrete show that the SEC is sensitive to localized cracks on the concrete substrate (Yan et al. 2019). However, strain values measured by the SEC are higher than the actual strain on the concrete being monitored. In order to utilize the SECs on concrete structures, it is essential to measure the actual strain present in the concrete, as opposed to simply monitoring abnormal variations (such as those caused by damage). For this project, we hypothesized that high strains recorded by the SECs bonded on the concrete surface result from capacitance coupling between the SEC/concrete interface due to the intrinsic capacitance of the cement matrix in the concrete (Wen and Chung 2004). Therefore, the challenge with deploying SECs on concrete is not because of the slight electrical conductivity of the concrete but rather its intrinsic capacitance. For example, the SEC has been successfully deployed on conductive materials such as aluminum and steel. The success of the SEC on conductive materials is attributable to the fact that the impedance of these materials is nearly perfectly resistive. At the same time, concrete has a significant capacitive component to its impedance.

Deploying the SEC with the use of additional isolation material is required but complex to achieve, especially when installing multiple sensors. This project modified the SEC to achieve isolation by adding an extended polymer matrix of SEBS on both sides of the SEC sensor to act as an integrated isolation layer that extends the polymer matrix that makes up the SEC to five layers. The extended polymer matrix of SEBS is a transparent layer over the electrodes; this addition does not affect the sensor's sensitivity. With this design, an SEC is achieved for monitoring structural changes in concrete materials without needing separate isolation material. The contributions of this project are (1) advancing previous research on strain sensing in concrete through the implementation of an extended polymer matrix of SEBS to minimize capacitance coupling between the SEC and concrete and (2) conducting an experimental study on the capacitive coupling between a sensing skin and a concrete structure.

Figure 2.4a depicts a single SEC with a surface area of 76.2 × 76.2 mm (3 × 3 in.), and Figure 2.4b depicts a schematic of the sensor with an extended polymer matrix developed in this project. It is worth noting that the geometry (such as form and size) can be changed. The resulting sensor has the following features: low cost, great ultra-flexibility, mechanical robustness, ease of installation, and low power consumption required for sensing.

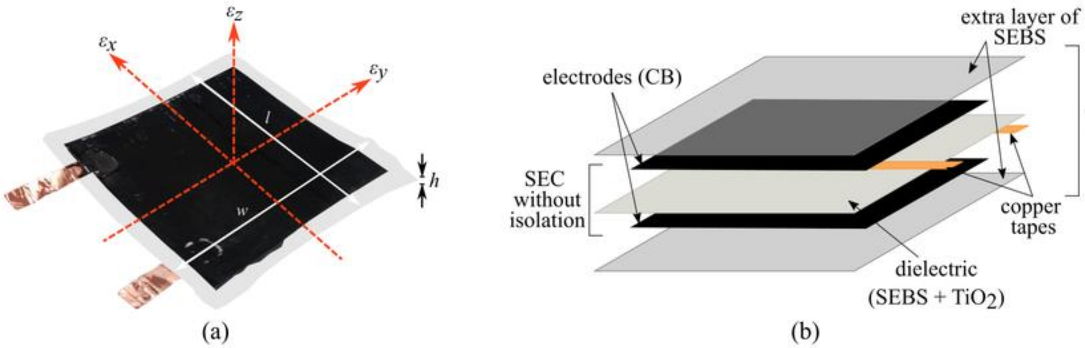

Figure 2.4. Extended SEC showing (a) dry and ready-for-use sensor and (b) schematic of the layers making up the extended sensor

Fabrication Process

The fabrication process of the SEC with the extended polymer matrix is shown in Figure 2.5 and described in the six steps that follow.

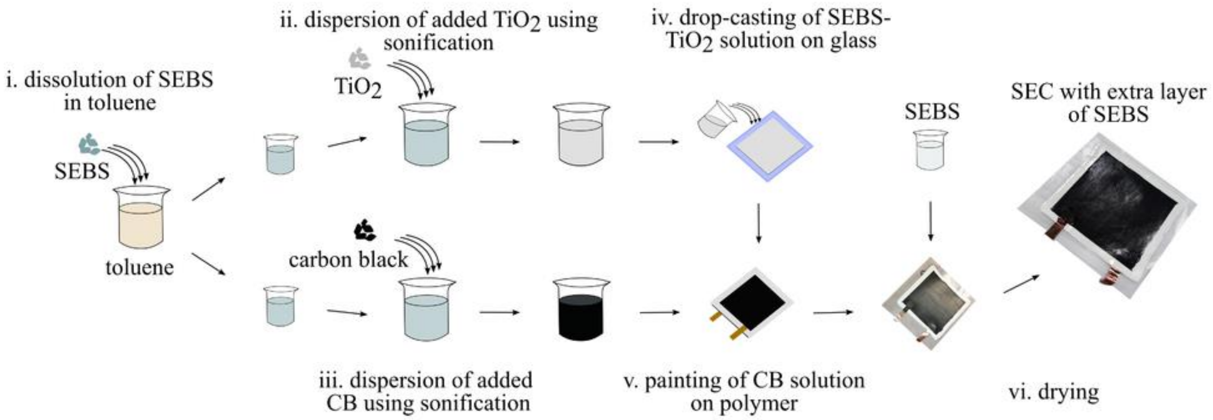

Figure 2.5. Extended SEC fabrication process

1. Toluene is used as the solvent to dissolve SEBS 500120M (Mediprene Dryex) particles to prepare the SEBS/toluene solution at a concentration of 160 g/L. PDMS-coated titania TiO_2 (-OSI(CH_3)$_2$-) rutile particles are dispersed in a portion of the SEBS/toluene solution at a concentration of 75 g/L.
2. Titania particles are further uniformly dispersed in the SEBS matrix using an ultrasonic tip (Fisher Scientific D100 Sonic Dismembrator) at 20 kHz and 120 W for 5 minutes.
3. Another SEBS/toluene solution is prepared by dissolving SEBS 500050M in toluene for a concentration of 380 g/L. Carbon black particles (Orion Printex XE 2-B) are scattered at a 25 g/L concentration in the stock solution and dispersed using a low-speed homogenizer for 1 hour at 650 rpm.
4. The dielectric layer is made utilizing a solution cast process, in which 20 ml of the prepared SEBS-TiO_2 solution is dropped and cast directly onto a 76.2 × 76.2 mm (3 × 3 in.) glass slide

and covered for 24 hours in a fume hood to allow the toluene to evaporate. The resulting film is peeled off from the glass plate and left to dry for 12 hours at room temperature.

5. The resulting SEBS-carbon black solution is brushed onto both the top and bottom surfaces of the dielectric, and a total of 4 layers of the conductive solution are brushed on each side with 30 minutes of drying between each layer. Two conductive copper tapes are implanted into the liquid electrode layers to provide mechanical connections for the wires that connect the sensor to the DAQ system.
6. The resulting multilayered nanocomposite is allowed to dry for 24 hours. The SEC is then extended with an extra layer of nonconductive SEBS 500120M/toluene solution without TiO_2 on both surfaces for a composite configuration, preventing capacitive coupling between the electrode and the concrete layer.

Future Directions in Soft Elastomeric Capacitive Sensing

This subsection is extracted from the following publications:

Liu, H., M. Kollosche, S. Laflamme, and D. Clarke. 2023.Multifunctional Soft Stretchable Strain Sensor for Complementary Optical and Electrical Sensing of Fatigue Cracks. *Smart Materials and Structures*, Vol. 32, No.4.

Liu, H., S. Laflamme, and M. Kollosche. 2023. Paintable Silicone-Based Corrugated Soft Elastomeric Capacitor for Area Strain Sensing. *Sensors*, Vol. 23, No. 13.

Multifunctional Soft Stretchable Strain Sensor

Timely discovery of damage can be achieved using SHM technologies. Electromechanical methods are popular SHM techniques used to detect cracks through local changes in electrical properties. For example, using restive paints (Kurnyta et al. 2021), CNT-based films (Lin et al. 2020, Gupta et al. 2021), flexible sheets of resistors (Aygun et al. 2020), and SECs (Kong et al. 2018). The promise of these technologies lies in the coverage of large structural surfaces, enabling both fatigue crack discovery and quantification during operations. Optical properties can be leveraged to assist in damage detection and visualization during visual inspections. Investigations on structurally colored materials that undergo visible (400 to 800 nm) absorption and spectral emission changes in response to external stimulus have been conducted and reported over the last decade (Sun et al. 2013, Behera 2022). Structurally colored materials that respond to mechanical stimuli have been proposed for optical sensing (Yue and Gong 2015). The promise of these materials is that color change or intensity change can be obtained without degradation under external mechanical stimuli.

In this project, we developed a new multifunctional skin sensor technology that combines both optical and electrical responses to strain and capable of fatigue crack monitoring. The novelties are twofold: (1) the optical signal of the structural color film is angle-independent and thus greatly facilitates field measurements using an affordable camera, and (2) the optical and capacitive signals are combined to improve the detection and identification of fatigue cracks. The purpose of the optical signal is to visually assist in locating fatigue cracks, and that of the capacitive signal is to send timely warnings to infrastructure operators. The optical property arises from a structural color film, fabricated with monodispersed silica nanoparticles (NanoCym). Its mechanoresponsive behavior results in a reversible, observable to the naked eye, and angle-independent color change under an ambient environment. This color film is then sandwiched between two transparent CNT electrodes to produce a flexible, parallel plate capacitor to add the electromechanical property. The fabrication steps of the soft structural color film are illustrated in Figure 2.6a.

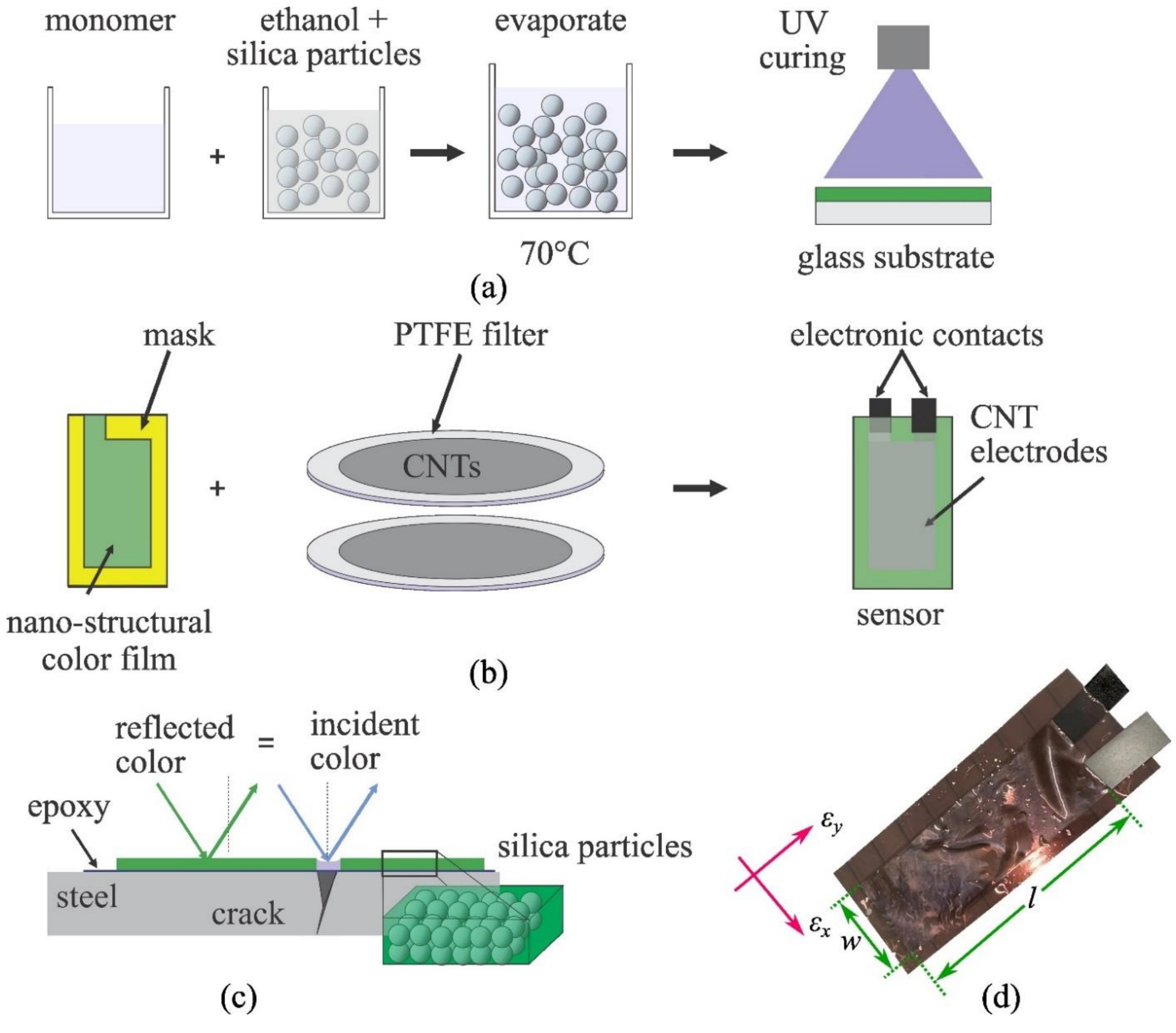

Figure 2.6. (a) Fabrication steps of the structural color film capacitor material, (b) formation of the CNT electrodes by CNT stamping, (c) optical mechanism, (d) and the assembled sensor

Silica nanoparticles with a diameter of 100 nm were purchased from NanoCym and washed in anhydrous ethanol at least three times. Then, the particles were dispersed in anhydrous ethanol in a ratio of 1:10 w/w. The host polymer matrix poly(ethylene glycol) phenyl ether acrylate (Sigma-Aldrich) was mixed with 1 w/w of photoinitiator (2-hydroxy-2-methyl-1-phenyl-1-propanone, Sigma-Aldrich), named monomer. The silica particles and the matrices in a ratio of 40 wt% of SiO_2 were mixed using a shear mixer for 5 minutes at 2,000 rpm, and the resulting composite is stored at 70ºC to evaporate the ethanol for several hours. The resulting material was cast onto glass slides. To enable easy peeling of the stretchable composite, a sacrificial layer of water-soluble dextran (MW 15000–25000, Sigma-Aldrich) was first spin coated onto the glass slide. In the final step, the composite was cured under UV light and nitrogen atmosphere for 5 minutes at 8 W and 254 nm wavelength for solidifying.

The structural color relies upon the interference of light, scattered in the nanoscale structures of randomly arranged silica spheres. Different materials hosting nanostructures can be employed, among them polymers or other responsive materials. The mechanical properties provided by the polymer matrix allows external triggers—such as strain, temperature, and change in the scattering structure—to produce changes in the optical appearance. This enables tuning and therefore adds functionalities of the materials for different applications such as sensors, displays, and camouflage. The essential characteristic of our structural color film is the stretchability of the soft composite and a predictable and reversible color response to external stimuli. In this study, silica (SiO_2) particles were employed to serve as photonic structural changes in their density, enabling reversible, repeatable, and angle-independent color changes under stretch. The optical functionality can be used to recognize the presence of fatigue cracks on steel given the strain provoked by the opening of the crack, as illustrated in Figure 2.6c.

When electroded on both sides, the silica/elastomer composite film becomes a parallel plate capacitor as shown in Figure 2.6b. The electrodes on the structural color composite film are defined by a masking layer applied directly after peeling of the cured polymer film. To form a stretchable fairly transparent electrode, CNT electrodes were prepared from a commercially available CNT solution (Invision 3500, NanoC). An amount of 5 ml of the CNT ink was diluted in isopropanol, sonicated for 10 minutes and vacuum filtered through a porous polytetrafluoroethylene (PTFE) membrane with a pore size of 0.5 nm. The resulting PTFE filter membrane had a sheet resistance of 600 Ω/Sq (20J3 Sheet Resistance Meter, DELCOM Instruments, Inc.). A masking layer was used to define the electrode areas, produced by stamping, on both sides of the film. The PTFE filters with the CNT electrode was stamp-transferred onto both sides of the previously prepared structural color film to define the parallel plate capacitor structure, simultaneously combining the optical and electrical sensing properties. Finally, electrical connections were applied and the sensors transferred for testing and evaluation. The two electrodes are highly compliant and transparent, thus minimizing optical absorption. Consistency and uniformity of specimens was ensured through a quality control process that consisted of measuring and evaluating the thickness, color response, permittivity, dissipation factor, and initial capacitance across the optical and electrical properties.

Paintable Silicone-cSEC

A key limitation of the SEBS-cSEC technology is the need for an epoxy that provides reliable bonding of the sensor onto the monitored surface, mainly attributable to the sensor's fabrication process that comprises a solvent that limits its direct deployment through a painting process. This project investigated a paintable version of the cSEC and developed an improved solvent-free fabrication process using a commercial room-temperature-vulcanizing silicone. In comparison to thermoplastic elastomers (e.g., SEBS), silicone is chemically cross-linked and is constituted from siloxane that confers the typical rubbery property with excellent stretchability, biocompatibility, heat and chemical resistance, physiological inertia, and hydrophobicity (Chen et al. 2019, Wang et al. 2020). A thin layer of silicone was directly painted onto the monitored surface to bond the prefabricated silicone-cSEC. This configuration enables polymer-on-polymer contact that can use interfacial chain entanglements to provide sufficient bonding strength for direct deployment.

The commercially available liquid silicone Wacker 7670 A and B components were used as the host matrix. Both the A and B components contain siloxane and silica particles in the range of 30 to 40 wt% (Skov and Yu 2018). The silicone has a relative permittivity of 2.9 (Matysek et al. 2008), is elastically stretchable beyond 200% (Cohen et al. 2022), and has a stiffness of approximately 220 kPa (Downey et al. 2019) in its pure form. The relative permittivity was boosted using high permittivity titania particles dispersed in the prepolymer before the A and B components were mixed and cured. Details of the fabrication process (Figure 2.7) are described as follows:

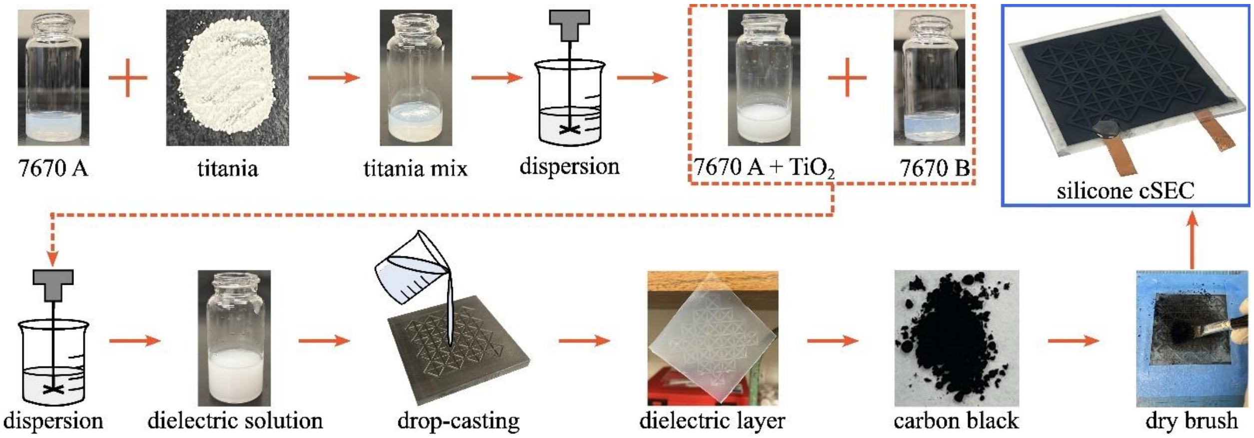

Figure 2.7. Fabrication process of a silicone-cSEC

- PDMS-coated titania $TiO_2(-OSI(CH_3)_2-)$ (TPL, Inc., Albuquerque, New Mexico) particles with an average diameter of 100 nm are added in 3 wt% to 5 mL of the liquid silicone WACKER Elastosil P 7670 A (Polydimethyl siloxane (63148-62-9), Polydimethylsiloxane vinyl terminated (68083-19-2), (TSRN 38673700-5112 P)) for a concentration of 30 g/L.
- Rutile titania particles are uniformly dispersed in the silicone matrix using a low-speed homogenizer for 600 seconds at 650 rpm, while the solution is cooled in an iced water bath.
- A volume of 5 mL of the liquid silicone WACKER Elastosil P 7670 B (Polydimethyl siloxane (63148-62-9), (TSRN 38673700-5101P), Polydimethylsiloxane vinyl terminated (68083-19-2), Silazanetreated Silica (68909-20-6), Polydimethyl hydrogenmethyl siloxane (69013-23-6)) is added into the stock solution and mixed using a shear mixer for 180 seconds at 2,000 rpm, yielding a dynamic viscosity of approximately 2,000 cP.
- The resulting silicone-titania solution is drop-cast onto an 80 mm × 80 mm nonstick square steel mold. The steel mold contains grooves to create a corrugated pattern. The use of surface

corrugation is known to improve strain sensing performance by adding in-plane stiffness and decreasing the transverse Poisson's ratio (Liu et al. 2021a).

- The drop-casted solution is cured at room temperature for 6 hours, and the film is subsequently peeled from the mold. The resulting film has a mean thickness of 0.4 mm over the non-corrugated area and a corrugation height of 0.35 mm. Note that the thickness of the dielectric layer can be tuned by controlling the volume of the silicone-titania solution drop-casted into the steel mold.
- Carbon black particles are stored in an oven at 50ºC for 24 hours to remove moisture, and an antistatic gun (Milty 5036694022153 Zerostat 3) is used to remove the static charge on the surface of the cured dielectric film before brushing electrodes. A dry stacking process through stamping that has no solvent-elastomer interactions (Cohen et al. 2022) can be employed for future studies.
- The dry carbon black particles are brushed onto both sides of the dielectric layer to form conductive soft stretchable electrodes. The painting process is stopped once the electrode has reached a sheet resistance of approximately 3.6 kΩ/Sq (Botron digital surface resistivity meter, SKU: B8563). In prior work on the SEBS version of the sensor, we conducted accelerated aging tests and found that the use of carbon black conferred the polymer with long-term durability both mechanically and electromechanically (Downey et al. 2019). While a similar study on silicone-cSECs is left to future work, we hypothesize that the use of carbon black would yield similar conclusions.
- Adhesive copper tapes are glued on the brushed conductive electrodes to create electrical connections to the DAQ. A thin layer of PELCO conductive carbon glue (Ted Pella, Inc., United States) is added to the exposed parts of the copper tapes to enhance mechanical bonding strength and minimize signal noise. The resulting silicone-cSEC has a permittivity of 4.05 at 100 Hz (equation 1) with an effective thickness of 0.52 mm for the electrode section of the sensor, which corresponds to an increase of approximately 40% compared to the pure silicone. The Young's modulus of the cured silicone composite was found to be 305 kPa using a tensile tester under a strain rate of 2.5%/second.
- As an optional step for deployment, a small amount of WACKER Elastosil P 7670 A and B components are mixed with a weight ratio of 1:1 and applied as a protecting layer onto the surface of the electrodes to improve resilience with respect to weathering. The resulting silicone-cSEC has an initial capacitance of approximately 170 to 200 pF under 1 kHz measuring frequency.

Conclusion

This chapter focused on the development of the sensing skin technology. In an effort to produce a large-scale, deployable sensing skin system, we have developed our own sensing skin solution in this project. In particular, we developed a new generation of SEC by corrugating the top surface of the dielectric layer to tune the in-plane stiffness, resulting in lowering the sensor's Poisson's ratio and improving its mechanical stability. Further, we developed an electrically isolated SEC by extending the SEBS matrix of the SEC to including include a decoupling layer between the electrode and the concrete, aiming to minimize the electrical coupling between the SEC and the substrate structure for a more accurate strain measurement on concrete structures.

For future field applications of the sensing skin technology, we developed a multifunctional sensor that consists of a soft stretchable structural color film sandwiched between transparent CNT electrodes to form a parallel plate capacitor. The resulting device exhibits a reversible and repeatable structural color change from light blue to deep blue with an angle-independent property, as well as a measurable change in capacitance, under external mechanical strain. We also studied an improved solvent-free fabrication method using a commercial room-temperature-vulcanizing silicone as the host matrix to produce a paintable cSEC. This eliminates the need for epoxy, which is usually used to create a reliable bond of the cSEC onto the monitored surface, enabling direct deployment of the cSEC through a painting process.

CHAPTER 3: LABORATORY CHARACTERIZATION OF THE SENING SKIN

Overview

This chapter presents results from the laboratory characterization of the sensing skin technology. The objective of the laboratory characterization was to determine whether the cSEC and the multifunctional soft stretchable strain sensor are capable of being used as fatigue monitoring devices in common steel bridge applications. To accomplish this, the general sensing performance of the two types of sensors were experimentally characterized and evaluated, and algorithms were formulated that validate the capability of the cSEC at measuring angular rotation as well as monitoring fatigue cracks in corner welds.

Sensing Performance

This subsection is extracted from the following publication:

Liu, H., S. Laflamme, J. Li, C. Bennett, W. Collins, A. Downey, P. Ziehl, and H. Jo. 2021. Investigation of Surface Textured Sensing Skin for Fatigue Crack Localization and Quantification. *Smart Materials and Structures*, Vol. 30, No. 10.

cSEC

Corrugated Patterns

Four candidate corrugation patterns were selected for this investigation based on the results from prior research (Liu et al. 2020a). The first is a diagonal grid pattern (Figure 3.1a), selected due to its ease of fabrication. The second is a diagrid pattern (Figure 3.1b) constructed with intersecting diagonal elements angled at 36°, selected because it outperformed other non-auxetic patterns in Liu et al. (2020a) by yielding the best SEC gauge factor and resolution. The third is a reinforced diagrid pattern (Figure 3.1c), designed based on the diagrid pattern and modified to include reinforcements angled at 45° to provide a symmetric option. The fourth is the re-entrant hexagonal honeycomb pattern (Figure 3.1d), selected because it outperformed other auxetic patterns in Liu et al. (2020b) by yielding the best SEC gauge factor and resolution. It should be noted that this investigation uses identical geometries, as reported in previous studies.

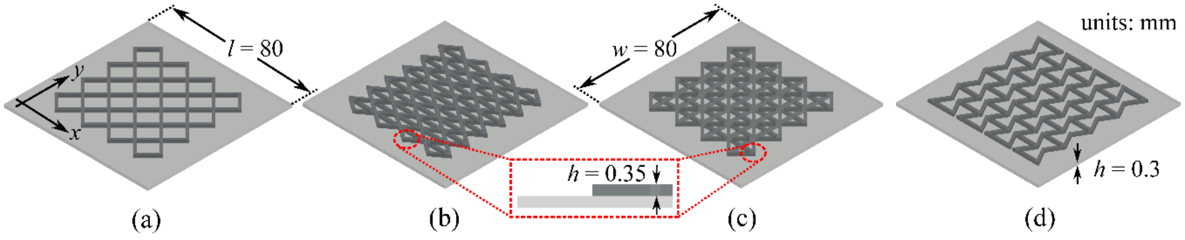

Figure 3.1. Candidate corrugated patterns: (a) symmetric diagonal grid, (b) diagrid, (c) symmetric reinforced diagrid, and (d) re-entrant hexagonal honeycomb (auxetic) pattern

Square SECs ($l = w = 76$ mm) with a sensing area of 63.5 mm × 63.5 mm (2.5 in. × 2.5 in.) were fabricated using each of the selected patterns. The initial capacitance C_0 of each cSEC varied depending on the corrugation pattern and the mean thickness of the dielectric but remained in the range of 220 to 260 pF. Three cSECs of each pattern were fabricated, plus three untextured (flat) SECs for benchmarking purposes, for a total of 15 samples. The consistency and uniformity of specimens was ensured through the utilization of computer numerical control milled steel molds and the measurement and evaluation across electrical properties and material geometries sampled at various points.

Experimental Procedure

An experimental investigation focused on the performance of the SEC for detecting and quantifying fatigue cracks was conducted on C(T) specimens following the same procedure as in prior work (Kong et al. 2016). Figure 3.2a illustrates the overall experimental setup.

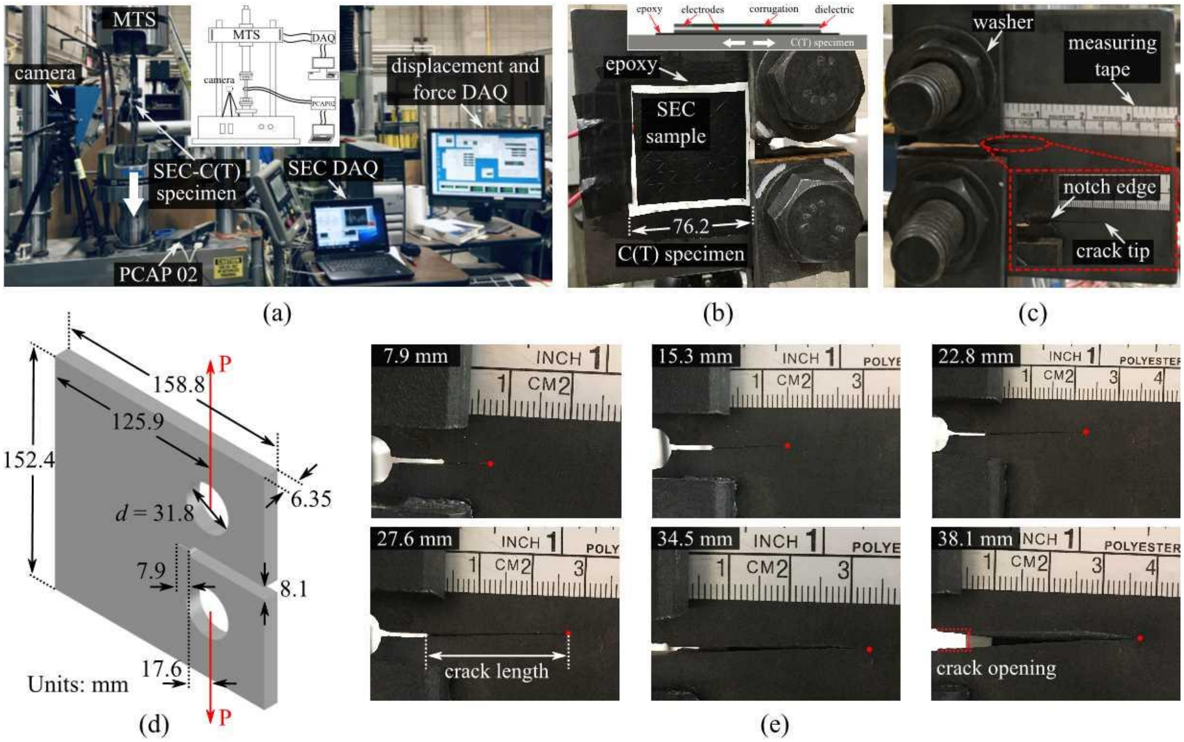

Figure 3.2. (a) Overall experimental configuration (large arrow indicates the loading direction), (b) close-up on the front surface of SEC-C(T) specimen, (c) close-up on the back surface of SEC-C(T) specimen, (d) geometric configuration of the C(T) specimen, and (e) fatigue cracks propagated over 7.9, 15.3, 22.8, 27.6, 34.5, and 38.1 mm

The C(T) specimens were fabricated from A36 structural steel plate and machined using water-jet cutting to accomplish the configuration prescribed by ASTM E647-15, shown in Figure 3.2d. The surface of the specimen was sanded using 1000 grit sandpaper and cleaned with acetone. As shown in Figure 3.2b, a thin layer of off-the-shelf bicomponent epoxy (JB Weld) was applied onto the front side of the C(T) with the flat surface of the SEC fully adhered onto the epoxy layer. For the nonsymmetric patterns (diagrid and re-entrant hexagonal honeycomb), the sensors were adhered by aligning their most flexible axis (their *y*-axis, as indicated in Figure 3.1) with the axial load to provide enhanced electrical sensitivity to the damage produced by cracking. A peel-and-stick tape measure was adhered onto the back surface of the C(T) specimen (Figure 3.2c) to monitor and quantify the crack length via photographs taken during the test. The experiments were conducted using a closed-loop servo-hydraulic testing machine (MTS model 312.41 with a TestStar IIm controller) equipped with the 647 Hydraulic Wedge Grip. The SEC-C(T) specimen was mounted using a pair of clevises and installed onto the grip, and washers were used in conjunction with screw nuts to prevent relative sliding and to distribute stress evenly.

The loading range was designed to evaluate the performance of the SEC for detecting low-cycle fatigue cracks and quantifying damage levels. A 2 Hz harmonic excitation in tension-tension mode between 2.9 kN (0.65 kips) and 29 kN (6.5 kips), resulting in a constant stress intensity ratio R of 0.1, was applied to the SEC-C(T) specimen to generate a fatigue crack. Note that this loading resulted in a stress intensity higher than that prescribed in ASTM E647-15, which facilitated more rapid crack growth in this study. Load and displacement were sampled at 20 Hz, where the displacement was directly extracted from the linear variable displacement transducer (LVDT) of the servo-hydraulic testing machine instead of the localized displacement experienced by the sensor. The capacitance data were collected at 25 Hz using an off-the-shelf DAQ board (ACAM PCAP02). Wires were fixed with electrical tape to create an electrically insulating barrier and minimize the electrical noise due to cable movement. Each test ran continuously until the maximum displacement of the testing machine reached 2.54 mm.

For this study, crack length was defined as the distance measured from the crack tip to the notched edge, as shown in the magnified view of Figure 3.2c. Figure 3.2e presents photographs of a fatigue crack propagating over 7.9, 15.3, 22.8, 27.6, 34.5, and 38.1 mm taken at cycle 8153, 11709, 13141, 13991, 14506, and 14983, respectively, where the crack tip is indicated with a red dot. It can be observed that the crack opening (indicated in Figure 3.2e) increased with the extension of the fatigue crack. Slight out-of-plane deformations were observed for crack lengths over 38.1 mm due to lateral torsion.

Numerical Simulation

A three-dimensional (3D) nonlinear finite element model (FEM) was constructed in ANSYS 2020 R1 to numerically reproduce laboratory experiments conducted on C(T) specimens. A C(T) specimen was fabricated from a 6.4 mm (1/4 in.) A36 steel plate having geometric dimensions consistent with ASTM E647-15, as shown in Figure 3.2d. The material properties of the A36 steel used in the finite element simulation of crack damage are tabulated in Table 3.1.

Table 3.1. Assigned properties for A36 steel

Material property	Value
Density	7850 kg m^{-3}
Young's modulus	2.02×10^{11} Pa
Poisson's ratio	0.3
Bulk modulus	1.67×10^{11} Pa
Shear modulus	7.69×10^{10} Pa
Strength coefficient	9.20×10^{8} Pa
Strength exponent	-0.106
Ductility coefficient	0.213
Ductility exponent	-0.47
Cyclic strength coefficient	1.01×10^{9} Pa
Cyclic strain hardening exponent	0.2
Tensile yield strength	4.20×10^{8} Pa
Tensile ultimate strength	5.60×10^{8} Pa
Material coefficient C	3.26×10^{-10}
Exponent m	2.86

The sensor installed onto the C(T) specimen was modeled with a base layer thickness of 0.30 mm and textured height of 0.35 mm, and the SEBS material was defined as an isotropic polymer, with Young's modulus E = 0.41 MPa obtained from the tensile testing, and strain-dependent nonlinear Poisson's ratio v obtained experimentally in a prior study using digital image correlation (DIC) (Liu et al. 2020a) and shown in Figure 3.3.

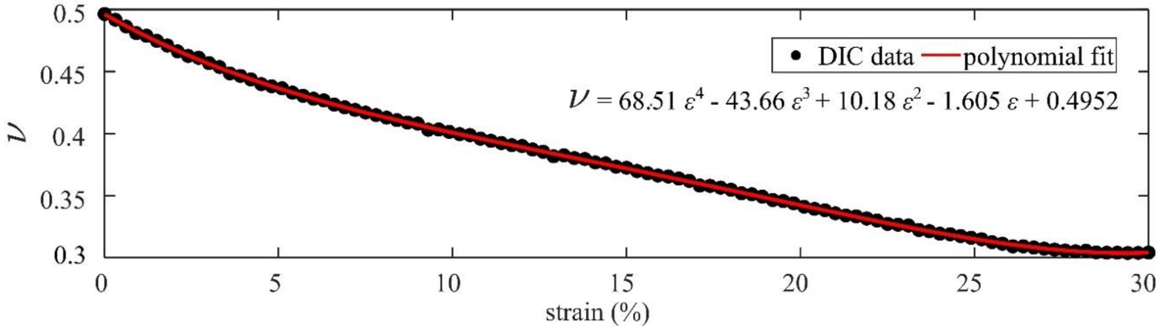

Figure 3.3. Strain-dependent nonlinear transverse Poisson's ratio

In the FEM, the capacitance response is directly obtained from the change in the sensing area using the algorithm proposed by Kong et al. (2016) and derived from the electromechanical model and presented as follows:

$$\frac{\Delta C}{C_0} = \frac{1}{A_0} \sum_{i=1}^{n} A_0 \left(\frac{A_{li}^2}{A_{0i}^2} - 1\right) \tag{9}$$

The sensor was modeled as perfectly bonded to the C(T) specimen to mimic full adhesion. The SEC-C(T) specimen was constrained as pin fixed along the circular inner surface of the upper hole (indicated in blue, Figure 3.4a), restraining x, y, z translational degrees-of-freedom (UX, UY, and UZ), and as simply supported pinned along the circular inner surface of the lower hole (indicated in red, Figure 3.4b), allowing only the y translational degree-of-freedom (UY).

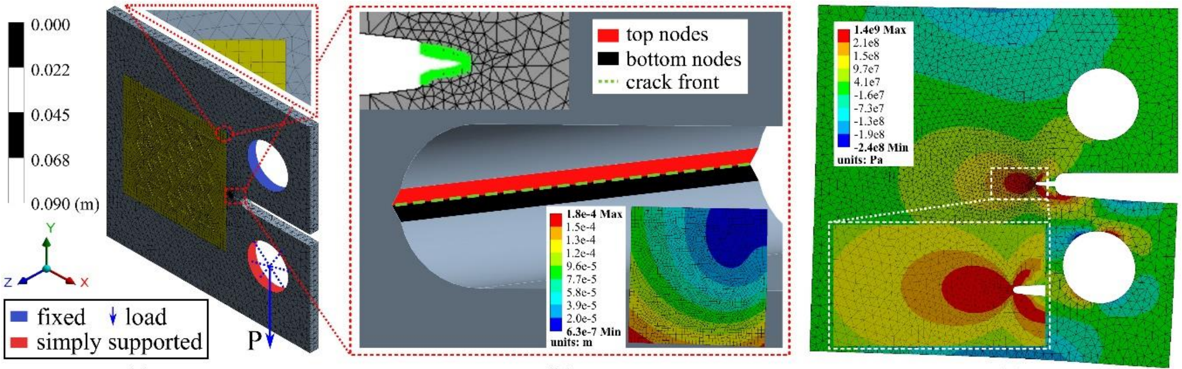

(a) (b) (c)

Figure 3.4. (a) FEM showing the geometry, boundary conditions, loading direction, mesh type, and mesh distribution; (b) close-up of FEM showing fracture setup, nodes used for the extraction of synthetic measurements, simulated fatigue growth (top left), and deformation of the cSEC under a 7.9 mm crack length (bottom right); and (c) normal stress distribution of the C(T) specimen at the peak of the loading input (the sensor is hidden for clarity)

The C(T) specimen was meshed with the tetrahedrons mesh style using the patch-conforming method, generating a total of 6,662 mesh elements with a mesh size of 0.2 mm. A 4^{o} refinement was applied around the notch to generate a much denser mesh distribution to improve the accuracy of the analysis. The SEC sensor was meshed with the multizone mesh style with a mesh size also of 0.2 mm to generate square-shaped mesh elements, simplifying the application of equation 9. A 2 Hz harmonic excitation with a constant loading range from 2.9 kN to 29 kN was applied at the lower hole of the C(T) specimen. Figure 3.4c presents a typical normal stress distribution of the SEC-C(T) specimen at the peak of the loading input for a crack length of 0 mm. The inhomogeneous stress distribution on the C(T) specimen can be explained by the asymmetric boundary conditions. The maximum stress is concentrated at the notch tip, constituting the point of crack initiation.

The fatigue behavior in the FEM is dominated by Paris's law. Figure 3.5a presents a plot of stress intensity range (ΔK) versus loading cycle, where K_{max} and K_{min} were computed using equations from ASTM E1820-20b. The subplot in Figure 3.5b shows the crack growth rate with respect to the stress intensity range in a semi-log scale.

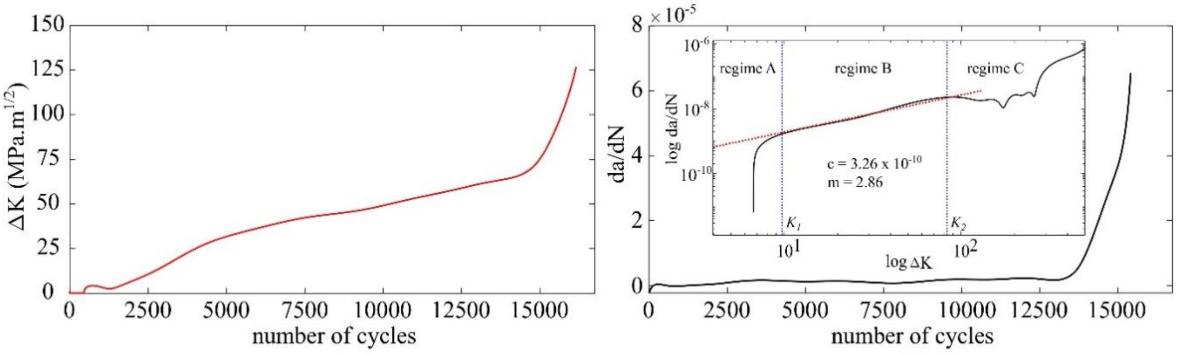

(a)

(b)

Figure 3.5. (a) Plot of stress intensity (Δ*K*) versus number of cycles and (b) crack growth rate (*da/dN*) as a function of loading cycles with the subplot showing typical crack growth rate with respect to the stress intensity range

The threshold values of K_1 and K_2 (blue dashed lines) were computed from the threshold equation in Allen et al. (1988). To simplify modeling, the Paris' law constants *C* and *m* were assigned through a linear regression (red dashed line) applied to regime B, and the material coefficients *C* and exponent *m* respectively taken as the *y*-axis-intercept and the slope of the fitted line (Broek 2012), yielding $C = 3.26 \times 10^{-10}$ (m cycle^{-1}) and $m = 2.86$. These values are in the typical ranges found in literature (Pugno et al. 2006, Ritchie 1999). Figure 3.5b plots the fatigue crack growth rate as a function of the number of cycles. The growth rate was found to be relatively small and near-constant from 0 to 13,000 cycles, as is typical in fatigue propagation. The fatigue crack growth was analyzed by using the separating morphing and adaptive remeshing technology (SMART) crack growth simulation tool (Alshoaibi and Yasin 2021) in Ansys Workbench Mechanical, enabling mode one dominant fatigue and automatic remeshing during simulations. The SMART crack method has been applied in various fatigue crack simulation studies (see Kowalski and Rozumek 2019, Li et al. 2020, and Solob et al. 2020, for instance).

A five-step procedure was established to simulate crack propagation and sensor measurements. First, a fracture objective was assigned in the numerical model using the pre-meshed crack tool, and 63 face nodes were uniformly assigned on the top and bottom crack faces respectively, as shown previously in Figure 3.4b. Second, the mesh distribution at the crack front was refined to improve crack propagation accuracy, and the computation of fracture parameters was conducted over six contours. Third, the damage evolution was defined according to Paris' law along with values for *C* and *m* (listed previously in Table 3.1). This step also defined the initial damage point and failure point, which allows each individual element to accumulate damage as it passes the initial damage point, where each element is automatically removed from the model once it reaches the limit failure point. Fourth, a maximum crack growth increment of 50 mm was defined. The previous Figure 3.4b illustrates an example of crack propagation (top left corner). Fifth, the initial and deformed area of each element was extracted within the location of the SEC sensor. The bottom-right inset in Figure 3.4b shows an example of maximum deformation of the SEC when the C(T) specimen reached a crack length of 7.9 mm, such that the crack tip reached the sensor. These changes in area were used to compute the capacitance response of the SEC using equation 9.

Crack growth behavior within the expected Paris' law behavior regime was investigated. Figure 3.6a presents the range of crack lengths obtained from all 15 tests as a function of the number of cycles, with the error bars indicating the full range of measured crack lengths. Results are compared against those obtained from numerical simulations, shown as red triangles in the figure. Good agreement was observed between the experimental and numerical data, with all numerical values located within the crack ranges.

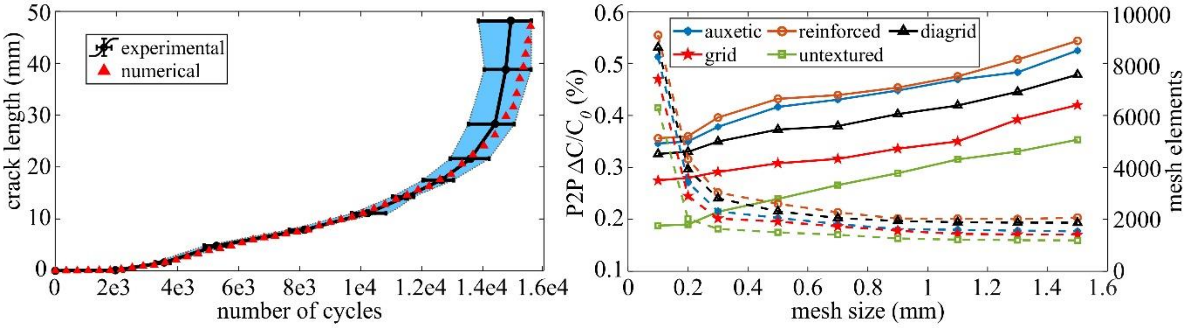

(a) (b)

Figure 3.6. (a) Range of crack lengths obtained experimentally versus numerical results as a function of the number of cycles and (b) averaged P2P $\Delta C/C_0$ amplitudes (solid lines) and corresponding number of mesh elements (dashed lines) under each pattern

An investigation of the effect of mesh size on the convergence of results was conducted for each pattern. The geometry, material properties, boundary conditions, and mesh style were kept constant for the simulations, and the mesh size varied from 0.1 mm to 1.5 mm in 0.2 mm increments. Convergence of results was evaluated by comparing the peak-to-peak (P2P) relative capacitance $\Delta C/C_0$ at a 7.9 mm crack length, where the crack started to propagate under the sensing area. Figure 3.6b presents the results, with solid lines representing the averaged P2P amplitudes and dashed lines representing the number of mesh elements. Results show that the P2P relative capacitance stabilized under a mesh size of 0.2 mm, thus validating the meshing procedure.

The simulated electric response of the sensor was investigated. Figure 3.7 presents a comparison of the numerical (simulated) and experimental (measured) relative changes in capacitance ($\Delta C/C$) time series under crack lengths of 1.6, 4.8, 7.9, 11.1, 17.9, 23.6, and 48.2 mm. Results are shown for the auxetic pattern, constituting the most complex geometry used in this investigation.

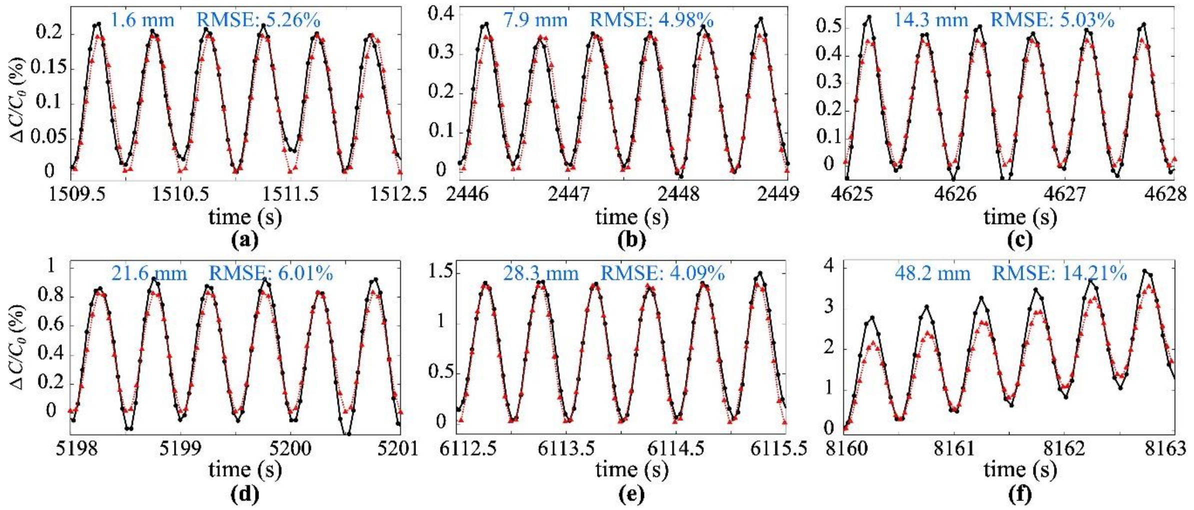

Figure 3.7. Comparison of experimental and numerical ΔC/C0 values under crack lengths of (a) 1.6 mm, (b) 7.9 mm, (c) 14.3 mm, (d) 21.6 mm, (e) 28.3 mm, and (f) 48.2 mm (shown in Figure 3.2e)

The presented experimental data were filtered by using a low-pass filter and averaged over the three tests. Good agreements were observed between the experimental and numerical results for both the magnitude and phase of the electrical response. The root mean square error (RMSE) remained approximately constant in the range of 4% to 6%, except for the larger crack size (48.2 mm), where it reached 14.2%. This larger discrepancy can be attributed to the out-of-plane deformation of the C(T) specimen creating additional strain on the SEC from the torsional phenomena.

Figure 3.8a is a typical time series plot of raw data measured from an SEC with the reinforced diagrid pattern across the entire loading process, with the vertical dashed arrows indicating the fatigue crack lengths measured from photographs.

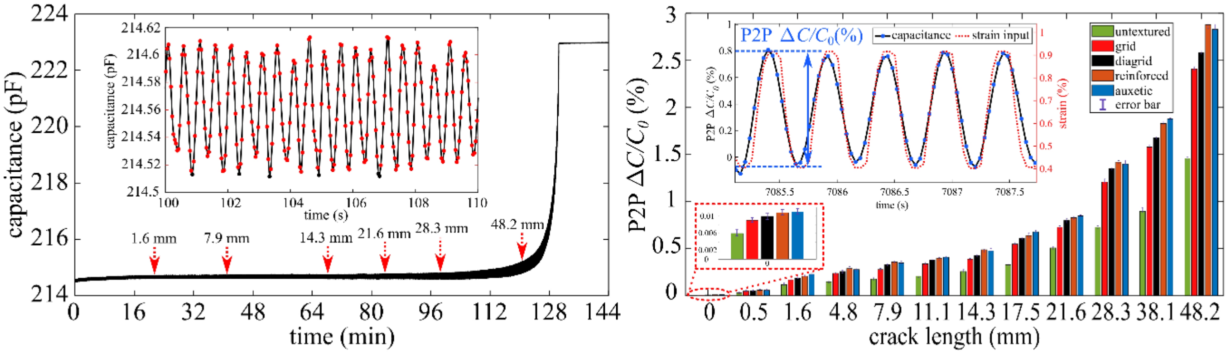

(a)

(b)

Figure 3.8. (a) Time series plot of measured raw data for a typical sensor (reinforced diagrid pattern) under cyclic loading and (b) P2P amplitudes of the relative change in capacitance ΔC/C0 for all patterns over different crack lengths

The measurements exhibit an increasing P2P amplitude denoted by the increasing apparent width of the time-series line, increasing with crack propagation, with a significant change in capacitance observed after the crack reached a length of 48.2 mm, associated with rapid crack growth until failure of the C(T) specimen. A signal drift is also observed, attributed to the plastic deformation at the crack tip in the C(T) specimen and the increasing of minimum crack opening.

The crack sensitivity of the SECs was evaluated by comparing the P2P relative change in capacitance (P2P $\Delta C/C_0$) across the different crack lengths. The P2P value, illustrated in the inset of Figure 3.8b, was utilized to filter out signal drift that could be caused by calibration and environmental effects, such as temperature and humidity. Figure 3.8b is a bar chart graphing the three-sample averaged P2P amplitudes with the error bars indicating the full P2P range over the three samples. Results were compared across each pattern over different crack lengths. It was found that the use of corrugated surfaces significantly improved the strain sensitivity, resulting in an average increase in the P2P amplitude of 53.2% (under 21.6 mm crack) to 106.1% (under 17.5 mm crack) compared to the untextured SEC, attributable to the higher gauge factors. Overall, the symmetric reinforced diagrid (reinforced) and re-entrant hexagonal honeycomb (auxetic) patterns performed better than the other patterns, with an increase in P2P amplitudes of 13.7% (21.6 mm crack) to 33.3% (7.9 mm crack), 7.9% (17.5 mm crack) to 24.6% (48.2 mm crack), and 62.7% (4.8 mm crack) to 100.1% (28.3 mm crack) compared to the grid pattern, diagrid pattern, and untextured pattern, respectively. The reinforced diagrid pattern exhibited slightly better performance than the auxetic pattern by resulting in further increases in P2P amplitudes between 1.41% and 3.48%.

The assessment of signal linearity and resolution was conducted as a function of local strain measured by the SEC. The local strain was estimated using the validated FEM. To do so, 63 pairs of nodes (indicated as the red and black dashed surfaces in the previous Figure 3.4b) were assigned at the top and bottom face of the crack from which the numerical displacement data were extracted. The relative displacement for each pair of nodes along the y direction was extracted and converted to strain using the initial width of the opening notch. Then, the strain values from each pair of nodes were averaged and the value taken as the local strain measured by the sensor.

Figure 3.9 shows plots of relative change in capacitance as a function of local strain under three representative crack sizes: 0 (undamaged), 11.1 (small crack), and 48.2 mm (large crack), for all corrugated patterns.

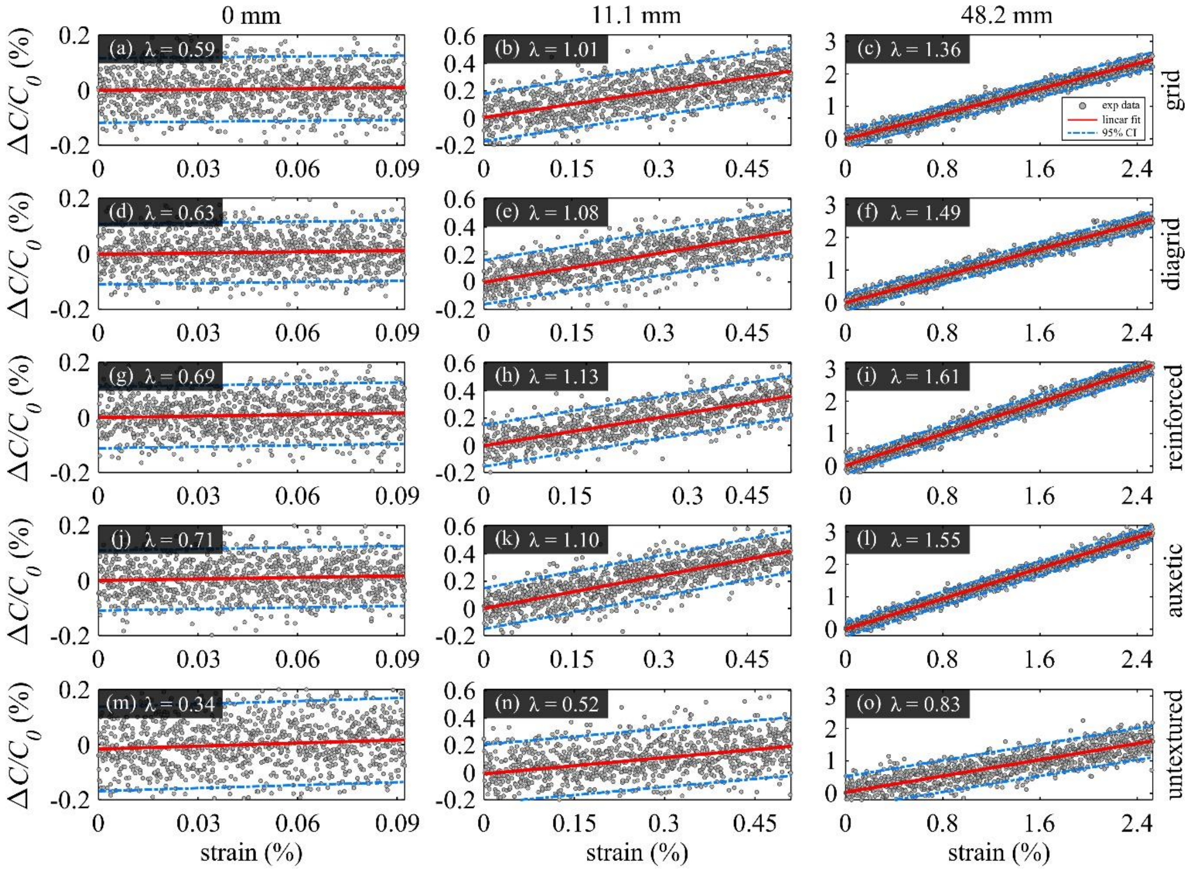

Figure 3.9. Relative change in capacitance (ΔC/C_0) as a function of local strain under crack lengths of 0 (undamaged), 11.1, and 48.2 mm under the grid pattern (a–c); diagrid pattern (d–f); symmetric reinforced diagrid pattern (g–i); re-entrant hexagonal honeycomb (auxetic) pattern (i–l); and untextured pattern (m–o)

It also includes the linear fit (red solid line) conducted using a least squares regression and the 95% confidence interval (CI) line (dotted-dashed blue, 95% CI). Values for $\Delta C/C_0$ are averaged over the three specimens for each corrugated pattern. The gauge factors computed from the linear fits are included in each subplot. One can observe that the resolution of the signal (95% CI) and gauge factor (λ) improved with the increasing crack length, with the reinforced diagrid pattern showing the best performance overall.

Table 3.2 assembles the quantitative results for crack lengths 0, 11.1, and 48.2 mm. It tabulates the universal testing machine's (MTS's) derived and local strain, the R^2 value for the linear fit (a measure of linearity), the gauge factor λ computed from the MTS-derived and local strain data (a measure of sensitivity), the 95% CI (a measure of resolution) both in terms of relative change in capacitance and strain where the strain equivalence is computed from using equation 4 with the reported local λ, and the standard deviation on the resolution σ_{res} (a measure of accuracy). All values for R^2, λ, and the 95% CI were averaged over the three specimens.

Table 3.2. Experimental results from the studied signals

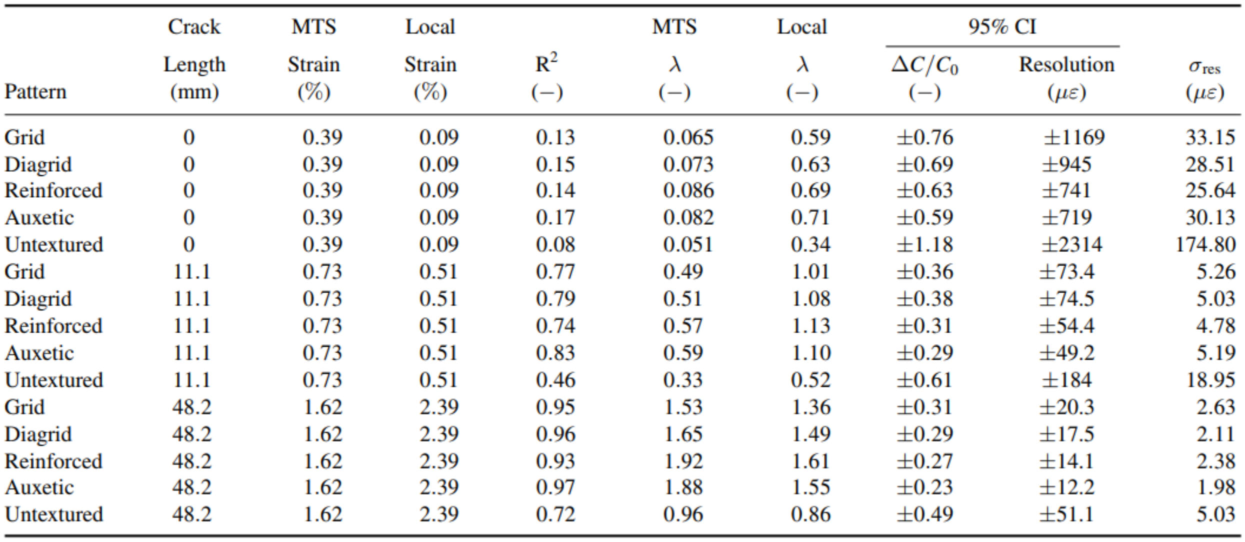

Pattern	Crack Length (mm)	MTS Strain (%)	Local Strain (%)	R^2 $(-)$	MTS λ $(-)$	Local λ $(-)$	95% CI $\Delta C/C_0$ $(-)$	95% CI Resolution $(\mu\varepsilon)$	σ_{res} $(\mu\varepsilon)$
Grid	0	0.39	0.09	0.13	0.065	0.59	±0.76	±1169	33.15
Diagrid	0	0.39	0.09	0.15	0.073	0.63	±0.69	±945	28.51
Reinforced	0	0.39	0.09	0.14	0.086	0.69	±0.63	±741	25.64
Auxetic	0	0.39	0.09	0.17	0.082	0.71	±0.59	±719	30.13
Untextured	0	0.39	0.09	0.08	0.051	0.34	±1.18	±2314	174.80
Grid	11.1	0.73	0.51	0.77	0.49	1.01	±0.36	±73.4	5.26
Diagrid	11.1	0.73	0.51	0.79	0.51	1.08	±0.38	±74.5	5.03
Reinforced	11.1	0.73	0.51	0.74	0.57	1.13	±0.31	±54.4	4.78
Auxetic	11.1	0.73	0.51	0.83	0.59	1.10	±0.29	±49.2	5.19
Untextured	11.1	0.73	0.51	0.46	0.33	0.52	±0.61	±184	18.95
Grid	48.2	1.62	2.39	0.95	1.53	1.36	±0.31	±20.3	2.63
Diagrid	48.2	1.62	2.39	0.96	1.65	1.49	±0.29	±17.5	2.11
Reinforced	48.2	1.62	2.39	0.93	1.92	1.61	±0.27	±14.1	2.38
Auxetic	48.2	1.62	2.39	0.97	1.88	1.55	±0.23	±12.2	1.98
Untextured	48.2	1.62	2.39	0.72	0.96	0.86	±0.49	±51.1	5.03

From these results, all textured SECs performed consistently better compared to the untextured SECs by showing a significant increase in linearity, sensitivity, and resolution, and accuracy over all crack lengths. The auxetic pattern outperformed in linearity and resolution by exhibiting a 35% to 113% increase in R^2 and 222% to 319% increase in resolution with respect to the untextured sensors. The reinforced diagrid pattern outperformed in sensitivity (λ) and accuracy (σ_{res}) by exhibiting a 69% to 100% increase in the gauge factor λ and 111% to 582% improvement in accuracy with respect to untextured SECs. Relative results for λ had the same rank as found in the crack sensitivity (P2P) study, and those for the resolution had the same rank as found in crack detection performance. All SEC sensors exhibited a relatively poor resolution under the 0 mm crack length case (undamaged), attributable to the very small level of localized strain.

Multifunctional Soft Stretchable Strain Sensor

Tensile Test

Quasi-static tests were designed to characterize the sensor under a free-standing configuration. Sensors were customized in rectangular-shaped thin-film specimens, each of 56 mm length, 8 mm width, and 0.15 mm thickness, for an aspect ratio of 7:1. Experimental tests were conducted using an Instron 5544A tensile tester equipped with a 10 N load cell (shown in Figure 3.10a).

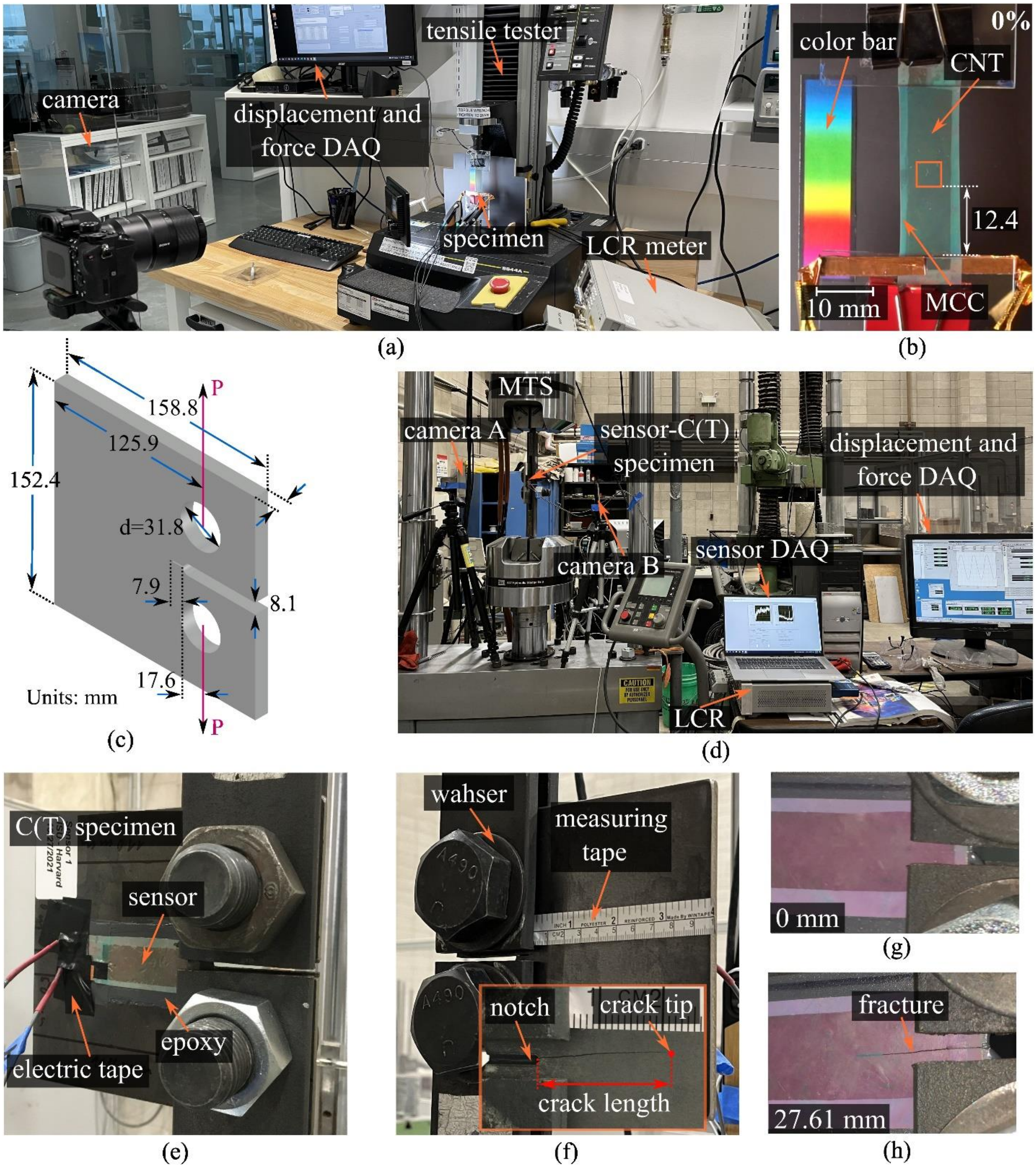

Figure 3.10. (a) Experimental setup of the free-standing test, (b) close-up view on the free-standing sensor (front view), (c) geometry of the C(T) specimen, (d) overall experimental setup for fatigue crack test, (e) close-up view of the front surface of the sensor-C(T) specimen, (f) close-up view of the back surface of the sensor-C(T) specimen, (g) sensor under 0 mm crack length, and (h) sensor under 27.61 mm crack length

Both ends of the sensor were gripped between two clamping fixtures and mounted onto the load cell. Three independent specimens were prepared and each were initially pre-strained at 50 mN to eliminate slack before testing. A first series of tests was conducted by applying uniaxial tensile strain along the longitudinal direction at a linear rate of 1% s^{-1} and stopped at 40% strain.

A second series of tests consisting of cyclic loadings was conducted by subjecting the sensor to a 0.1 Hz excitation at 0.5%, 1%, 2%, 3%, 4%, 5%, 10%, 20%, 30%, and 40% strain through five cycles applied under each strain level. A 10-second pause was applied at the peak amplitude of the third cycle under each strain level to allow an investigation of the signal-to-noise ratio (SNR). Capacitance data was recorded at 100 Hz using an inductance (L), capacitance (C), and resistance (R) meter (LCR meter) (Keysight E4980A), and the sensor's surface/apparent color under normal white light was simultaneously recorded using a digital camera with a frame rate of 30 fps during the cyclic loading process.

To allow a direct investigation of the mechanical properties of the structural color film, three of these films were customized to the same size and the mechanical properties were characterized by following the same experimental procedure. The color reflectance of the structural color film under different strain levels was measured using an optical fiber setup connected to an Ocean Optics HR2000+ spectrometer, and the measurements were carried out both before and immediately after film straining.

Fatigue Crack Test

The performance of the sensor at detecting and quantifying fatigue cracks was examined on C(T) specimens. The experimental test was conducted by following the same procedure as previously demonstrated in Liu et al. (2021a). Figure 3.10d shows the experimental setup.

Two mobile phone cameras (A and B) were placed on the back and front sides of the sensor-C(T) specimen to simultaneously record the crack length and sensor's color during the loading process at frame rates of 30 fps for both. Load and displacement were recorded using the LVDT of the MTS machine with a sampling frequency of 20 sample s^{-1}, and capacitance data were collected at 10 samples s^{-1} using an LCR meter (Agilent 4263B) at a 1 kHz measuring frequency driven in the LabVIEW environment. Wires were fixed with electrical tape to create an electrically insulating barrier and minimize the electrical noise caused by cable movement. In this study, crack length was defined as the distance measured from the notched edge to the crack tip (indicated as a red dot in Figure 3.10f, where a fatigue crack of 20.1 mm was observed and photograph taken at cycle 13,059). Tests ran continuously until the maximum displacement of the MTS machine reached 25.4 mm (1 in.). Slight lateral torsion-induced out-of-plane deformations were observed on the C(T) specimen for crack lengths beyond 38.1 mm.

Structural Similarity Index Measurement (SSIM)

The SSIM is a perceptual metric used to measure and quantify visual similarity between images (Sara et al. 2019, Peng et al. 2020). Mathematically, the SSIM is computed as the weighted combination of the luminance contrast, and structure similarity between two images p and q (Brooks et al. 2008), given as follows:

$$SSIM(p,q) = [k(p,q)^{\alpha} \cdot [c(p,q)^{\beta}] \cdot [s(p,q)^{\gamma}] \tag{10}$$

where k is the luminance used to compare the brightness between both images, c is the contrast used to differ the ranges between the brightest and darkest region of both images, s is the structure used to compare the local luminance pattern to find the similarity and dissimilarity between both images, and α, β, and γ are positive constants. The luminance, contrast, and structure of an image can be separately expressed as follows:

$$k(p,q) = \frac{2\mu_p\mu_q + C_1}{\mu_p^2 + \mu_q^2 + C_1} \tag{11}$$

$$c(p,q) = \frac{2\sigma_p\sigma_q + C_2}{\sigma_p^2 + \sigma_q^2 + C_2} \tag{12}$$

$$s(p,q) = \frac{2\sigma_{pq} + C_3}{\sigma_p\sigma_q + C_1} \tag{13}$$

where μ_p and μ_q are the local mean of p and q, σ_p and σ_q are the standard deviations of p and q, and σ_{pq} is the cross-covariance for images p and q, respectively (Kumar and Moyal 2013). By substituting equations 9 through 11 into equation 8 and assigning $\alpha = \beta = \gamma = 1$, the *SSIM* can be is simplified as follows:

$$SSIM(p,q) = \frac{(2\mu_p\mu_q + C_1)(2\sigma_p\sigma_q + C_1)}{(\mu_p^2 + \mu_q^2 + C_1)(\sigma_p^2 + \sigma_q^2 + C_2)} \tag{14}$$

Results and Discussion

Figures 3.11a–f present images taken from the recorded experiment under ambient conditions (normal white light), showing the multifunctional sensor’s apparent color at slack, and under 1%, 8%, 20%, 30%, and 40% strains, respectively. Here, the applied strains result in a remarkable and naked-eye observable color change from light blue to a deeper blue and finally to cold white.

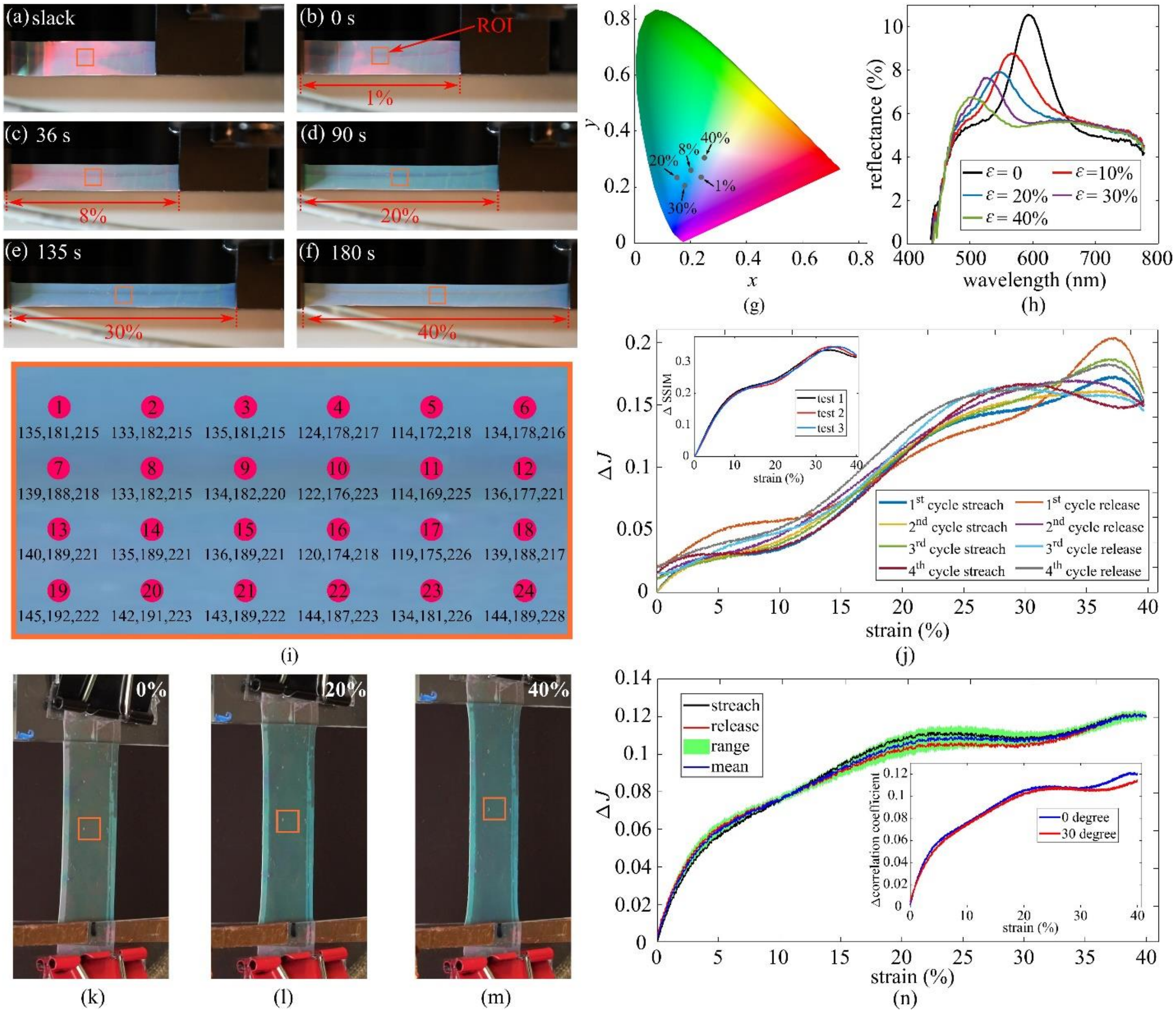

Figure 3.11. (a)–(f) Structural color film at 0%, 1%, 8%, 20%, 30%, and 40% strain under ambient condition; (g) measured reflectance spectra of the structural color film at different strain levels; (h) CIE 1931 color space chromaticity plotting the color change of structural color film at different strains; (i) 24 color points organized RGB matrix of the first frame (0% strain); (j) Δ*J* as function of strain for the structural color film during the stretch and release processes of the first four cycles, with the inset showing the change in SSIM (Δ*SSIM*) in the defined ROI; (k)–(m) digital photos showing the apparent color of the sensor at (k) 0, (l) 20%, and (m) 40% strain; and (n) change in correlation (Δ*J*) versus applied strain of the sensor during the stretch and release processes with the inset comparing the mean Δ*J* curves computed from 0° and 30° measurements

The Commission Internationale de l’Éclairage’s (CIE’s) coordinate system was used to define the color coordinates, and the calculated CIE 1931 color space chromaticity of the structural color film at different strain levels are plotted in Figure 3.11g. It can be observed that the coordinates change with increasing strain and is evident for optical strain sensing.

The light scattering behavior of the multifunctional sensor at different strain levels are displayed in Figure 3.11h. A distinguishable peak in diffuse reflectance was observed at each stretch level, and all reflectance peaks are centered around the wavelength of approximately 500 to 650 nm, characteristic of the turquoise color. The measured wavelength of the peak intensity gradually decreased with the increase of strain, while the peak intensity in diffuse reflectance decreased 20.5% when stretching of the color film from 0% to 10% strain, indicating a higher optical sensing sensitivity over that strain range.

To investigate the reversibility of the color changes during the loading and unloading cycle, an 8 mm × 8 mm square-shaped region at the center of the sensor, where the axial deformation is the most uniform and the observed color change is the most homogeneous, was defined as a region of interest (ROI), identified by the orange box in Figures 3.11a–f. The 8 mm length selected here corresponds to a 14.28% gauge length, achieving an ROI with dimensions comparable with the width of the sensor. After, 24 color points were uniformly assigned on the defined ROI, indicated as red dots in Figure 3.11i, to identify the red, green and blue (RGB) value on that location and formed as an RGB color matrix, as presented in Figure 3.11i.

The Pearson correlation coefficient J, which is computed as the ratio between the covariance of two RGB color matrices and the product of their standard deviations, was adopted as the color change indicator to measure the linear correlation between the surface color that appeared on each frame, written as follows:

$$J = 1 - \frac{E\left[\left(S_{i,k} - \mu_S\right)\right]\left[S_{i,j}^0 - \mu_S^0\right]}{\sigma_S \sigma_{S^0}} = 1 - \frac{\sum_{i,k}\left(S_{i,k} - \mu_S\right)\left(S_{i,j}^0 - \mu_{S^0}\right)}{\sqrt{\sum_{i=1}^{n}\left(S_{i,k} - \mu_S\right)^2}\sqrt{\sum_{i=1}^{n}\left(S_{i,j}^0 - \mu_{S^0}\right)^2}} \tag{15}$$

where $S_{i,j}$ and $S_{i,j}^0$ are the RGB matrices of the first frame and the compared frame, E is the expected value, μ_S and μ_{S^0} are the means of $S_{i,j}$ and $S_{i,j}^0$, and σ_S and σ_{S^0} are their standard deviations, respectively.

The results of the change in correlation coefficients (ΔJ) during the stretch and release processes of the first four cycles are presented in Figure 3.11j. A non-linearity after 30% strain can be observed, which can be explained by the edge effects. Additionally, the highest value for ΔJ was obtained between approximately 40% to 30% strain during the strain release phase of the first cycle, indicating a path-dependent color change after the first cycle of stretching. A positive and approximately linear relationship was observed between the change in correlation coefficients and the applied strain, and an optical gauge factor of 0.53 was found from the slope of the linear regression conducted in the 0% to 30% strain range.

The defined ROI was used for cropping and extracting images used for color change analysis. The plot of the computed change in SSIM ($\Delta SSIM$) between the first frame and each other frame is shown in the inset of Figure 3.11j. Results in the plot are taken from the stretch during the second cycle of three tests conducted on three independent specimens. The overlap and close agreement between the experimental data measured from three independent specimens were evaluated by comparing the area below each SSIM curve that resulted from the stretch and release process. The enclosed area remained in the range of 6.11 to 6.29 during the stretch and release process, illustrating the repeatability of the color change on the structural color film. A similar underlying trend between the RGB correlation loss and the computed *SSIM* was observed, evident in the strain-induced color change on optical response.

Figure 3.11b is a digital photo taken from the front view (0°) showing the surface color of the free-standing sensor under 0% strain. An 8 mm × 8 mm ROI with 24 colors is also assigned for creating RGB matrices. Results for ΔJ taken from the stretch and release process during the first cycle are presented in Figure 3.11n as a function of strain, with the green area illustrating the range measured over 10 cycles and with the blue curve representing the mean value. To illustrate the angle independence of the strain-dependent color change, the experiment was recorded under an angle of 30° normal to the sensor. Figures 3.11k–m are digital images taken from that angle, showing the color of the free-standing sensor under 0%, 20%, and 40% strain. Results from the mean ΔJ curve was compared against those measured from front view (0°) and presented in the inset of Figure 3.11m. An RMSE value of 2.39% was found over 0% to 30% strain, demonstrating an angle-independent color change.

The sensing performance of the sensor was investigated by evaluating the signal's linearity, gauge factor, capacitance versus strain match, and resolution. Figure 3.12a presents a time series plot of the relative change in capacitance $\Delta C/C_0$ versus applied strain at a rate of 1% s^{-1}.

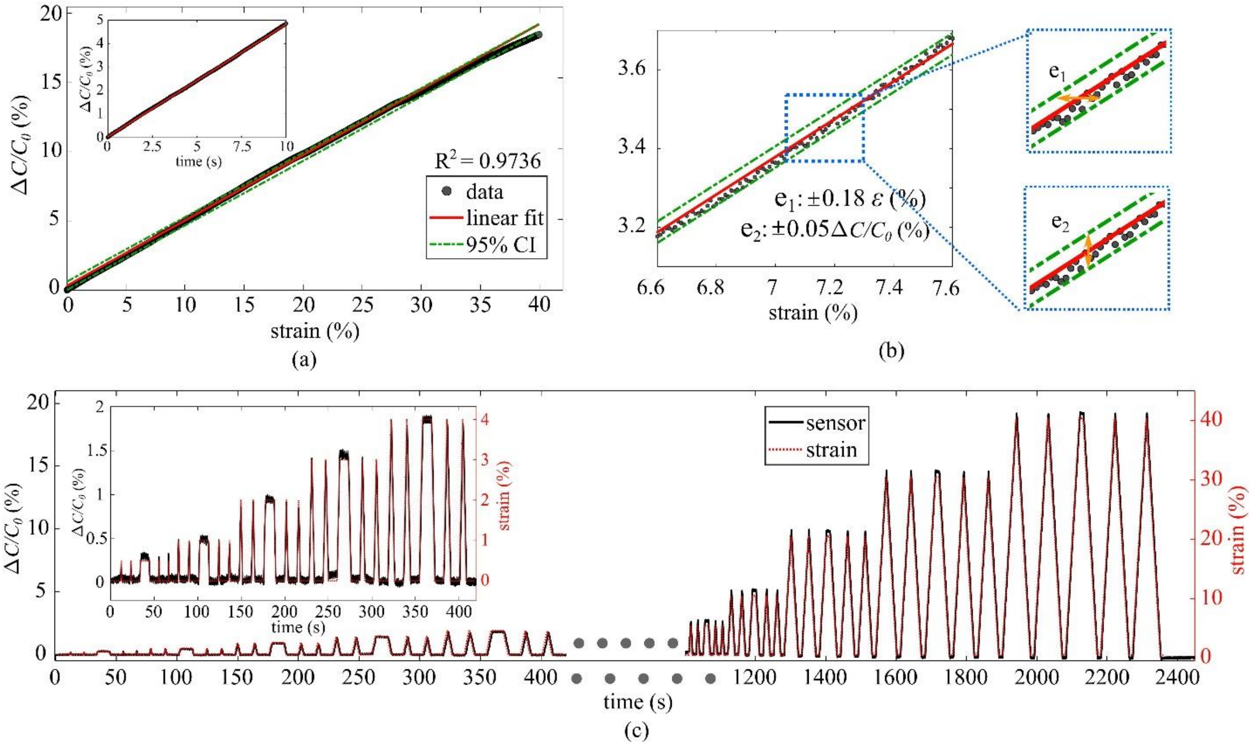

Figure 3.12. (a) Quasi-static tensile test results over 40% strain level, (b) strain accuracy resulted from the capacitance error bounds, and (c) time series response of the sensor under cyclic loading (superimposed)

Results exhibit excellent linearity up to 35% and an RMSE of 97.36% over the full 40% strain range, and the gauge factor obtained using the linear fit over the 10% strain range (inset of Figure 3.12a) is $\lambda = 0.49$, taken as the slope of the fit. Figure 3.12b presents the strain accuracy e_1 ($\pm 0.18\ \varepsilon$) and capacitance error bounds e_2 ($\pm 0.05\ \Delta C/C_0$), both computed from the linear fit over 10% strain.

Figure 3.12c plots the relative change in capacitance $\Delta C/C_0$ compared against the strain input under cyclic loading with the strain level successively increasing to 0.5%, 1%, 2%, 3%, 5% and up to 40%. Results show good agreement between both signals, with an RMSE of 3.88% and an overall SNR value of 10.62 dB, indicating the strain tracking capability and the high quality in signal. The 95% CI bound in terms of strain and relative change in capacitance yields an accuracy of $\pm 0.65\ \mu\varepsilon$, and $\pm 0.29\ \Delta C/C_0$.

Figures 3.13a through c presents digital photos taken from the video recorded continuously during the fatigue tests. Selected photographs show that the color changes on the sensor under a large opening, no opening, and a small opening for a crack length of 16.3 mm taken at 10,361 cycles.

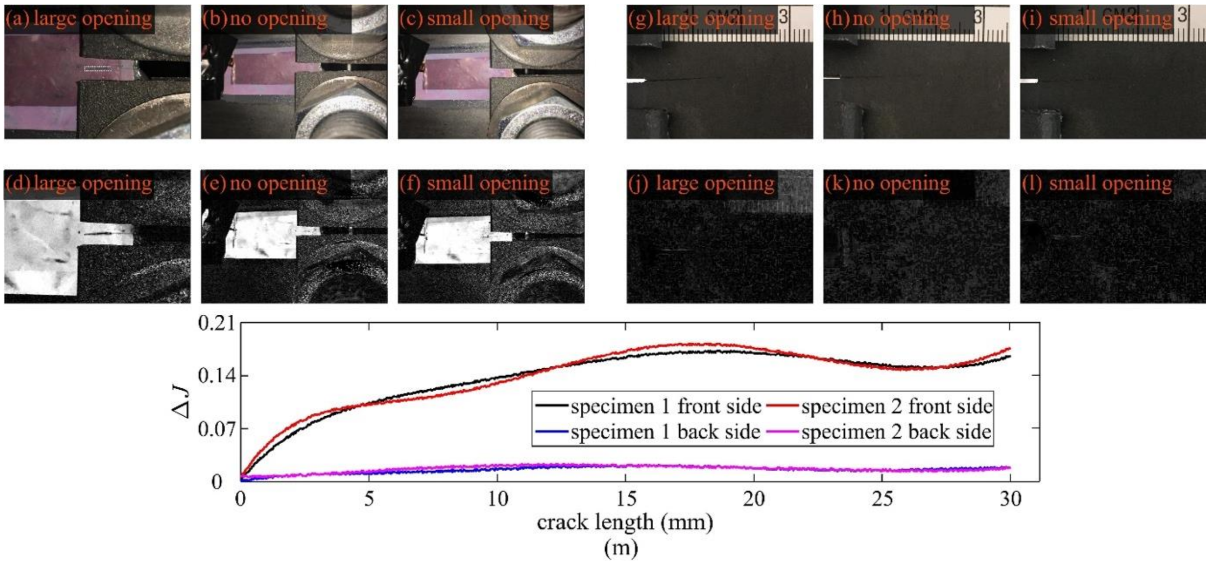

Figure 3.13. (a–c) Sensor under a crack length of 16.3 mm (at 10 361 cycles): large crack opening, no crack opening, and small crack opening; (d–f) CIE 2000 processed images of a–c; (g–i) back surface of the C(T) under a crack length of 16.3 mm (at 10 361 cycles): large crack opening, no crack opening, and small crack opening; (j–l) CIE 2000 processed images of g–i; and (m) comparison of the change in correlation (ΔJ) computed from the front side (sensor) and back side (no sensor) of the C(T) specimen

A color change of the sensing area above the cracking area was observed under the cross-crack strain provoked by the opening of the crack. The digital photos are further processed with CIELAB-based color-difference formulas (CIE 2000) in MATLAB to improve the accuracy of observed color differences through the introduction of various corrections in CIELAB. Results of the processed photographs are shown in Figures 3.13d–f. Differences in the sensor's apparent color can be observed even under a small crack opening. Figures 3.13g–i are images taken from the back side of the C(T) specimen that correspond to Figures 3.13a–c, emulating pictures that would be taken during a traditional inspection. Those photographs are also processed with the CIE 2000 coordinate, and the resulting photographs are shown in Figures 3.13j–l. By comparing the processed photographs of the sensor (Figures 3.13d–f) and the back side of the C(T) specimen (Figures 3.13j–l), it can be seen that the sensor improved visual capabilities to observe a fatigue crack. Figure 3.13m is a plot comparing ΔJ taken over the front side (sensor) and back side (no sensor) specimen, for both tested specimens. Results clearly show that the utilization of the sensor permits better optical discovery of a fatigue crack, as well as better characterization of the fatigue crack length.

Figure 3.14a plots a capacitance time history across the entire loading/unloading process, and the inset presents capacitance versus strain input under a crack length of 30.6 mm.

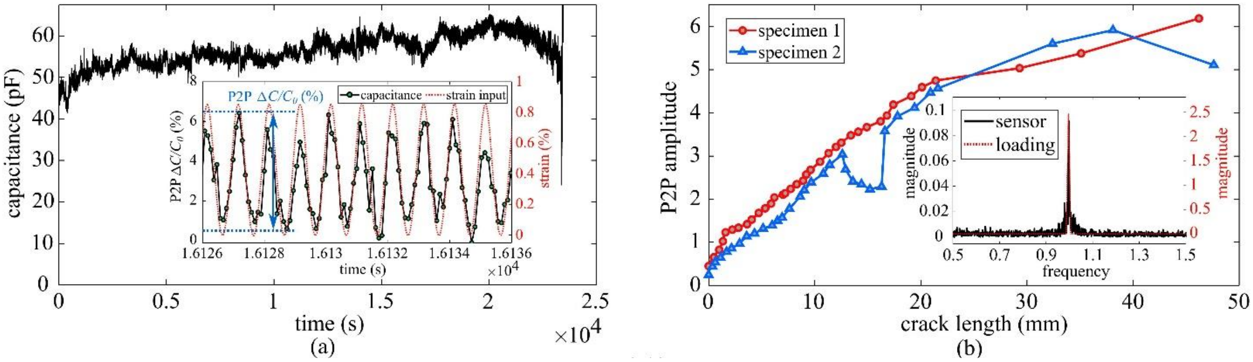

(a)
(b)

Figure 3.14. (a) Time series of raw capacitance data under designed fatigue loading protocol and (b) P2P amplitudes of the relative change in capacitance ΔC/C0 under different crack lengths, with the inset showing the frequency spectra of the sensor and the loading

The upward drift in the capacitance data can be explained by the plastic deformation of the C(T) specimen, where the minimum crack opening increased as the crack propagates. A P2P relative change in capacitance $\Delta C/C_0$ amplitude (illustrated in the inset of Figure 3.14a) was extracted as a signal feature to quantify the localized strain provoked by the closing and opening of the crack, which corresponds to the actual strain experienced by the sensor. This strategy corrects for drifts caused by calibration and in-field environmental effects. Note that the long-term performance of the device with respect to environmental effects is left to future work.

Figure 3.14b presents the P2P amplitudes extracted from both tested specimens over different crack lengths, where the P2P amplitudes are taken as the averaged values of 100-second measurements under a given crack length. An overall increase in P2P amplitudes is observed with the increase of the crack length. The increments of the P2P amplitudes under a unit crack length decreased after approximately 20 mm crack length, which can be attributed to the potential delamination of the sensor and rupture of the sensing area during the experiment, as shown previously in Figure 3.10h, taken under a crack length of 27.61 mm. The inset of Figure

3.14b compares the frequency spectrum of the sensor's signal and MTS-derived inputs (i.e., force input), where the input frequency of 1 Hz is observable.

Figures 3.15a–d plot the averaged relative change in capacitance from both specimens as a function of the crack-induced strain under crack lengths of 0, 6.2, 12.5, and 20.1 mm.

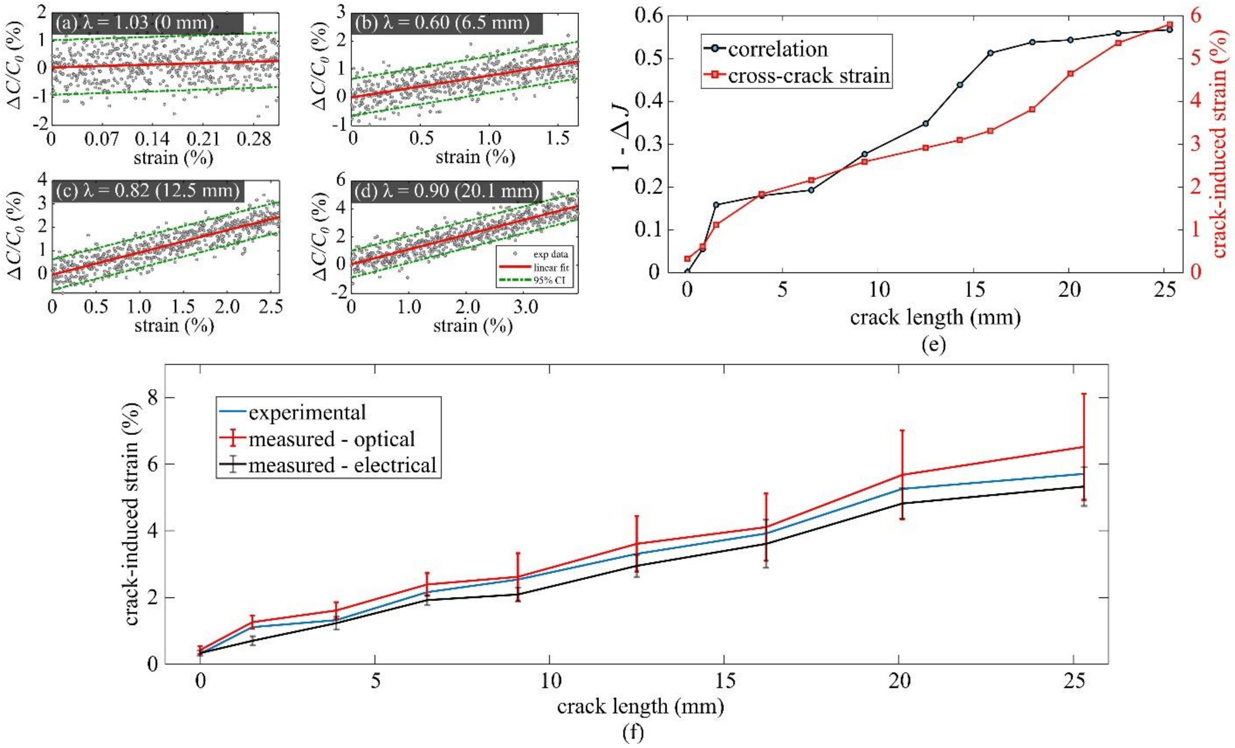

Figure 3.15. (a–d) Two sample-averaged relative change in capacitance ($\Delta C/C_0$) as a function of cross-crack strain under crack lengths of (a) 0, (b) 6.2, (c) 12.5, and (d) 20.1 mm, also presenting the gauge factors and signal matching error for with 95% CI; (e) correlation coefficients (black solid line) between the 20 color patches organized RGB matrices resulted from the cracking and noncracking area, along with the corresponding cross-crack strain levels (red dot line) under different crack lengths; (f) comparing of cross-crack strain measured from numerical model, optical sensing, and capacitance sensing under different crack lengths

The crack-induced strain is the localized strain provoked by the closing and opening of the crack and is a better representation of the strain experienced by the sensor. These values are computed from an FEM under the corresponding crack lengths. The FEM for the test configuration was presented and validated in previous work (Liu et al. 2021a). Results show the linear fit (red solid line) obtained from least squares regression, along with the resulting 95% CI bounds (green dashed line) representing the resolution. The computed gauge factors λ are listed in each subfigure.

Table 3.3 assembles the quantitative results over nine representative crack lengths, listing the load-derived strain from the MTS machine (MTS-strain), crack-induced strain, MTS-derived to crack-induced strain ratio, linearity through the quality of the linear regression fit (R^2), gauge factors (λ) computed from MTS-derived strain and crack-induced strain, resolution through the 95% CI in terms of the relative change in capacitance and equivalent strain levels computed using equation 8 with MTS-induced λ, and standard derivation on the resolution (σ_{res}) measured from specimens 1 and 2.

Table 3.3. Experimental results characterizing fatigue crack sensing performance

							95% CI		
Crack length (mm)	MTS strain (%)	Crack strain (%)	Strain ratio (%)	R^2 (−)	MTS λ (−)	Crack λ (−)	$\Delta C/C_0$ (−)	resolution ($\mu\varepsilon$)	σ_{res} (−)
0	0.39	0.31	125.81	0.19	0.82	1.03	±1.072	±90.8	30.12
1.5	0.43	1.11	37.74	0.23	1.59	0.62	±1.101	±69.2	26.71
6.5	0.56	2.16	25.93	0.46	2.32	0.60	±1.051	±45.3	22.98
12.5	0.79	3.31	27.01	0.52	3.03	0.72	±0.953	±31.4	24.43
20.1	0.88	5.26	18.96	0.64	4.77	0.79	±1.166	±27.4	20.77
29.3	0.97	6.44	15.06	0.87	5.05	0.76	±1.315	±26.0	19.29
35.1	1.16	8.39	13.83	0.95	4.48	0.62	±1.131	±28.2	21.38
41.9	1.41	10.56	13.35	0.91	3.78	0.50	±1.005	±26.6	18.61
47.6	1.62	13.11	12.36	0.93	3.15	0.39	±0.961	±30.5	19.09

Results show that both the MTS-derived strain and crack-induced strain are increasing with the extension of the crack length but with the crack-induced strain increasing at a higher rate, resulting in a decrease of the strain ratio as the crack propagates. Values for R^2 and the crack-induced λ respectively exhibit an overall good linearity and sensitivity, especially under a large strain. However, a relatively poor linearity was observed under the 0 mm crack (no crack), given the nonexistent crack-induced strain. The slightly lower crack-induced λ under large crack lengths (41.9 and 47.6 mm) can be attributed to the loss in the geometric sensing area. The resolution of the signal and accuracy (σ_{res}) improved with the increase in crack length, where the accuracy is computed as the standard deviation of data under a given crack length.

The performance of the multifunctional sensor is compared against that of a more mature parallel-plate capacitor (cSEC) reported in prior work on the exact same experimental setup (Liu et al. 2021a). Results are tabulated in Table 3.4.

Table 3.4. Sensing performance versus cSEC under 0, 11.1, and 48.2 mm crack lengths

	Crack length (mm)	multif. (sensor)	cSEC
R^2 (–)	0	0.19	0.17
	11.1	0.51	0.83
	48.2	0.93	0.97
95% CI $\Delta C/C_0$ (–)	0	±1.07	±0.59
	11.1	±0.94	±0.29
	48.2	±0.96	±0.23
95% CI resolution ($\mu\varepsilon$)	0	±90.8	±71.9
	11.1	±32.6	±49.2
	48.2	±30.3	±12.2
σ_{res} ($\mu\varepsilon$)	0	30.12	25.64
	11.1	23.39	4.78
	48.2	18.52	2.77
min. crack length (mm)	—	0.84	0.28

The comparison showed that generally the multifunctional sensor underperforms the cSEC probably due to its early stage of development. However, the reported values remain similar to those reported under the cSEC, except for the variance of the resolution, where the multifunctional sensor underperforms by one magnitude.

The optical strain sensing properties of the sensor is evaluated on an $l \times w = 5 \times 1$ mm^2 rectangular ROI located above the crack with 20 color points uniformly assigned within the region. The loss in correlation coefficients (1-ΔJ) between the RGB matrices that are computed under different crack lengths are presented in Figure 3.15e. It can be observed that the loss in correlation increases following a trend similar as a function of crack length to that of the crack-induced strain, consistent with the findings from the tensile tests conducted on the structural color film. This illustrates the capability of the sensor at optically localizing and quantifying the crack.

Figure 3.15f is a plot comparing the crack-induced strain extracted from the numerical model using experimental data with measurements obtained from the optical and electrical (capacitance) signals. Values are presented as the average from both specimens. The optical-derived values were computed using the curves previously shown in Figure 3.11n, and the electrical-derived values were computed using the gauge factor λ characterized from the prior tensile test. The error bars added to the optical measurements show the strain resolutions, and the error bars added on the electrical-derived values indicate the minimum to maximum range over both specimens. Both optical and electrical sensing capabilities agree with the experimental data, with the optical response slightly overestimating crack-induced strain, while the electrical feedback slightly underestimates it.

Angular Application

This subsection is extracted from the following publication:

Liu, H., S. Laflamme, J. Li, C. Bennett, W. N. Collins, A. Downey, P. Ziehl, and H. Jo. 2021. Soft Elastomeric Capacitor for Angular Rotation Sensing in Steel Components. *Sensors*, Vol. 21, No. 21, Article No. 7017.

Angular Motion Sensing

This study extends work on the cSEC to evaluate its performance at measuring angular rotation when installed folded at the junction of two plates. The objective is to characterize the sensor's electromechanical behavior anticipating applications to the monitoring of welded connections in steel components.

Electromechanical Model

In prior work, the cSEC was utilized to measure strain associated with in-plane deformation in the sensor, for instance, from pure axial elongations or widening of cracks. The electromechanical model of the sensor for in-plane deformation is derived as follows. Assuming a low measurement frequency (<1 kHz), the cSEC can be modeled as a non-lossy parallel plate capacitor of initial capacitance C_0:

$$C_0 = e_0 e_r \frac{A}{h} \tag{16}$$

where e_0 = 8.854 pF/m is the vacuum permittivity, e_r is the relative permittivity, h is the thickness of the dielectric, and A is the electrode area of length l and width d.

To derive the electromechanical model applied to angular motions, consider a small section of a cSEC as illustrated in Figure 3.16a.

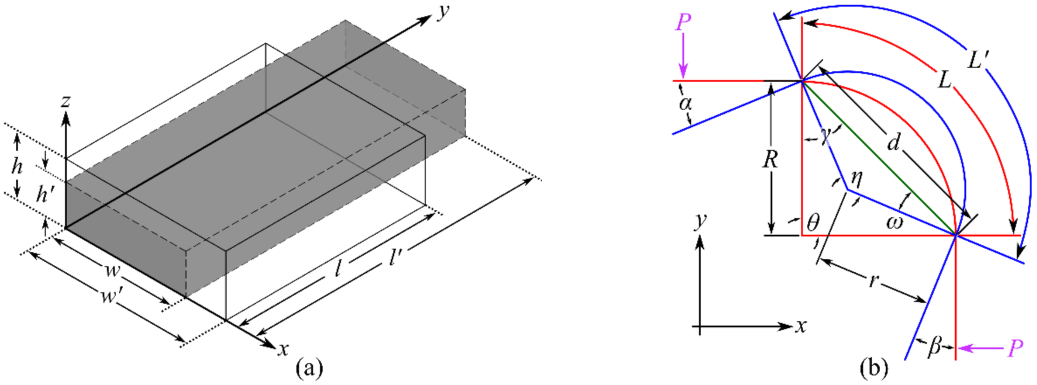

Figure 3.16. (a) Small cuboid unit of the mesh element and (b) deformation of an arc under compression

The section is of initial length l, width w, and thickness h, and the strain is assumed to be distributed uniformly along the section. An incremental stretch along the y direction produces a longer length l', smaller width w', and smaller thickness h', where the prime denotes a deformed dimension. Here, the capacitance response, $\Delta C/C_0$ can be expressed as follows:

$$\frac{\Delta C}{C_0}=\frac{C_1-C_0}{C_0}=\frac{e_0e_r(\frac{A'}{h'}-\frac{A}{h})}{e_0e_r\frac{A}{h}}=\frac{A'h-Ah\prime}{Ah\prime} \tag{17}$$

where C_1 is the capacitance and A_0 is the deformed sensing area of the deformed section. Substituting $A=lw$ and $A'=l'w'$ into equation 17, one obtains the following:

$$\frac{\Delta C}{C_0}=\frac{l'w'h-lwh\prime}{lwh\prime} \tag{18}$$

Differentiating equation 18 with respect to length l and width w, the capacitance response $\Delta C/C_0$ of the sensor becomes the following:

$$\frac{\Delta C}{C_0}=\left(\frac{l'-l}{l}+\frac{w-w'}{w}-\frac{h-h'}{h}\right)=\varepsilon_x+\varepsilon_y-\varepsilon_z \tag{19}$$

where ε_x and ε_y are the in-plane strains and ε_z is the out-of-plane strain. Substituting $l'=(1+\varepsilon_x)l$, $w'=(1+\varepsilon_y)w$, and $h'=(1+\varepsilon_z)h$ into equation 19, one obtains the following:

$$\frac{\Delta C}{C_0}=\frac{(1+\varepsilon_x)(1+\varepsilon_y)}{1+\varepsilon_z}-1 \tag{20}$$

Using Hooke's Law under plane stress assumption, for a plain (isotropic) SEC with Poisson's ratio ν, the strain along the z-axis can be written as follows:

$$\varepsilon_z = -\frac{\nu}{E}\left(\sigma_x + \sigma_y\right) = -\frac{\nu}{1-\nu}\left(\varepsilon_x + \varepsilon_y\right) = \frac{1}{(1+\varepsilon_x)(1+\varepsilon_y)} - 1 \tag{21}$$

Substituting equation 21 into equation 20 yields the following:

$$\frac{\Delta C}{C_0} = (1+\varepsilon_x)^2(1+\varepsilon_y)^2 - 1 \tag{22}$$

The corrugated surface alters the stiffness of the dielectric layer in the *x*-*y* plane and yields with a transverse Poisson's ratio ν_{xy} expressed, in a free-standing configuration, as follows:

$$\nu_{xy} = -\frac{\varepsilon_y}{\varepsilon_x} \tag{23}$$

When the sensor is fully adhered onto the monitored material, the composite effect on ν_{xy} needs to be considered (e.g., stiffness of the monitored material and level of adhesion). Here, the transverse Poisson's ratio under composite action $\nu_{xy,c}$ can be taken as follows:

$$\nu_{xy,c} = -\frac{-a\nu_{xy} + b\nu_m}{a+b} = -\frac{\varepsilon_{y,c}}{\varepsilon_{x,c}} \tag{24}$$

where ν_m is the Poisson's ratio of monitored material, $0 \le a \le 1$ and $0 \le b \le 1$ are weights such that $a + b = 1$, and $\varepsilon_{x,c}$ and $\varepsilon_{y,c}$ are the in-plane strains in *x* and *y* directions under composite action. When applied to steel, as it is the case in this study, $a \approx 0$ and $b \approx 1$. Substituting equation 24 into equation 22 yields the following:

$$\frac{\Delta C}{C_0} = \left(1+\varepsilon_{x,c}\right)^2(1-\nu_{xy,c}\cdot\varepsilon_{x,c})^2 - 1 \tag{25}$$

Assuming that the majority of strain deformation ($\varepsilon_{x,c}$) in the sensor is attributed to the rotation of the arc-length, and equation 25 can be further refined by evolving with the angular rotation. Figure 3.16b is the diagram of an arc of initial arc angle θ and chord length *d*. In the experimental section, values of θ = 89.85° and θ = 90.05°, and *d* = 10.2 mm and *d* = 10.1 mm were obtained for the left and right corners, respectively. The initial arc length *L* can be written as follows:

$$L = \theta \cdot R = \theta \cdot \frac{d\cdot\sin(\gamma)}{\sin(\theta)} = \theta \cdot \frac{d\cdot\sqrt{\frac{1-\cos\,(180-\theta)}{2}}}{\sin\,(\theta)} \tag{26}$$

where *R* is the radius of curvature and $\gamma = (180-\theta)/2$.

Consider two concentrated loads *P* acting at the free ends of the arc, and the deformed arc central angle and radius are η and *r*, respectively, as illustrated in Figure 3.16b. Angle η can be expressed as a function of the angular rotation α and β (also known as angle of rotation, angle of inclination, and angle of slope) written as follows:

$$\eta = \theta + \alpha + \beta \tag{27}$$

where α and β are the angle of rotations between the *x*- and *y*-axes and the tangent at the tip of the deflected arcs in the *x* and *y* directions, respectively. The deformed arc length *L'* can be expressed as follows:

$$L' = \eta \cdot r = (\theta + \alpha + \beta) \cdot \frac{d \cdot \sin(\omega)}{\sin(\eta)} = (\theta + \alpha + \beta) \cdot \frac{d \cdot \sqrt{\frac{1-\cos(180-\theta-\alpha-\beta)}{2}}}{\sin(\theta+\alpha+\beta)} \tag{28}$$

with the following:

$$\omega = \frac{180-\eta}{2} = \frac{180-\theta-\alpha-\beta}{2} \tag{29}$$

It follows that $\varepsilon_{x,c}$ in equation 25 can be taken as bending strain ε_x and written as the function of *L* and *L'* derived in equations 26 and 28 and given as follows:

$$\varepsilon_{x,c} = \varepsilon_x = \frac{\Delta L}{L} = \frac{L'-L}{L} = \frac{\left((\theta+\alpha+\beta) \cdot \frac{d\sqrt{\frac{1-\cos(180-\theta)}{2}}}{\sin(\theta+\alpha+\beta)} - \theta \cdot \frac{d \cdot \sqrt{\frac{1-\cos(180-\theta-\alpha-\beta)}{2}}}{\sin(\theta)}\right)}{\theta \cdot \frac{d \cdot \sqrt{\frac{1-\cos(180-\theta)}{2}}}{\sin(\theta)}} \tag{30}$$

Angular Rotation Index (ARI) Algorithm

The ARI algorithm is developed to fuse cSEC data into a scalar relating to the angle of rotation. The algorithm includes four consecutive steps, illustrated in Figure 3.17 and discussed in this section.

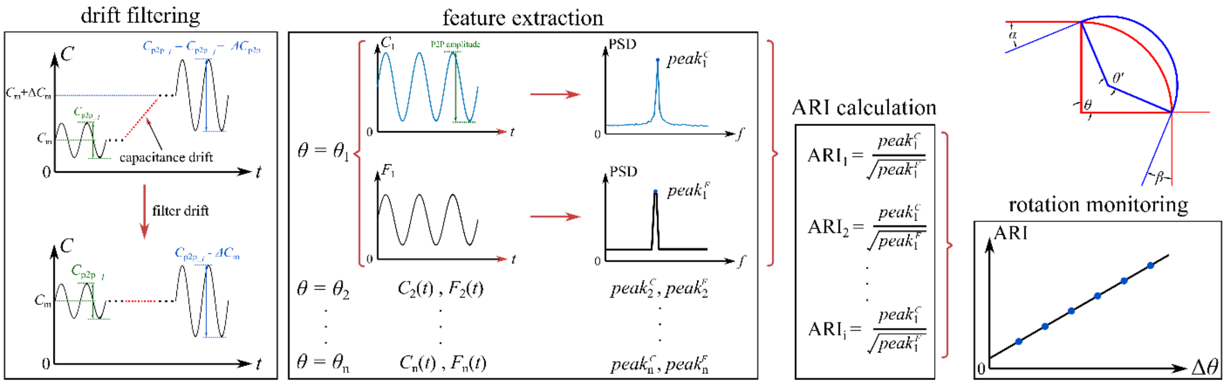

(a) (b) (c) (d)

Figure 3.17. Four-step algorithm used on monitoring angle of rotation: (a) data acquisition and drift filtering, (b) feature extraction, (c) construction of ARI, and (d) rotation monitoring

The first step consists of filtering drifts out of the measurements, a common issue found in strain gauges used over long periods of time (Figure 3.17a). To do so, the change in mean capacitance ΔC_m is computed and subtracted from each measurement segment to align signals with the initial mean capacitance C_m. In field applications, the cSEC may be affected by variations in temperature and humidity. These environmental effects can be filtered out, for example, through the design of a Wheatstone bridge configuration (Jeong et al. 2018a, 2018b).

The second step consists of extracting features (Figure 3.17b). These features correspond to the peak amplitudes of capacitance (peak_i^C) and force (peak_i^F) from the ith measurement taken in the power spectral density (PSD), as the frequency domain signal is less sensitive to the noise content of the measurements and used to represent the P2P amplitudes in the time domain. The utilization of these features is useful for filtering out signal drifts (e.g., temperature effects) and shifts (e.g., from a loose cable).

The third step consists of fusing features into the ARI (Figure 3.17c). Because the load range directly affects the P2P $\Delta C/C_0$ of the cSEC, peak_i^C is normalized by taking the ratio to the square root of the peak force $\sqrt{\text{peak}_i^F}$ to make the ARI input-independent, with the ARI of the ith measurement segment being ARIi = peak_i^C / $\sqrt{\text{peak}_i^F}$. The square root is taken in this equation to reduce heteroscedasticity of the residuals in linear regression and weaken the effect of the nonlinear relationship in equation 30. Mathematically, the ARI represents the level of the angular rotation induced by the P2P amplitude under a unit excitation load.

The fourth step consists of correlating the ARI with the angle of rotation (Figure 3.17d). This can be done by characterizing the relationship between ARI and $\Delta\theta$, therefore enabling the identification of $\Delta\theta$ online in real-time.

Experimental Test

The experimental study focused on characterizing the capacitance response of the cSEC in a folded configuration using a 101.6 mm × 101.6 mm × 3.175 mm hollow structural section (HSS) specimen (A500 Grade C). The HSS is used to mimic the curved surface of an orthogonal joint in a connection. Figure 3.18a shows the overall experimental setup, and Figure 3.18b is a close-up view of the front side of the HSS specimen.

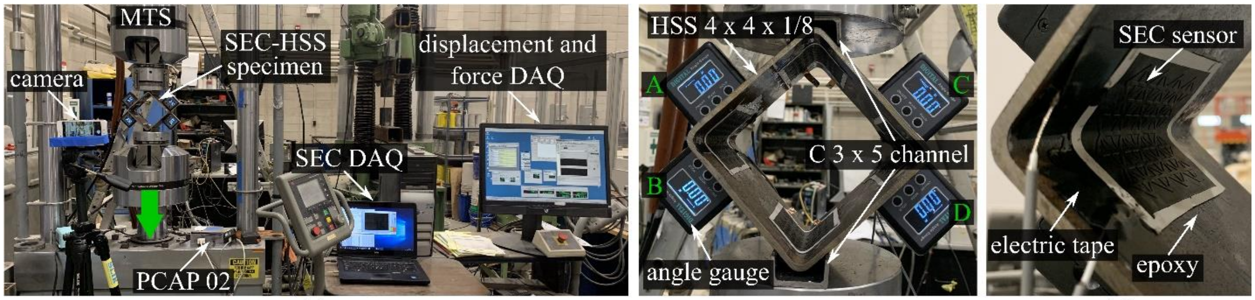

(a) (b) (c)

Figure 3.18. (a) Overall experimental configuration (green arrow indicates the loading direction), (b) zoom on the front side of HSS specimen, and (c) close-up view of the inner surface, right corner

The inner surface of the HSS specimen was sanded using 1000 grit sandpaper and cleaned with acetone. After, as shown in Figure 3.18c, four cSECs were glued in folded configurations by adhering the flat surface onto the inner surface of the curved corners using an off-the-shelf bicomponent epoxy (JB Weld) so that the sensor was in full contact with the arc surface, which allowed the measurement of angular motion. Wires were fixed with electrical tape to be electrically insulated. Two C 3 × 5 steel channels (Grade A36 steel) were placed over the top and bottom corners to affix the HSS to a closed-loop servo-hydraulic testing machine (MTS model 312.41 with a TestStar IIm controller) equipped with model 647 Hydraulic Wedge Grips. Four digital angle gauges (labeled with A, B, C, and D in Figure 3.18b), with a measurement resolution of 0.05° and a minimum reaction time of 0.1 seconds, were installed above and below the left and right corners to measure localized angular rotations. The measurements from each angle gauge were assigned to be negative for clockwise rotations and positive for counterclockwise rotations.

A preload of 0.05 kN was applied on the HSS specimen prior to each test to obtain a compression-compression mode, and the specimen was subjected to a displacement controlled harmonic excitation at a constant frequency of 1 Hz. Ten tests were conducted, each lasting 120 cycles, but at different displacement amplitudes: 0.5, 1, 1.5, 2, 2.5, 3, 3.5, 4, 4.5, and 5 mm. A digital camera was placed in front of the specimen to simultaneously record the angular rotations measured by the angle gauges during testing, and the frame rate was set as 30 fps. Load and displacement data were recorded from the MTS at 20 samples/second, and cSEC capacitance data was sampled at 80 samples/second using an off-the-shelf DAQ board (ACAM PCAP02).

Figure 3.19a is a typical time series plot of the raw data measured from the cSEC (installed at the right angle) compared against the numerical response under the maximum displacement of 4 mm.

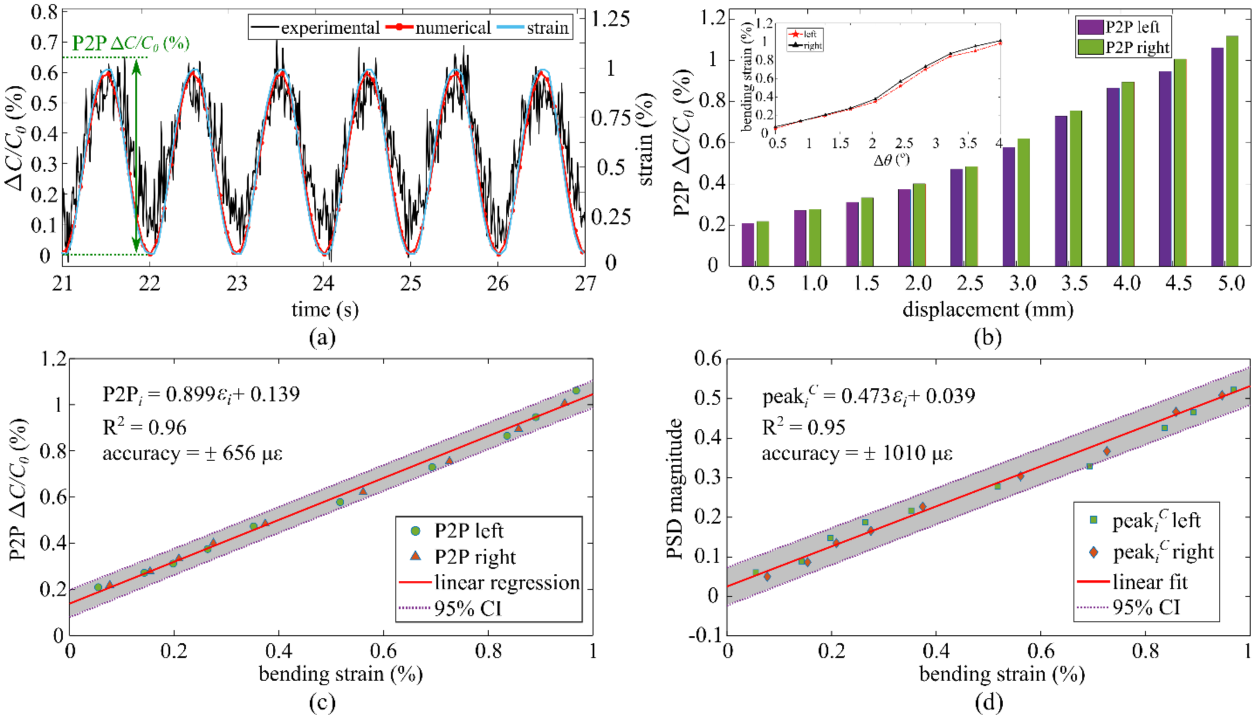

Figure 3.19. (a) Comparison of experimental and numerical signals for $\Delta C/C_0$ under a 4.0 mm maximum displacement, (b) P2P $\Delta C/C_0$ amplitude as a function of displacement with the inset showing bending strain as the function of angular rotations ($\Delta\theta$), (c) linear regression of the P2P amplitudes with respect to bending strain and (d) linear regression of the PSD amplitudes with respect to bending strain

The first 20 seconds were discarded to eliminate the early-stage noise in the signal. Quantities $\Delta\theta_C$ and $\Delta\theta_D$ were substituted into equation 30 as α and β to convert the measured angular rotation $\Delta\theta_R$ into bending strain $\varepsilon_{x,c}$, represented by the blue line in Figure 3.19a for which a linear interpolation was used to create a smooth curve. Strain obtained from the numerical capacitance response was also converted to bending strain ($\varepsilon_{x,c}$) and represented by a red-circle line in Figure 3.19a. There is a good fit between the experimental and numerical capacitance responses, with an RMSE value of 4.98%, showing that the electromechanical model can be used to estimate bending strain.

Figure 3.19b is a bar chart comparing the averaged 120 cycles P2P relative capacitance $\Delta C/C_0$ amplitudes (P2P illustrated in Figure 3.19a) under each maximum displacement, where a higher displacement correlates with a larger angular deformation and thus larger bending strain. It was found that the magnitudes of the P2P $\Delta C/C_0$ increase with increasing maximum displacement.

The inset in Figure 3.19b shows bending strain versus angular rotations ($\Delta\theta$), where bending strains were also calculated by using equation 30 with reported $\Delta\theta_i$ previously shown in Figure 3.18b.

Figures 3.19c and 3.19d plot the P2P $\Delta C/C_0$ and peak amplitudes of the PSD of capacitance (peak_i^C) as a function of bending strain, respectively. Fitted linear regressions have R^2 values of 96.1% (P2P $\Delta C/C_0$) and 94.9% (peak_i^C), and the 95% CI bounds result in an accuracy of ±656 με (P2P) and ±1010 με (PSD), respectively. This is significantly more than the levels reported in prior work on the cSEC under 54 με (Liu et al. 2021a) for measuring bending-induced and crack-induced strain over a flat surface. This could be explained by the change in local thickness of the cSEC, additional strain induced in the system that is ignored by the model, and the imperfect adhesion of the sensor during the hand-application process. However, it is evident that cSEC signal can be used to quantify the angular rotation-induced bending strain through a linear relationship. However, mapping the cSEC measurements to rotations is more difficult, as observed through equation 30 and the nonlinear relationship plotted in the inset of Figure 3.19b.

Figure 3.20 plots the computed ARI as a function of angle of rotations ($\Delta\theta$) for the left and right sensors. A desired linear relationship between the ARI and $\Delta\theta$ was found on both sets of measurements (left and right sensors), which verifies that the ARI could be used as a metric to quantify angular rotation. The 95% CI bound in terms of ARI and angular rotations $\Delta\theta_i$ yields an accuracy of ±0.416°, which compares well with off-the-shelf tiltmeters. Overall, the sensor led to large strain readings in the folded configuration with a poor resolution, but nevertheless the results from the ARI showed good accuracy in terms of degrees. Additional tests on different cross-section geometries would be required to further study the quality of the linear regression. This is left to future work. It should also be noted that this work only considered rotation-induced bending strain and that the presence of a fatigue crack, for instance if the sensor was installed over a corner weld, may induce additional kinetics. This is also left to future work.

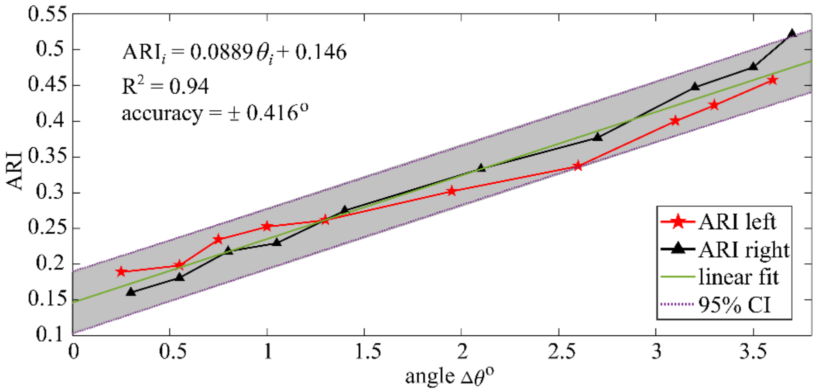

Figure 3.20. Linear regression of ARI with respect to angular rotation $\Delta\boldsymbol{\theta}_i$

Fatigue Crack Monitoring on Fillet Welds

Welding is a practical joining method widely employed in the fabrication of steel bridge components (e.g., assemble beams, channels, angles, plates, and other metal components) due to its low cost and reliability. However, the effect of service loads combined with residual stresses generated from the fast heating and cooling cycles during the welding process can significantly accelerate the formation of fatigue cracks (Oh et al. 2015).

Despite the fact that the importance of fatigue weldment cracking has been recognized and that numerous relevant research investigations have been conducted and reported since the 1920s (Farmer 1921), the detection of fatigue cracking in welds still mainly relies on visual inspections (Campbell et al. 2020, Campbell et al. 2021, Haagensen and Maddox 2013) and NDE techniques (e.g., thermography [Sakagami et al. 2016], ultrasonic testing [Amiri et al. 2020], x-ray imaging [Wu et al. 2016, Dong et al. 2021], magnetic particle testing [Zolfaghari et al. 2018], eddy-current testing [Gonchar et al. 2021], and acoustic emission monitoring [Yu et al. 2011, Yu et al. 2013, Chai et al. 2017]). However, both approaches usually require a trained practitioner, and timely detection is limited by the inspection schedule and quality of the inspection and/or NDE process.

The cSEC technology has been successfully demonstrated for measuring bending strain as well as angular rotation in a folded configuration. This study builds on prior discoveries to characterize the sensor's capability at monitoring fatigue cracks in corner welds, for which the sensor needs to be installed in a folded configuration. The objective is to characterize the cSEC signal when performing such a task, anticipating that discoveries will be useful to applications in the field and over complex geometries.

Damage Law

The Paris-Erdogan law (Newby 1991) is a well-utilized power model for characterizing and evaluating the fatigue crack propagation (FCP) rate. By considering the crack closure effect and the influence of welding residual stress, the FCP rate can be described as follows (Gadallah et al. 2018):

$$\left[\frac{da}{dN}\right]_{R_{eff}>1} = \left(\frac{U_{R_{eff}>0}}{U_{R_{eff}=0}}\right)^{m} . C(\Delta K_{eff})^{m} = \left(\frac{U_{R_{eff}>0}}{U_{R_{eff}=0}}\right)^{m} \cdot C(U_{R_{eff}=0} \cdot \Delta K)^{m} \tag{31}$$

where C and m are Paris' constants, and ΔK_{eff} is the effective stress intensity factor range defined as follows:

$$\Delta K_{eff} = U\Delta K = U(K_{Imax} - K_{Imin}) \tag{32}$$

where U represents the stress range ratio, taken as follows for structural steel (Kumar 1992):

$$U = 0.722 + 0.278\, R_{eff} \tag{33}$$

where R_{eff} is the effective stress ratio characterized by the stress intensity factors (e.g., K_{Imax} and K_{Imin}) and changes due to the presence of welding residual stress under cyclic load. The stress intensity range $\Delta K(K_{Imax} - K_{Imin})$ can be computed by using the equation defined in ASTM E2899-19e1, which is given as follows:

$$\Delta K = K_{Imax} - K_{Imin} = (H\sigma_b F_b)\left(\frac{\pi a}{1+1.464(\frac{a}{c})^{1.65}}\right)^{1/2} \tag{34}$$

where H and F_b are the combinations of correction factors, σ_b is the bending stress, a is the surface crack depth, and c is the half surface crack length.

Fatigue Loading Protocol

A value of 23 MPa$\sqrt{m}$ was selected for ΔK as the target stress intensity during the entire crack propagation process, consistent with ASTM E2899-19e1 requirements. An initial crack aspect ratio a/c of 0.1 (Mikulski and Lassen 2019) and residual stress induced effective stress ratio R_{eff} of 0.05, calculated using the procedure reported in Servetti and Zhang (2009), were selected to compute the stress range σ_b under different crack lengths through equations 31 through 34. Results are plotted in Figure 3.21a.

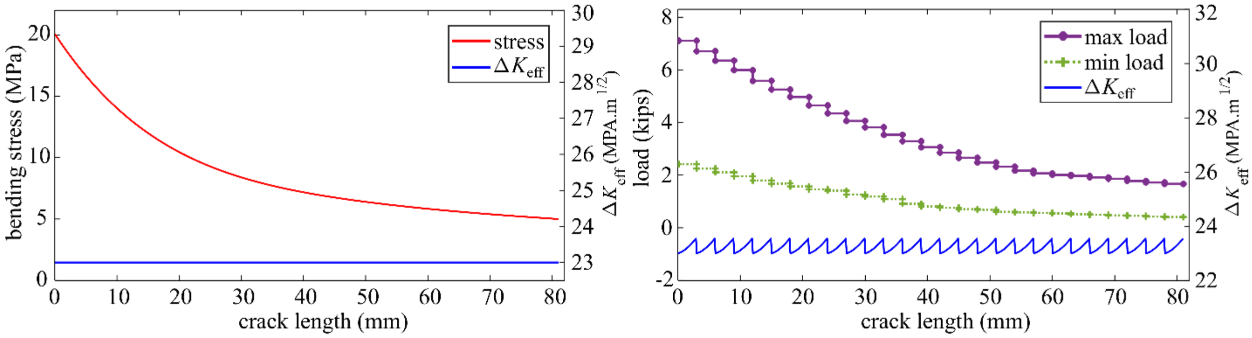

(a) (b)

Figure 3.21. (a) Computed bending stress as a function of crack length on fillet welds and (b) fatigue loading protocols characterized from FEM

Equation 34 implied that the bending stress σ_b can be determined once a selected ΔK is introduced, with a longer crack length c yielding a larger ΔK if σ_b is fixed. Therefore, the fatigue loading dominated by the designed bending stress σ_b is obtained from the constructed FEM by creating a crack growth path along the edge of the fillet weld to extract bending stresses, as shown in Figure 3.22a. The results extracted along the defined path under a 0.1 mm crack are plotted in Figure 3.22b with the red line representing the average value along the path. It can be observed that approximately 40% higher stress is concentrated at both ends of the fillet weld under compression, which corresponds to the position of the fatigue crack initiation observed during the experiments.

A stress ratio $R = \sigma_{max}/\sigma_{min}$ of 0.3 was selected and used to represent the ratio of live load-induced stress (i.e., vehicle load) to the dead load-induced stress (i.e., bridge self-weight) over one load cycle (Kong et al. 2017b). Values for F_{max} and F_{min} can be obtained from the numerical model by taking the average values of the yielded bending stress on the defined crack path equal to the calculated bending stress (shown in Figure 3.21a). A multistage loading protocol was established in which F_{max} and F_{min} remain constant during each crack interval and are recomputed and adjusted at every 3 mm (0.12 in.) of crack growth, maintaining an approximately constant stress intensity ΔK_{eff} within a range of 23 MPa$\sqrt{m}$ to 23.6 MPa$\sqrt{m}$, as plotted in Figure 3.21b.

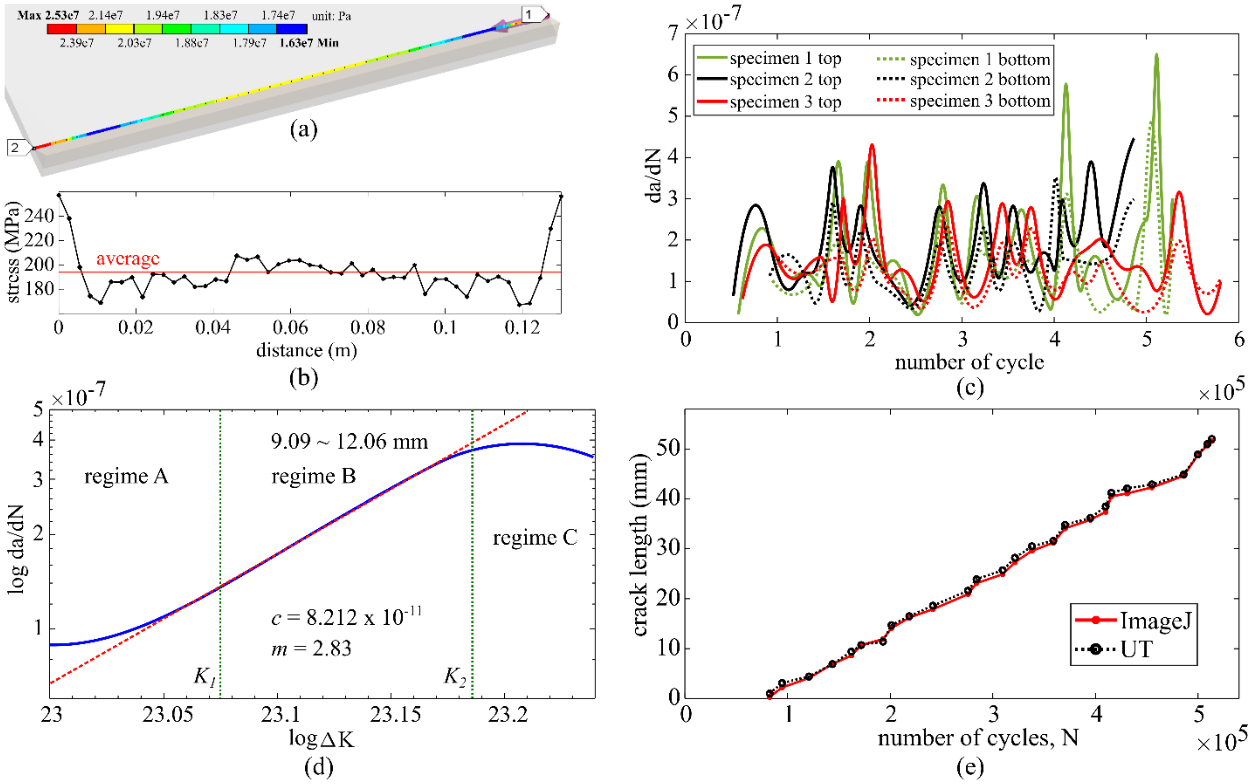

Figure 3.22. (a) Defined crack path along with the distribution of simulated bending stress along the path, (b) extracted bending stress values along the crack path, (c) crack growth rate (*da/dN*) as a function of loading cycles, (d) typical crack growth rate with respect to the stress intensity range in log scale, and (e) comparison of the visualized crack lengths with their results detected from UT

Experimental Procedure

The sensing properties of cSEC under angular rotation-induced bending strain were characterized on an HSS (i.e., no weld) specimen in Liu et al. (2021b). Here, the study is extended by creating the HSS by joining two L-shaped sections via a fillet weld. The fillet weld was selected in this study because it provides high shear strength and is typically applied to join two pieces of metal perpendicularly with small joint preparation required (Lu et al. 2015), and the test setup can be used to mimic a plate-to-web orthogonal weld connection. Four specimens were constructed (numbered 0 through 3), equipped with the cSEC, and tested under the previously developed fatigue load protocol. The objectives of the experiments were to characterize the capacitance response and evaluate the performance of the sensor at detecting and quantifying cracks on fillet welds. Figure 3.23a is an annotated photograph of the overall experimental configuration.

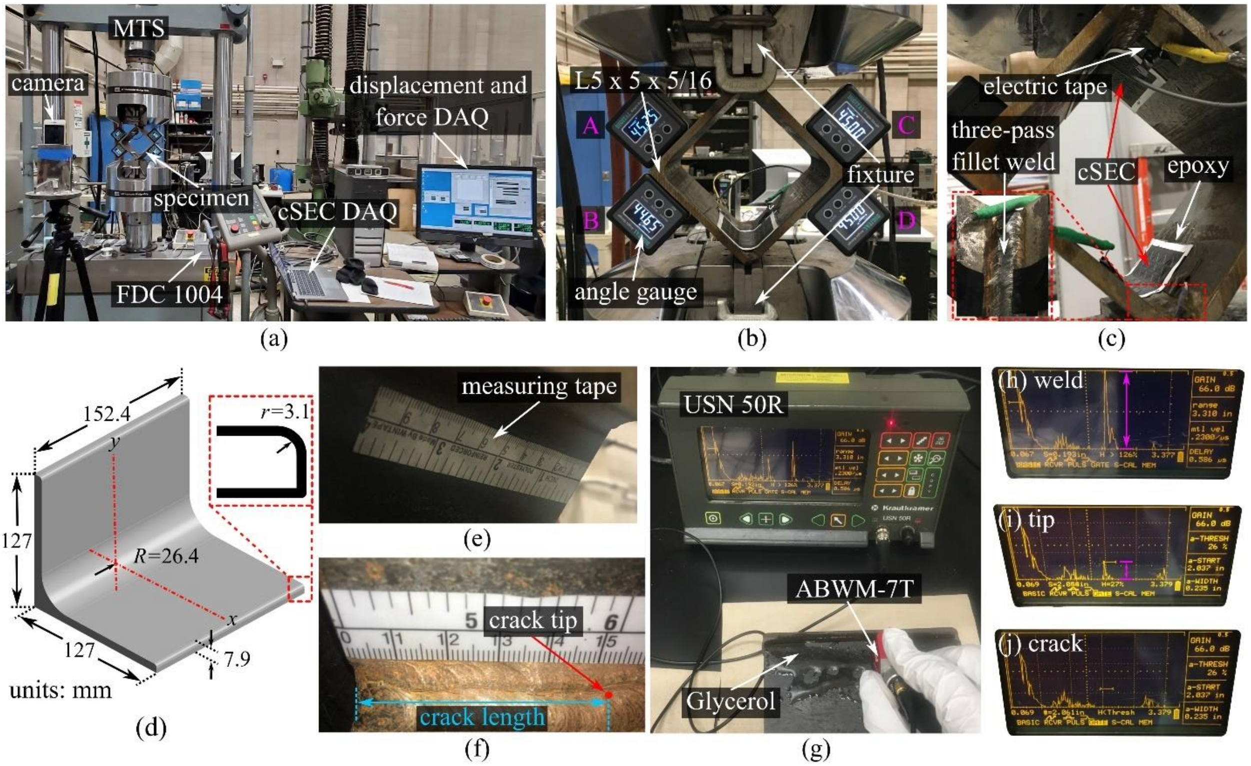

(a) (b) (c)

(d) (e) (f) (g)

Figure 3.23. (a) Overall experimental configuration (the arrow indicates the loading direction), (b) zoom on the front side of the welded specimen showing the digital angle gauges and custom H-shape fixture, (c) zoom on the back side of the welded specimen showing cSECs with the onset showing the detail of three-pass fillet weld, (d) geometric configuration of the L5 × 5 × 5/16 L-shaped channel, (e) measuring tape adhered next to the welded at the top corner of specimen 0, (f) picture of a fatigue crack propagated over 52.1 mm, (g) experimental setup for UT testing, and transmission pulse and defect echo under (h) weld, (i) crack tip, and (j) crack

Figure 3.23b is a close-up view of the front side of a welded specimen. It is fabricated using three-pass horizontal fillet welds along the edges of the two A36 L5 × 5 × 5/16 L-shaped channels. Values of $\varphi = 89.95^\circ$ and $\varphi = 90.05^\circ$, and $d = 11.3$ mm and $d = 11.2$ mm were measured at the corners in the top and bottom corners (Figure 3.22d). The inner surface of the welded specimen was sanded using 500 and 1000 grit sandpaper successively and rinsed with acetone to obtain a smooth and clean sensing area. As observable in Figure 3.23c, the off-the-shelf bicomponent epoxy (JB Weld) was applied as a thin layer onto the sanded surface of the fillet welds, and the cSECs were glued in folded configurations by adhering their flat surface onto the epoxy layer, with each cSEC aligned with an end of the weld and fully adhered onto the welded surface. Electrical tape was used to affix the wires to minimize signal noise caused by cable movement. Unlike specimens 1 through 3, specimen 0 only had one cSEC installed over the bottom corner. Specimen 0 was used exclusively to validate the ultrasonic testing (UT) procedure.

As shown in Figure 3.23e, a peel-and-stick measuring tape with 1 mm marks was adhered next to the crack path along the top corner of specimen 0 to assist with computer-aided visual measurement of the crack length during testing. Figure 3.23f is a photograph of a fatigue crack propagating over 52.1 mm on specimen 0, taken at cycle 50,293, with the crack tip indicated by a red dot. Two customized H-shaped fixtures fabricated using three AISI 1018 steel plates were placed over the upper and lower edges of the specimen and affixed onto the servo-hydraulic testing machine (MTS model 312.41 with a TestStar IIm controller) grips. To measure localized angular rotations along the top (θ_t) and bottom (θ_b) directions, four digital angle gauges, identified as A, B, C, and D in Figure 3.22b, were installed above and below the left and right corners. Those digital angle gauges have a minimum measurable degree resolution of 0.05° with a minimum reaction time of 0.1 seconds. These rotations correspond to the real angular rotation experienced by the installed cSEC sensors, with $\Delta\theta_t = |\Delta\theta_A| + |\Delta\theta_C|$ and $\Delta\theta_b = |\Delta\theta_B| + |\Delta\theta_D|$. The measurements from each angle gauge could also be obtained from the numerical model. They were assigned as negative for clockwise rotations and positive for counterclockwise rotations.

A preload of 0.05 kN was applied on the welded specimen prior to each test for a compression-compression mode. A loading frequency of 2 Hz was selected for initiating and propagating fatigue cracks. For simultaneously recording the rotated angular degrees, a digital camera with a frame rate of 30 fps was placed in front of the specimen to record the measurements from the angle gauges. Capacitance data collection was performed using a custom DAQ at a sampling frequency of 80 samples/second in the LabVIEW environment, and load and displacement data were recorded from the LVDT of the MTS at 20 samples s^{-1}. UT was performed using a Krautkramer Branson USN-50 R ultrasonic flaw detector equipped with an ABWM7 T-60 wedge probe to detect and quantify crack lengths under the sensor. The UT setup, shown in Figure 3.23g, used nontoxic glycerin with an acoustic impedance of 2.42 kg/m^{-12}s × 106 uniformly applied onto the exterior surface of the fillet welds to provide good contact and facilitate the transmission of sound waves. The ultrasonic flaw detector was set with a gain of 66 dB, displacement range of 84.07 mm (3.31 in.), sound velocity of 5,918,200 mm s^{-1} (0.233 in. μs^{-1}), and probe delay of 0.586 µs. The crack condition was identified by observing the transmission pulse and defect echo, where a significant amplitude, reduction in amplitude, and disappearance of amplitudes correspond to a weld, a crack tip, and a crack, respectively, as shown in Figures 3.23h–i.

Damage Model

Figure 3.24c plots the experimental S-N curves along with a linear interpolation to represent the crack propagation rates in terms of *da/dN* (increment of crack length per load cycle). Values for *da/dN* ranges from *da/dN* = 1.88×10^{-8} (m/cycle) to maximum *da/dN* = 6.49×10^{-7} (m/cycle) over the three specimens. These values are consistent with those reported in literature as typical in FCP (Pugno et al. 2006)

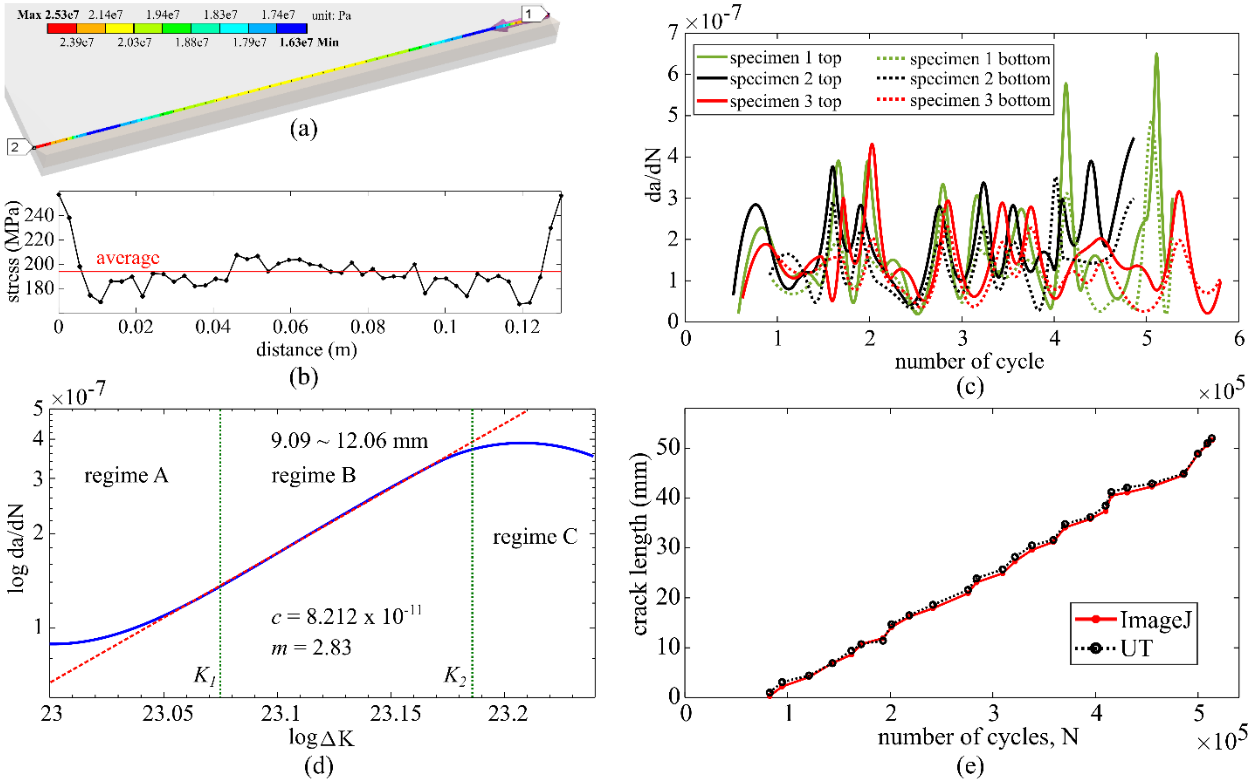

Figure 3.24. (a) Defined crack path along with the distribution of simulated bending stress along the path, (b) extracted bending stress values along the crack path, (c) crack growth rate (*da/dN*) as a function of loading cycles, (d) typical crack growth rate with respect to the stress intensity range in log scale, and (e) comparison of the visualized crack lengths with their results detected from UT

Figure 3.24c is a plot showing the variation in the fatigue crack length. It can be observed that the propagation rate varies with the fatigue load, implying a variability in the Paris' coefficients *C* and *m* over each crack growth interval. Figure 3.24d shows the crack growth rate (*da/dN*) as a function of stress intensity range (ΔK) in a log scale plot, where data are taken from the crack growth interval 9.09 to 12.06 mm on specimen 1. To quantify *C* and *m* in this selected interval, regime B was first identified on the curve by computing the threshold values of K_1 and K_2 following the threshold equation defined in Allen et al. (1988), represented by green dashed lines. After, a linear regression (red dashed line) was applied on regime B, and the Paris' coefficient *C* and exponent *m* were respectively taken as intercept on *y*-axis and determined as the slope of the fitted line (Allen et al. 1988).

The Paris' coefficients *C* and *m* throughout the test were characterized on each crack interval following the same procedure, and results are tabulated in Tables 3.5 and 3.6, where the superscripts b and t denote the bottom and top corner, respectively. The range is the resulting range of the coefficients found on each interval for specimen 1, and range* is the same range but over specimens 1 through 3. Overall, the ranges of both Paris' coefficients *C* and *m* found in those experimental tests are all in the valid ranges reported in Ritchie (1999) and Pugno et al. (2006).

Table 3.5. Experimentally obtained Paris' coefficients computed under different crack length intervals at the top (*t*) corners

Top crack length (mm)	0–2	2–4	…	48–50	Range	Range*
C_i^t	3.55×10^{-11}	4.63×10^{-11}	…	9.02×10^{-11}	2.801×10^{-11}–1.003×10^{-10}	2.66×10^{-11}–1.001×10^{-10}
m_i^t	2.68	2.72	…	2.70	2.64–2.71	2.65–2.76

Table 3.6. Experimentally obtained Paris' coefficients computed under different crack length intervals at the bottom (*b*) corners

Top crack length (mm)	0–3	3–6	…	78–81	Range	Range*
C_i^b	7.21×10^{-11}	1.12×10^{-10}	…	1.52×10^{-10}	6.708×10^{-11}–1.601×10^{-10}	6.13×10^{-11}–1.552×10^{-10}
m_i^b	2.83	2.81	…	2.85	2.69–2.85	2.68–2.88

Results and Discussion

Figure 3.25 plots the relative change in capacitance $\Delta C/C_0$ as a function of the MTS-derived strain (strain computed from MTS displacement) under crack lengths of 0, 9, 18, 27, 36, 45, 54, 63, and 72 mm.

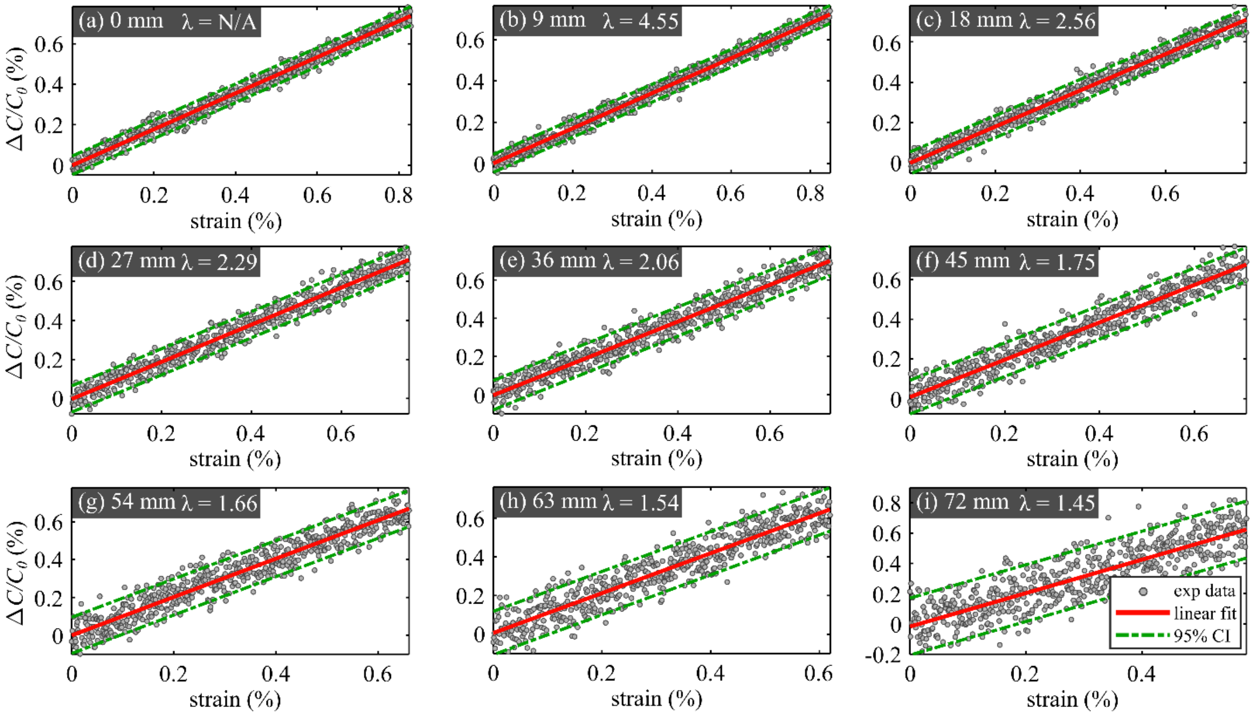

Figure 3.25. Three-specimen averaged relative change in capacitance (ΔC/C0) as a function of the MTS-derived strain under crack lengths of (a) 0 (undamaged), (b) 9, (c) 18, (d) 27, (e) 36, (f) 45, (g) 54, (h) 63, and (i) 72 mm

Values of the MTS-derived strain are extracted from the LVDT under the corresponding load and crack lengths, and the plots show the averaged measurements from specimens 1 through 3 installed at the bottom corners, along with a linear fit (red solid line) conducted within a 95% CI bound (dashed green lines). The gauge factors, corresponding to the slopes of the linear fits, are shown in each subplot.

Table 3.7 assembles the quantitative results under each crack length, also presented as the averaged values over specimens 1 through 3, showing the MTS-derived strain, the goodness of linear fit (R^2 value), the gauge factor (sensitivity) λ obtained from the localized crack strain (across-crack strain obtained using the FEM), accuracy (95% fit) in terms of $\Delta C/C_0$, equivalent strain resolution, and standard deviation of the measurements σ_{res}.

Table 3.7. Experimental results characterizing sensing performance

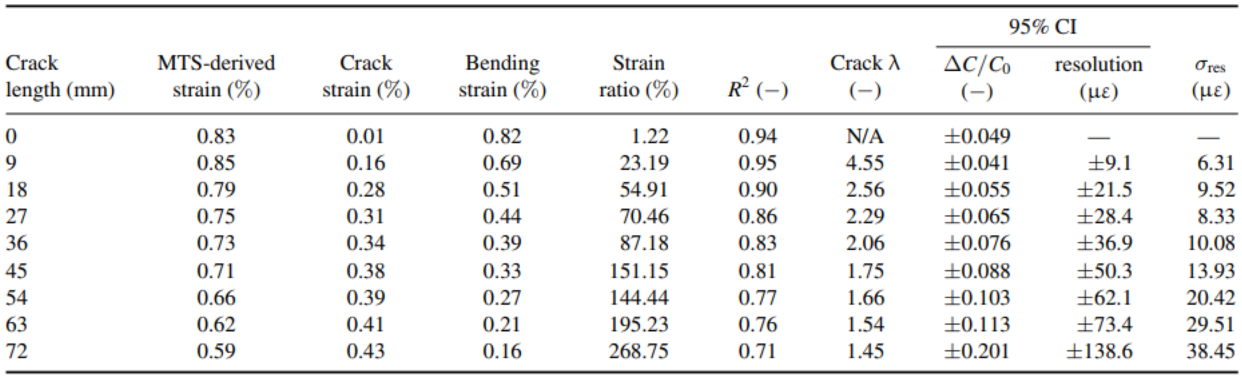

Crack length (mm)	MTS-derived strain (%)	Crack strain (%)	Bending strain (%)	Strain ratio (%)	R^2 (−)	Crack λ (−)	95% CI $\Delta C/C_0$ (−)	95% CI resolution (με)	σ_{res} (με)
0	0.83	0.01	0.82	1.22	0.94	N/A	±0.049	—	—
9	0.85	0.16	0.69	23.19	0.95	4.55	±0.041	±9.1	6.31
18	0.79	0.28	0.51	54.91	0.90	2.56	±0.055	±21.5	9.52
27	0.75	0.31	0.44	70.46	0.86	2.29	±0.065	±28.4	8.33
36	0.73	0.34	0.39	87.18	0.83	2.06	±0.076	±36.9	10.08
45	0.71	0.38	0.33	151.15	0.81	1.75	±0.088	±50.3	13.93
54	0.66	0.39	0.27	144.44	0.77	1.66	±0.103	±62.1	20.42
63	0.62	0.41	0.21	195.23	0.76	1.54	±0.113	±73.4	29.51
72	0.59	0.43	0.16	268.75	0.71	1.45	±0.201	±138.6	38.45

The equivalent strain resolutions are computed from $\Delta C/C_0$ and the gauge factor λ obtained from the crack strain. Results show that the MTS-derived strain and across-crack strain are respectively decreasing and increasing, resulting in the increase of the strain ratio (the percentage of strain attributable to the crack versus bending) as the crack propagates. The decreasing of the MTS-derived strain can be explained by the reduction of the fatigue loading under a longer crack length.

It can also be observed that the gauge factor decreases with the increase in crack length, attributable to the increase of the crack strain and strain ratio under a longer crack length. The gauge factor value under the 0 mm crack is discarded given the null level of crack strain. Overall, the cSECs exhibited good performance on linearity (R^2), resolution (95% CI), and accuracy (σ_{res}) under no crack (0 mm crack). As the crack forms and propagates, these metrics degrade, which can be attributed to the assumptions made in the electromechanical model yielding unmodeled kinematics and smaller SNR under smaller actuation levels (smaller MTS-derived strain). The observed decrease of SNR and crack detection sensitivity of LAE under smaller strain levels have been reported in other research (Kong et al. 2017a, 2017b).

Crack Growth Indices

This subsection is extracted from the following publications:

Liu, H., S. Laflamme, J. Li, C. Bennett, W. Collins, A. Downey, P. Ziehl, and H. Jo. 2021. Investigation of Surface Textured Sensing Skin for Fatigue Crack Localization and Quantification. *Smart Materials and Structures*, Vol. 30, No. 10.

Liu, H., S. Laflamme, J. Li, C. Bennett, W. N. Collins, D. J. Eisenmann, A. Downey, P. Ziehl, and H. Jo. 2022. Investigation of Textured Sensing Skin for Monitoring Fatigue Cracks on Fillet Welds. *Measurement Science and Technology*, Vol. 33, No. 8.

This section presents experimental crack growth index (CGI) data obtained from both cSECs and multifunctional soft stretchable strain sensors, specifically for monitoring in-plane fatigue cracks. Furthermore, the CGI data from cSECs are provided with a focus on monitoring fatigue cracks on fillet welds.

In-Plane Fatigue Crack Monitoring (C(T) Specimen)

cSEC

The quantification of a crack can be conducted using the CGI algorithm previously developed in Kong et al. (2016) that consists of a scalar relating to the size of the fatigue crack under or near a sensor. The principle of the CGI is to compare the magnitudes of the fundamental frequency peaks from the SEC signal and force input signal. The force input signal can be collected by other sensors indirectly relating to the input, such as an accelerometer measuring the vibration response of a beam subjected to such loads. Figure 3.26a compares the frequency spectrum of the SEC signal and MTS inputs (i.e., force input), where the input frequency of 2 Hz is clearly observable.

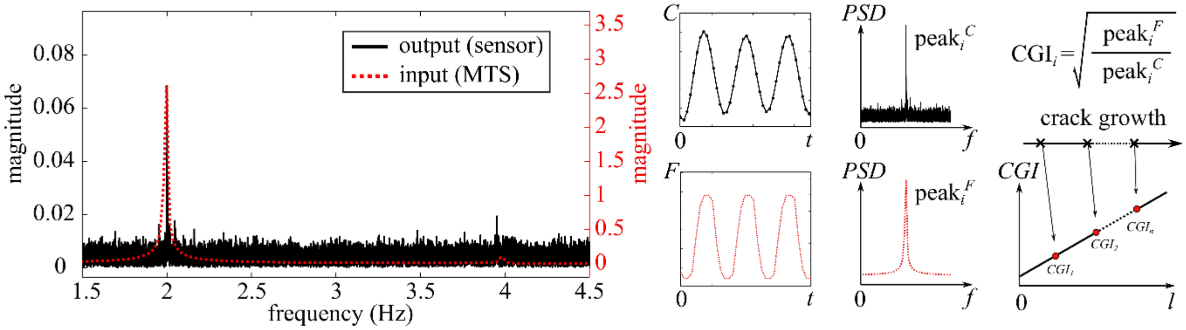

(a) (b)

Figure 3.26. (a) Frequency spectrum of an SEC with the reinforced diagrid pattern and (b) algorithm for the CGI

Mathematically, the CGI algorithm (Figure 3.26b) consists of extracting the peak PSDs from the short-term SEC measurements (C_i) and force measurements (F_i), yielding the peak magnitude of $\text{peak}_i^C$and of peak_i^F, respectively, with the CGI corresponding the to the square root of the ratio peak_i^F to peak_i^C. This process is implemented continuously over time, where it was found in Kong et al. (2016) that the CGI log scale relates linearly to the length l of high-cycle fatigue cracks. CGI data could be useful in SHM applications to directly quantify cracks and sound alarms or estimate crack growth rate by evaluating its temporal variations.

Here, the CGI algorithm was applied to the collected time series data. Figure 3.27a presents a plot of the computed CGI as a function of crack length for each pattern, with the *y*-axis presented on a log scale.

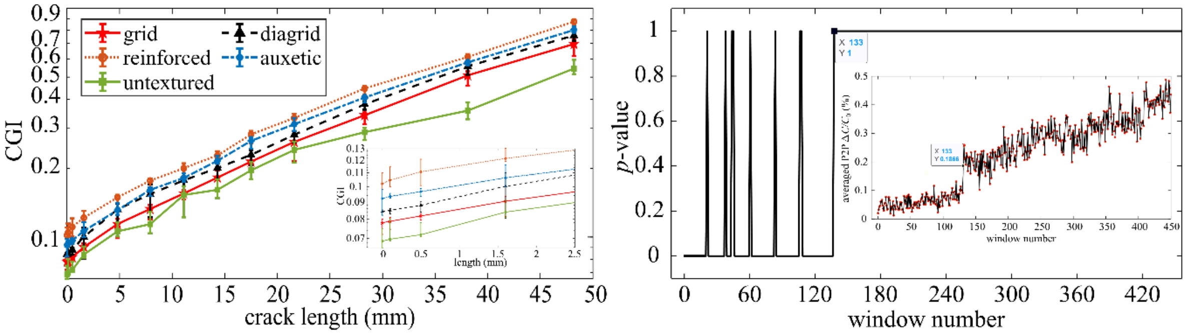

(a)

(b)

Figure 3.27. (a) Semi-log plot of CGI as a function of crack length under all patterns and (b) time series of averaged P2P ΔC/C0 amplitudes taken from each window

Results show the average values along with the CGI range through the error bar. The slight nonlinearity observed in the relationships between CGI and length may be explained by the propagation of low-cycle cracks. Regardless, the patterned SECs exhibited a net improvement in the CGI compared to the untextured SECs, showing far less variation in the CGI over a range of crack lengths.

The ability of a given sensor to discover a crack was determined by conducting a continuous paired t-test on the sensor's signal. To do so, the signal was split into windows of 10-second data sets. The 10th window (corresponding to the time interval 90 to 100 seconds) was taken as the reference window to eliminate early-stage noise in the signal. The P2P $\Delta C/C_0$ amplitudes were extracted, and the t-test was conducted under the null hypothesis that the mean of the P2P $\Delta C/C_0$ amplitudes from a new window was the same as that from the 10th window. Figure 3.27b presents the computed *p*-value for the first 4,500 seconds of the signal measured from an SEC (reinforced pattern), along with the time series of averaged P2P $\Delta C/C_0$ in the figure inset. A value of 1 indicates that the t-test rejects the null hypothesis at a 5% significance level. Here, a crack is discovered when the *p*-value remains stable at 1. In the example, that stability is reached for the 133th window, corresponding to 1,420 to 1,430 seconds. Chattering prior to that time could be attributed to measurement noise.

Table 3.8 lists the crack discovery times obtained for each sensor.

Table 3.8. Experimental results for the paired t-test

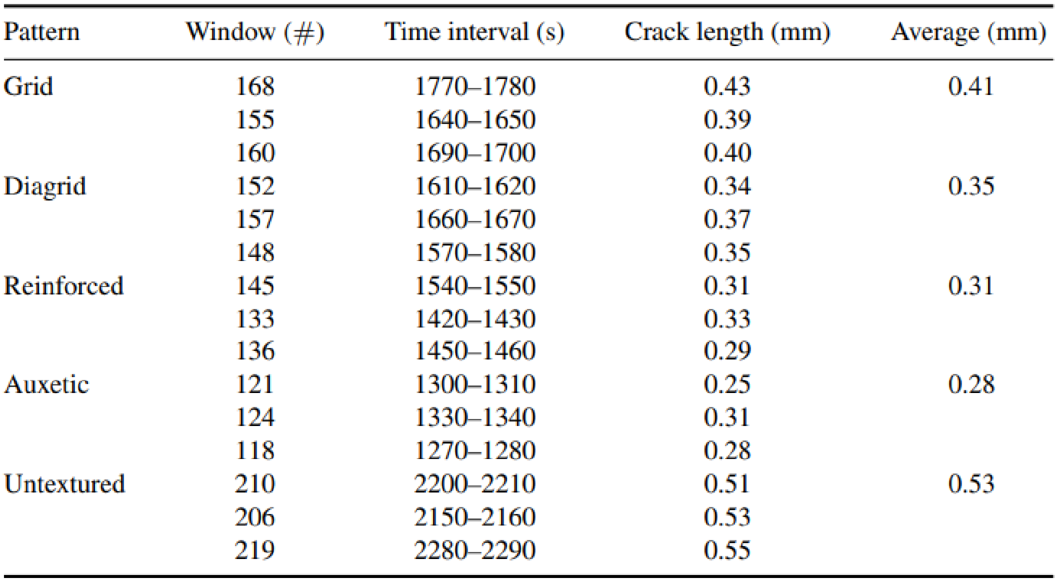

Pattern	Window (#)	Time interval (s)	Crack length (mm)	Average (mm)
Grid	168	1770–1780	0.43	0.41
	155	1640–1650	0.39	
	160	1690–1700	0.40	
Diagrid	152	1610–1620	0.34	0.35
	157	1660–1670	0.37	
	148	1570–1580	0.35	
Reinforced	145	1540–1550	0.31	0.31
	133	1420–1430	0.33	
	136	1450–1460	0.29	
Auxetic	121	1300–1310	0.25	0.28
	124	1330–1340	0.31	
	118	1270–1280	0.28	
Untextured	210	2200–2210	0.51	0.53
	206	2150–2160	0.53	
	219	2280–2290	0.55	

Results show that the auxetic and reinforced patterns significantly improved crack discovery capabilities (0.28 mm and 0.31 mm, respectively) compared to the untextured sensor (0.53 mm), corresponding to reductions in detectable crack length of 89% and 71%. The method used herein to detect a fatigue crack is inherently linked to the sensor’s resolution, whereas the t-test, in essence, determines when the signal produced by a crack raises above noise.

Multifunctional Soft Stretchable Strain Sensor

Figure 3.28a plots the computed CGI as a function of crack length in a semi-log scale plot, and linearity of the relationship was observed between 0 (no crack) and approximately 20 mm crack length. A continuous t-test on the sensor’s signal was used to determine the smallest detectable crack size from the signal. To do so, the CGI data were split into 25-second windows, and the 5th window (corresponding to the time interval 100 to 125 seconds) was taken as the reference window to reduce noise. Then, the t-test was conducted by using the t-test function in MATLAB and under the null hypothesis that the new CGI values were different from the CGI values in the reference window.

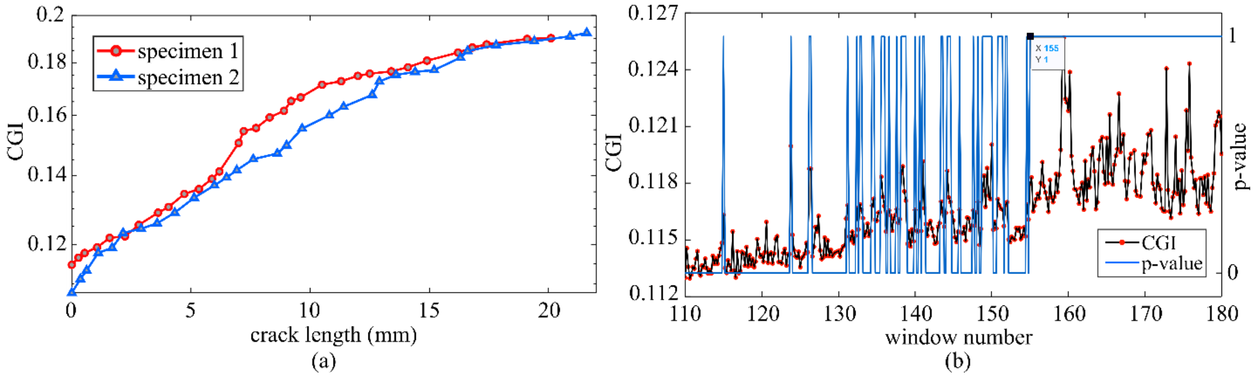

(a) (b)

Figure 3.28. (a) CGI as a function of crack length and (b) time series of averaged CGI values along with corresponding p-values from the t-test

Figure 3.28b is a time series plot of the resulting *p*-value. A *p*-value of 1 indicates that the t-test rejects the null hypothesis at a 5% significance level, and thus that a crack is discovered. In this study, the *p*-values from specimens 1 and 2 stabilized to 1 after the 155th and 148th windows, respectively. Those windows correspond to time intervals of 3,875 to 3,900 seconds and 3,700 to 3,725 seconds, indicating minimum detectable crack lengths of 0.86 and 0.82 mm, respectively.

Fatigue Crack on Fillet Welds

A real-time fatigue crack monitoring algorithm, diagrammed in Figure 3.29, was developed to produce actionable data from measurements.

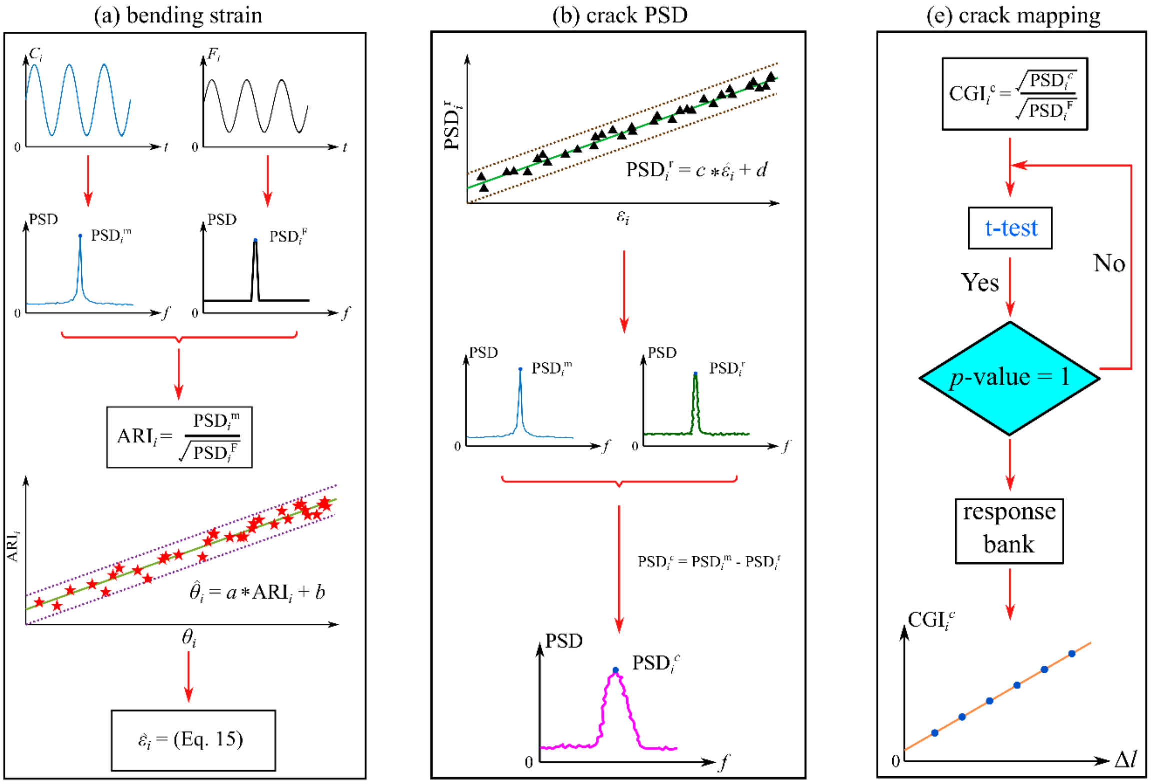

Figure 3.29. Schematic of the crack motoring algorithm framework

A challenge in the algorithm was to decouple strain produced by angular rotation and that produced by a crack. First, the capacitance C measurement of the cSEC and load input F measured indirectly by other sensors (e.g., bending strain on a girder produced by a moving car) were initially collected, with the capacitance filtered using a low-pass filter to reduce high-frequency noise and eliminate capacitance drift that is caused by environmental factors (i.e., temperature and humidity) and intrinsic electrical behavior associated with many sensors fabricated from hyper-elastic materials (Cai et al. 2013, Pasadas and Jiménez 2016). The PSD amplitudes of the cSEC (PSD_i^m) and load input sensor (PSD_i^F) were extracted and merged into an index termed ARI (Liu et al. 2021b) using the following:

$$ARI_i = \frac{PSD_i^m}{\sqrt{PSD_i^F}} \tag{35}$$

The ARI is a metric quantifying the level of angular rotation and relates linearly to the rotated angular degree with an accuracy of ±0.416°. The rotated angular degree (θ_i) was mapped from the ARI and converted to bending strain (ε_B) using equation 30. Based on work in (Liu et al. 2021b), there exists a linear relationship between the maximum amplitude of the PSD of the angular rotation (PSD_i^r) and ε_i, which allows the computation of PSD_i^r directly from the bending strain ε_B. After, the PSD amplitude of the crack-induced signal (PSD_i^c) can be computed by subtracting (PSD_i^r) from the measured PSD amplitudes (PSD_i^m). Another metric, termed CGI_i^c, is written as equation $\frac{\sqrt{PSD_i^c}}{\sqrt{PSD_i^F}}$ (Kong et al. 2019). Both ARI and CGI are metrics obtained by normalizing the numerators through taking the ratio to the square root of the peak force $\sqrt{PSD_i^F}$ to make their input independent and represent the level of the P2P capacitance amplitudes under a unit excitation load. However, the key difference is that the normalized numerators fuse different features, in which PSD_i^r and PSD_i^c are independently correlated with the level of the angular rotation and crack length at the *i*th measurement. A fatigue crack discovery can be determined by conducting a continuous paired t-test on CGI_i^c. The t-test would reject the null hypothesis and indicate a crack is discovered when the *p*-values are stabilized with a value of 1. Finally, the CGI_i^c data could be useful in SHM applications to directly quantify cracks and estimate the crack growth rate by evaluating its temporal variations, and the CGI_i^c based responses bank that includes user-defined thresholds under different crack lengths can be created for crack mapping.

The PSD amplitudes are extracted from the signals over different crack lengths, which represent the magnitude of the dominating frequency peak. Figure 3.30a plots the PSD$^{\mathrm{m}}$ amplitudes (from the cSEC signals) as the function of crack lengths.

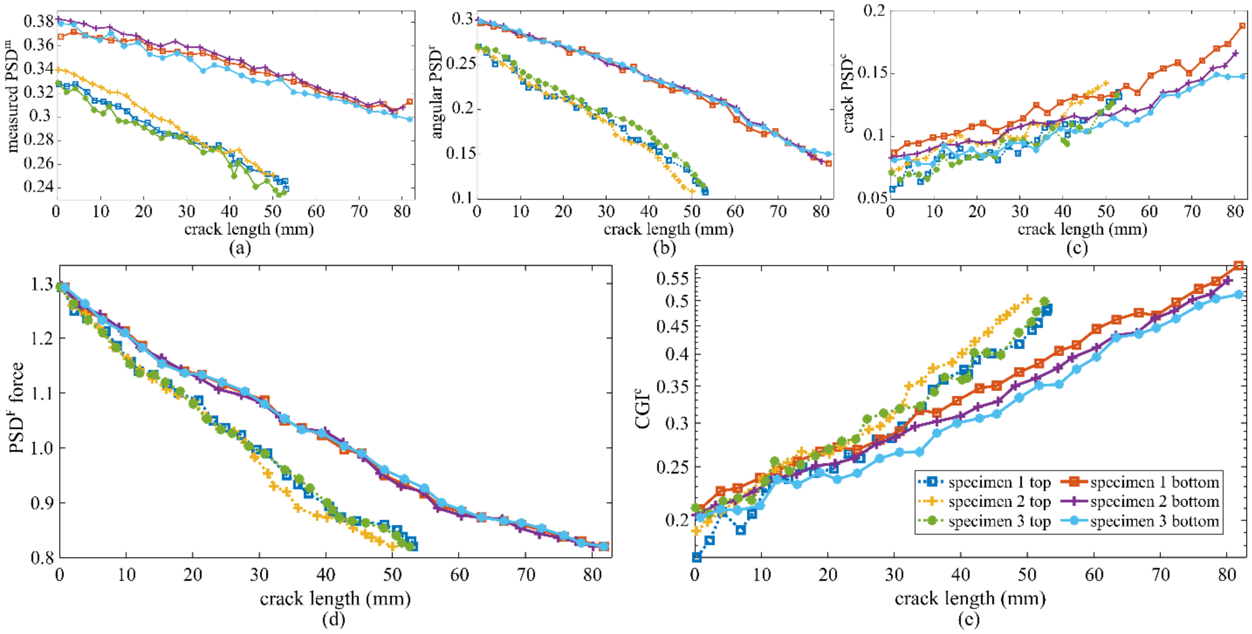

Figure 3.30. Signal study conducted in the top and bottom directions over three specimens: (a) measured, (b) angular rotation-induced, and (c) crack-induced P2P amplitudes of the relative change in capacitance $\Delta C/C_0$ as a function of crack lengths; (d) measured, (e) angular rotation-induced, and (f) crack-induced PSD amplitudes of measured time series data in capacitance response as a function of crack lengths; (g) PSD amplitudes of measured time series data in compression load under different crack lengths; and (h) semi-log plot of crack-induced CGI$^{\mathrm{c}}$ as a function of the crack length

One can observe that the $\mathrm{PSD}^{\mathrm{m}}$ amplitudes decrease with increasing crack length, attributable to the reduction in bending strain from the reduction in the compression load. To filter bending strain-induced capacitance response from the measured signal and eliminate the effect of the angular rotation, two linear regressions following findings in (Liu et al. 2021b) were used to identify the part of the signal caused by bending strain, which in turn can be used to identify angular rotation-induced amplitudes $\mathrm{PSD}^{\mathrm{r}}$ using equation 30. Results for the $\mathrm{PSD}^{\mathrm{r}}$ under each crack length are plotted in Figure 3.30b, also exhibiting an inverse relationship with crack length due to the reduction in the compression load. After, the crack-induced amplitudes $\mathrm{PSD}^{\mathrm{c}}$ are obtained by subtracting $\mathrm{PSD}^{\mathrm{r}}$ (Figure 3.30b) from $\mathrm{PSD}^{\mathrm{m}}$ (Figure 3.30a), and results are plotted in Figure 3.30c. It can be noticed that the $\mathrm{PSD}^{\mathrm{c}}$ are positive and approximately linear with respect to crack length, as desired. Lastly, the CGI is constructed using equation $\frac{\sqrt{PSD_i^c}}{\sqrt{PSD_i^F}}$.

Figure 3.30g plots the $\mathrm{PSD}^{\mathrm{F}}$ amplitudes of loading input under each crack length, and Figure 3.30h presents results in term of $\mathrm{CGI}^{\mathrm{c}}$ as a function of crack length in a semi-log scale plot, where the superscript c denotes crack-induced, where $\mathrm{PSD}^{\mathrm{c}}$ (Figure 3.30c) was used in the computation. A positive and approximately linear relationship between the CGI_i^c and the crack length was observed on the signal measured from all of the six installed cSECs, with the linear fit yielding R^2 values between 0.909 and 0.943. The produced values of the coefficient R^2 demonstrate high linearity and thus show considerable potential for using CGI_i^c as an actionable metric for fatigue crack mapping on fillet welds.

The signal was further processed using the proposed crack monitoring algorithm (in the previous Figure 3.29) to validate and verify the capability of a given sensor at discovering and quantifying fatigue cracks. The discovery of a fatigue crack was achieved by conducting a continuous paired t-test on and CGI_i^c. To do so, the time-series signal of both the capacitance and loading force signals were split into numerous windows with each window covering a 100-second data set, and each 100-second data set was further split evenly into 10 10-second data sets, named as a subset. The data in each subset were extracted and converted to the frequency domain to obtain CGI_i^c amplitudes.

Thus, 10 values of the CGI_i^c were included in each 100-second window. To eliminate early-stage chattering in the signal, data in the first two windows were discarded, and the third window (time interval 201 to 300 seconds) was taken as the reference window. A continuous paired t-test was conducted on the CGI_i^c by using the t-test function in MATLAB, and the test is under the null hypothesis that the mean of the 10 CGI_i^c values in a new window is the same as those in the reference window.

Figure 3.31a presents the averaged value of CGI_i^c in each window in the form of a time series, obtained from the bottom corner of specimen 1, and Figure 3.31b presents the resulting *p*-values computed from each window. It can be observed that the *p*-values stabilized to 1 after the 382nd window, which indicates that the t-test rejects the null hypothesis with a 5% significance level, and therefore that a crack is detected.

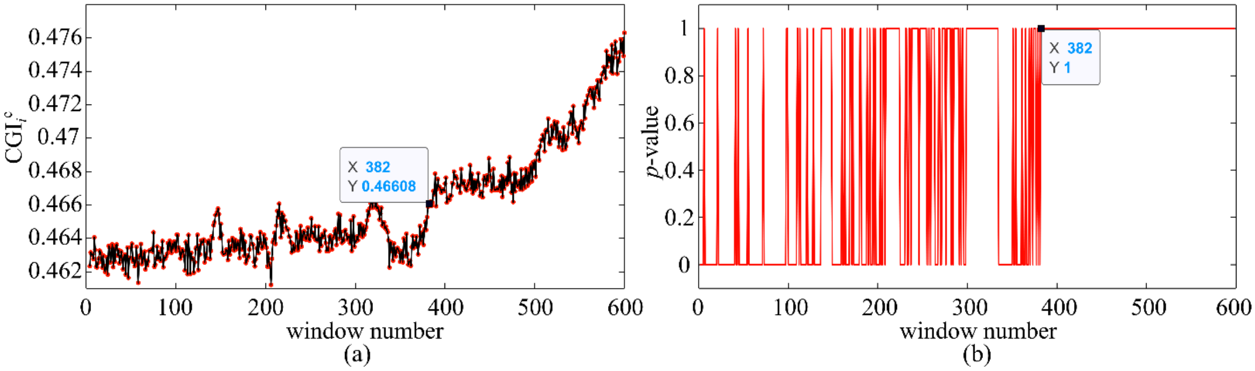

Figure 3.31. (a) Time series of averaged CGI$_i^c$ values taken from each window and (b) the computed *p*-value for the first 60,000 seconds of the signal

Table 3.9 lists and compares results for the CGI$_i^c$ in terms of the detected number of windows, corresponding time interval, corresponding number of cycles, and resulting crack lengths found by applying the crack monitoring algorithm to the signal taken from each sensor installed over the specimens 1 through 3.

Table 3.9. Experimental results obtained from the crack monitoring algorithm

		Top corner				Bottom corner			
	Sample	Window (#)	Time interval (s)	Cycle (#)	Crack length (mm)	Window (#)	Time interval (s)	Cycle (#)	Crack length (mm)
CGI	1	515	51 800–51 900	103 600–103 800	0.48	382	38 500–38 600	77 000–77 200	0.59
	2	530	53 300–53 400	106 600–106 800	0.50	361	36 400–36 500	72 600–72 700	0.52
	3	518	52 100–52 200	104 200–104 400	0.49	390	39 300–39 400	78 600–78 800	0.61

The crack lengths were obtained from the validated numerical model by inputting the number of cycles. It can be observed that the minimum detectable crack length ranges from 0.48 to 0.61 mm, which are slightly longer than the 0.31 mm reported in prior work on the cSEC for when detecting fatigue cracks over the flat surface of a C(T) specimen, attributable to the more complex geometry under consideration.

Conclusion

This chapter focused on the laboratory characterization of the sensing skin technologies we developed in this project. We investigated enhanced sensing performance provided by the textured SEC using various corrugation patterns and validated the capability of using cSEC and multifunctional soft stretchable strain sensors for detecting and quantifying mode-I fatigue cracks on steel. The general sensing performance of both the cSEC and the multifunctional strain sensor in terms of linearity, sensitivity, resolution, and accuracy were characterized and evaluated. We also leveraged the high compliance of the cSEC to measure angular motion in steel components by deploying the sensor in a folded configuration, deriving an extended electromechanical model adapted for angular motion sensing, and formulating a four-step algorithm to assess and quantify the angle of rotations.

Building on these findings, a three-pass horizontal fillet weld was selected and applied on the edge of two steel angles for welded corners and to mimic behavior at plate-to-web orthogonal connections in steel bridges. The cSEC sensors were fully adhered to the surface of the fillet welds and subjected to angular rotation-induced bending deformation under compression force. A newly proposed CGI_i^c metric was developed to transform the sensor data into actionable information, allowing for an accurate quantification of the crack length on fillet welds.

It was also found that adding a texture resulted in an overall 69% to 100% increase in gauge factor, 35% to 113% increase in linearity, 222% to 319% increase in the resolution, and 111% to 582% increase in stability compared to untextured SECs. The multifunctional soft stretchable strain sensor exhibited distinct color changes at the location of the crack opening and yielding an average minimum detectable crack length of 0.84 mm. ARI mapped linearly to the angle of rotation, with an accuracy of 0.416° that compares well with off-the-shelf tiltmeters. The proposed algorithm demonstrated promise at crack quantification through t-tests conducted on the CGI_i^c, resulting in a minimum detectable crack length of 0.48 mm on fillet welds.

CHAPTER 4: DEVELOPMENT OF THE WIRELESS CAPACITIVE SENSING BOARD

This chapter is extracted from the following publication:

Jeong, J.-H., H. Jo, S. Laflamme, J. Li, A. Downey, C. Bennett, W. Collins, S. A. Taher, H. Liu, and H.-J. Jung. 2022. Automatic Control of AC Bridge-Based Capacitive Strain Sensor Interface for Wireless Structural Health Monitoring. *Measurement*, Vol. 202.

Overview

This chapter discusses the development of the wireless capacitive sensing board that integrates the cSEC with the sensing platform for wireless sensing of fatigue cracks on steel bridges. We address the limitations of precise AC bridge balancing, signal amplification control, and shunt calibration associated with the AC bridge-based signal converter through critical updates in both hardware and software, incorporating fully automated features for high-sensitive capacitive strain sensing. The newly developed sensing board was designed to interface with the Xnode wireless platform utilizing its power supply (3.3 V), analog-to-digital conversion (ADC), onboard signal processing, and wireless data communication capabilities. Prototype sensor boards were fabricated, and their performance for capacitive strain sensing validated through a series of laboratory tests and compared with an off-the-shelf wired capacitance measurement system.

AC Wheatstone Bridge-Based Capacitive Strain Sensor Board

WSS are an attractive solution for SHM in that they enable wireless communication among sensor nodes distributed over large-scale structural systems without costly cabling (Spencer et al. 2017). Various sensing hardware and software systems have been developed for accelerometer and resistive strain gauge sensing and validated over full-scale implementations (Jang et al. 2010, Jo et al. 2013). However, capacitance-based strain sensing methods have not benefited from these advantages of WSS networks for SHM.

A recent research project has developed an analog De-Sauty bridge-based wireless capacitive strain sensor board (c-strain sensor board) that demonstrated extremely low-level capacitive strain sensing capability in a wireless manner (Jeong et al. 2018a, 2018b). It was successfully integrated with the high-fidelity smart sensing platform Xnode that provides various functionalities for high-sensitivity wireless SHM; Xnode functions include a solar-powered battery, low power consumption, 3.3 V power supply, onboard signal processing, wireless communication, and 24-bit ADC. The static and dynamic strain sensing sensitivity of the developed c-strain sensor board was validated via a series of laboratory tests. However, several practical limitations remain to be resolved for large-scale field implementation. The c-strain sensor board comprises full analog circuits; AC bridge balancing, amplification, and a two-step shunt calibration process are required to be done manually with an oscilloscope for high-frequency AC signal control prior to actual deployment for sensing to ensure high-quality measurement. However, such manual setup with the oscilloscope is cumbersome and is challenging in field conditions. Also, field engineers should have background knowledge of the sensor board pre-setup, such as precise AC bridge balancing and shunt calibration procedures, which is not desirable. Some studies have developed automated AC bridge balancing techniques for easy capacitance sensing applications (Holmberg 1995, Mantenuto et al. 2014). However, none of these approaches deals with the automated amplification and shunt calibration required for wireless SHM applications.

This study presents the development of a fully automated c-strain sensor board for wireless SHM applications, which can interface with the Xnode wireless sensor platform to be used under its 3.3 V power for a measurement range of 0 to 2.4 V. While keeping the basic capacitance measurement framework of the analog c-strain sensor board, we developed a low-cost microcontroller-based automated AC bridge balancing, amplification, and shunt calibration method. Peak-detection circuits and a 16-bit ADC were employed to read the peak voltages of the high-frequency AC signals. Digital potentiometers (DPs), a digital bus switch, and an 8-bit microcontroller were employed to control the AC bridge balancing, signal amplification, and two-step shunt calibration. Embedded software was developed for automated control of the digital components. A prototype of the new sensor board was produced, and the performance was validated via laboratory tests and compared with a commercial wired capacitance measurement system.

Fully Automated Capacitive Strain Sensor Board Design

The research objectives included measuring low-level structural strains using the SEC by converting the capacitance variation of the SEC into an analog voltage signal in a fully automated manner. We designed the new sensor board with the following requirements: (1) integration with the existing WSS platform Xnode, (2) high-sensitivity capacitive strain sensing, and (3) fully automated bridge balancing, amplification, and shunt calibration. Figure 4.1 shows the block diagram for the new sensor board, which illustrates the fully automated capacitance sensing procedure interfacing with the Xnode platform.

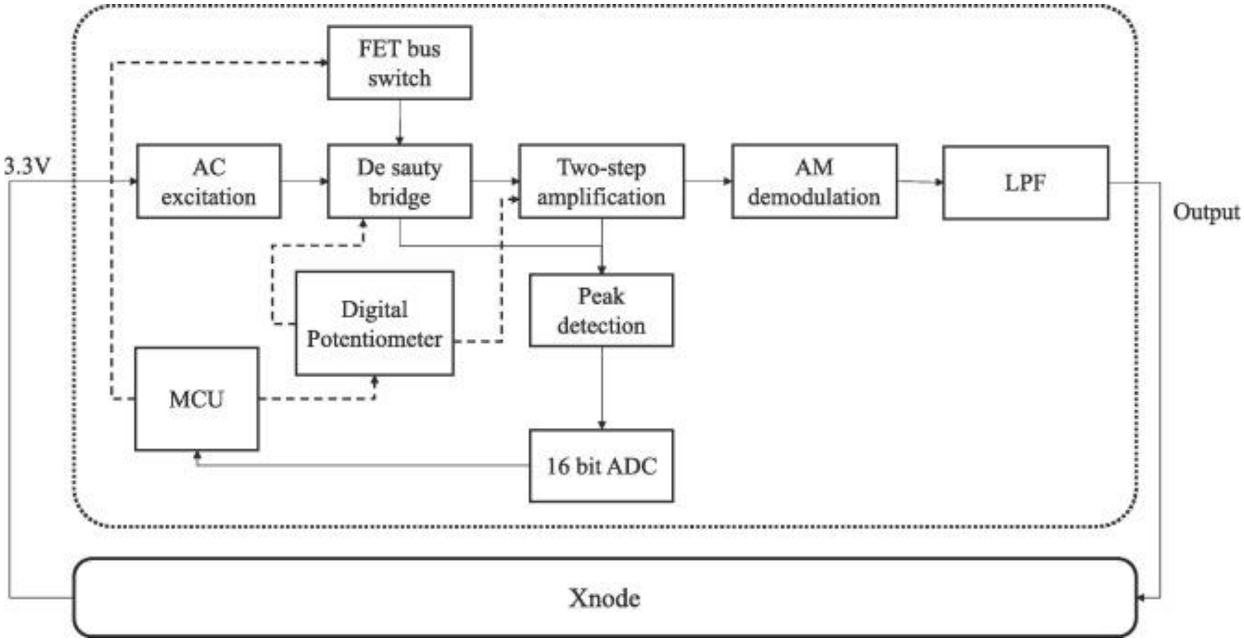

Figure 4.1. Block diagram for capacitive sensing module

The basic signal processing followed the AC bridge-based analog capacitance sensing system developed by Jeong et al. (2018b) that consists of AC signal excitation, AC De-Sauty bridge balancing, two-step amplification, amplitude modulation (AM) demodulation, and two-step shunt calibration. The full analog sensor board required manual adjustment and tuning (Jeong et al. 2018b). In contrast, the new sensor board employs digitally controlled parts and their associated circuits, microcontroller unit (MCU), and embedded software for fully automated operations. Analog potentiometers and a manual switch were replaced by a DP and a field-effect transistor (FET) bus switch controlled by the MCU. Direct control of the high-frequency AC signal by the MCU is not desired for wireless sensing systems due to its intensive computational requirements. To this end, an alternative AC signal control method was developed using a peak-detection circuit and a newly developed algorithm.

Wireless Sensing Platform

The new sensor board was developed to interface with a commercial wireless smart sensing platform Xnode, which provides the most advanced hardware and software features for wireless SHM applications available on the current market, enabling wireless capacitive strain sensing. The Xnode has a powerful dual-core central processing unit (CPU) (ARM cortex M0/M4), 24-bit ADC (ADS131E8), low-power wireless radio transceiver (Atmel AT 86RF233), Secure Digital (SD) data storage, triaxial accelerometer, three-channel strain Wheatstone bridge, five additional analog voltage input channels, and 4G LTE module (Sierra Wireless HL7588 LTE-CAT4) for data transfer to cloud storage. The Xnode uses a software framework based on the Illinois Structural Health Monitoring Project (ISHMP) services Toolshuite, providing various functionality for robust wireless SHM applications (Spencer et al. 2017). The Xnode has demonstrated its performance via various full-scale SHM projects (Fu et al. 2019, Hoang et al. 2020).

Particularly, the sensor board hardware is designed to be compatible with the Xnode hardware system. All parts and circuits were selected and designed to be powered by the Xnode's regulated 3.3 V voltage supply, and the sensor board output was adjusted to meet the measurement range (i.e., 0 to 2.4 V) of the Xnode's 24-bit ADC after onboard signal conditioning. Figure. 4.2 shows a schematic of the new sensor board and Xnode interface configuration.

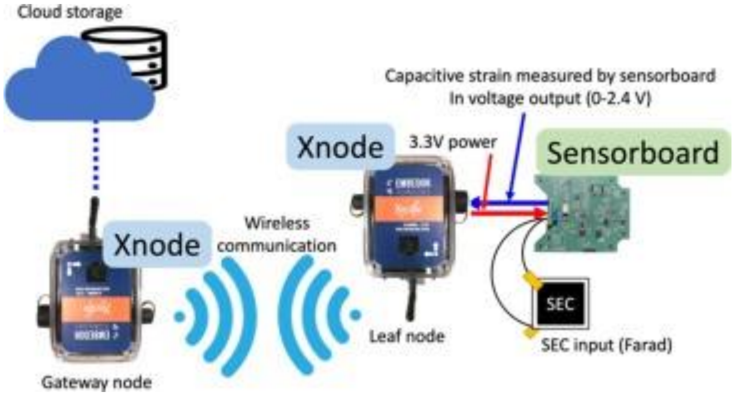

Figure 4.2. Sensor board and Xnode interface configuration

As shown in Figure 4.2, the Xnode has two types of nodes in the network. The leaf node measures the structural response data from the target structures and transmits data to the gateway node. The gateway node manages the whole sensor network by scheduling and triggering the network operation, collecting the measurement data from leaf nodes, and transmitting the collected data to cloud storage. The Figure 4.2 configuration has been successfully demonstrated in field conditions in (Anwar et al. 2022), and the new sensor board was also designed in the same compliance with the former system (Jeong et al. 2018b).

The AC De-Sauty bridge balancing and the two-step signal amplification are the two major parts for high-sensitivity capacitive strain sensing developed in this study. The bridge balancing should be designed precisely, and proper amplification is required to ensure the maximum sensitivity without saturation. The high-frequency AC signal (Vin, OSC) was excited using a 32.768 kHz square wave oscillator and converted to sine wave using a fourth-order Sallen-Key filter. The AC bridge with two resistors and two capacitors known as the De-Sauty bridge was used. It requires two potentiometers for bridge balancing and a dual-step amplification stage for gain control. There are various kinds of automated De-Sauty bridge balancing techniques that have been developed utilizing voltage-controlled resistor (VCR) and feedback loop circuits (Mantenuto et al. 2014). We employed a four-channel non-volatile DP (AD5254 with 256-tabs 100 kΩ 4 CH, Analog Devices) to directly control the bridge balancing and amplification via a microcontroller. Figure 4.3 shows the detailed schematic diagram of the De-Sauty bridge, amplifiers, peak detection circuit, 16-bit ADC, and MCU. The DP directly adjusts four resistances (R1 4) for bridge balancing and amplifications.

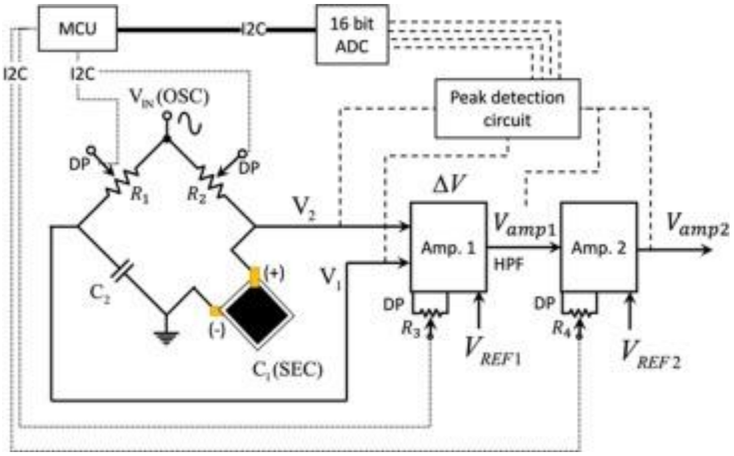

Figure 4.3. Fully automated De-Sauty bridge and two-step amplification design

The balanced bridge configuration status is obtained when $R_2/R_1 = C_1/C_2$. C_1 is the nominal capacitance of the SEC (DUT, device under test) and C_2 is the reference capacitor. Two AC signals from the De-Sauty bridge and two AC signals from the two-step amplifiers (AD8226, Analog Devices), for a total of four AC signals, were fed to the peak detection circuit shown in Figure 4.4, which detects AC peak voltages.

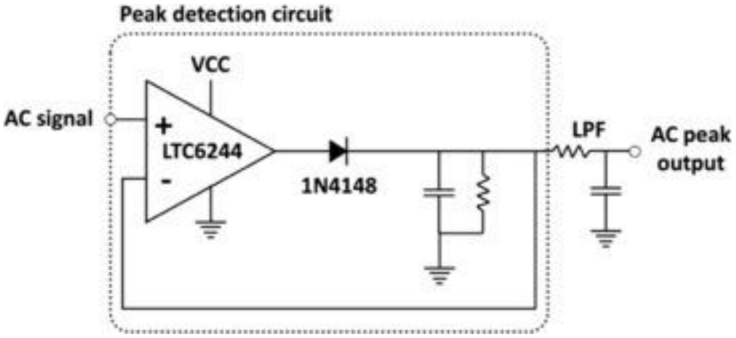

Figure 4.4. Peak detection circuit

A total of four peak detection circuits were employed to detect AC peaks separately, targeting the 0 to 40 Hz frequency bandwidth. The four signals were fed into a 16-bit ADC (ADS1115, Texas Instruments) for precise peak voltage detection from the MCU with 0.1 mV resolution (i.e., ADS1115 has 15-bit effective resolution). Figure 4.5 shows an example of a peak detection output where the peak of the AC signal was precisely detected.

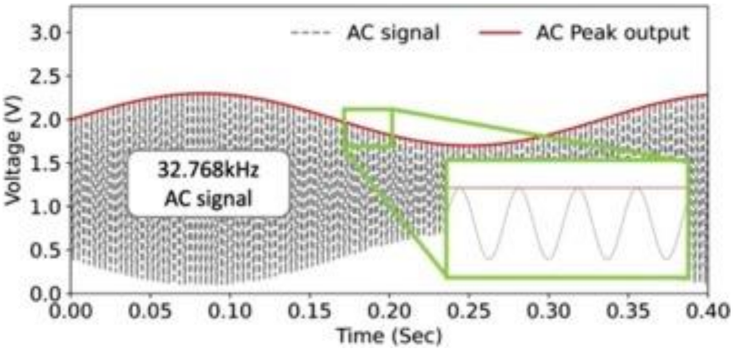

Figure 4.5. Peak detection result

The peak signals were fed to the ADC for precise voltage monitoring. Software was developed for automated bridge balancing and amplification.

The voltage difference from the De-Sauty bridge (i.e., $V_1 - V_2$), which was induced by the variation of SEC capacitance $C_1' = C_1 + \Delta C$, can be expressed as follows:

$$V_{test} = V_2 - V_1 = V_{in}\left(\frac{\frac{1}{j\omega C_2}}{R_2+\frac{1}{j\omega C_2}} - \frac{\frac{1}{j\omega(C_1+\Delta C)}}{R_1+\frac{1}{j\omega(C_1+\Delta C)}}\right) \tag{36}$$

Equation 36 can be rearranged to the following equation:

$$V_{test} = V_{in}\left(\frac{j\omega(C_1R_1-C_2R_2)+j\omega\Delta CR_1}{(1+j\omega C_1R_1+j\omega\Delta CR_1)(1+j\omega\Delta C_2R_2)}\right) \tag{37}$$

Equation 37 can be simplified by neglecting ΔC in the denominator, since the capacitance variation is very small compared to the nominal capacitances (i.e., C_1 and C_2) of the SEC and reference capacitor, and $C_1R_1 - C_2R_2$is zero in the numerator when the bridge is balanced. Therefore, equation 37 can be approximated by the linear expression given in the following equation:

$$V_{test} = V_2 - V_1 = V_{in}\left(\frac{j\omega R_1}{(1+j\omega C_1R_1)(1+j\omega C_2R_2)}\right)\Delta C \tag{38}$$

The maximized amplification is essential for high-sensitivity capacitive strain sensing. The voltage variation V_{test} by ΔC is amplified in the amplification stage. However, perfect balancing cannot be achieved in practice due to the parasitic capacitance, which leads the direct current (DC) components in V_{test}. Therefore, a two-step amplification was employed with a high-pass filter between two amplification stages to maximize the sensitivity, expressed as follows:

$$V_{output} = G_2\{(G1 \cdot V_{test} + V_{REF1}) - V_{HPF}\} + V_{REF2} \tag{39}$$

The DP directly controls the gains for each amplification stage, and DC voltages are supplied via V_{REF1} and V_{REF2} to prevent saturation and control the output level.

The amplitude of the amplified signal V_{output} represents the capacitance change ΔC. The AM demodulation circuit was employed to take the amplitude envelope targeting the frequency bandwidth of 0 to 30 Hz based on the following equation 40:

$$f \ll \tau = RC \ll \frac{1}{\omega} \tag{40}$$

where f is the carrier frequency, τ is the RC circuit charging time, and ω is the message bandwidth. The enveloped signal is passed through a second-order active low-pass filter (LPF) to clean the voltage output.

Two-Step Shunt Calibration Circuit

Shunt calibration is a key step to convert the voltage output to the desired unit for Wheatstone bridge-based sensing applications. Particularly in this application, the capacitance is affected by the parasitic capacitance (Z_L) in the lead wires that connect the SEC and AC De-Sauty bridge, as shown in Figure 4.6, of which the parasitic capacitance effect needs to be effectively considered for accurate calibration.

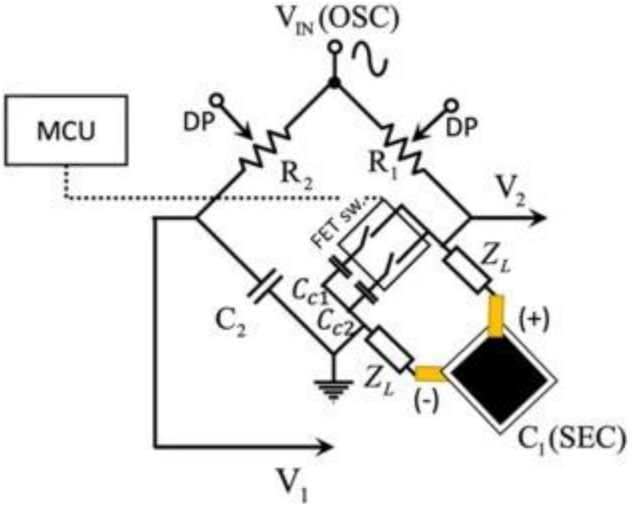

Figure 4.6. Two-step shunt calibration diagram

A recent study introduced the two-step shunt calibration strategy to avoid the parasitic capacitance effect (Jeong et al. 2018b). In this study, an FET bus switch (SN74CBT, Texas Instruments), which can handle multiple switch channels, was employed for the automated two-step shunt calibration procedure. The majority of digitally controllable switches, such as a bipolar junction transistor (BJT) and electromechanical relay, have a substantial parasitic capacitance, which is not negligible for this high sensitivity measurement application. Indeed, each component has its own unknown parasitic capacitance, which may result in inaccurate shunt calibration, particularly when a serial connection effect with the shunt capacitor is expected. The multichannel FET bus switch, selected for this application, has a low internal capacitance that is not prone to such an unknown parasitic capacitance effect.

The voltage-unit sensor board output (i.e., ΔV) can be converted into capacitance unit (i.e., ΔC) by the following equation:

$$\Delta C = \left(\frac{C_{C1} - C_{C2}}{V_{C_{C1}} - V_{C_{C2}}}\right)\Delta V \tag{41}$$

where C_{C1} and C_{C2} are shunt capacitors with different capacitance values, $V_{C_{c1}}$and $V_{C_{c2}}$ are the voltage levels measured from the two shunt calibration steps, respectively. The shunt calibration factor, which is the coefficient expression in equation 41, can be obtained by dividing the shunt capacitors' value difference (i.e., $C_{C1} - C_{C2}$) by the measured voltage difference (i.e., $V_{C_{c1}} - V_{C_{c2}}$) between each shunt steps.

The accuracy of the two-step shunt calibration using the FET bus switch was validated. The two capacitors were connected to the FET bus switch via parallel connection with an SEC having 870 pF nominal capacitance. The FET bus switch was controlled by a microcontroller (ATmega328P). The capacitance was measured using an off-the-shelf capacitance measurement toolkit PCAP02 for a reference evaluation.

Figure 4.7 shows the example test results of two cases using two pairs of shunt capacitors (i.e., 10 pF and 30 pF capacitors for case 1 and 10 pF and 47 pF capacitors for case 2) to demonstrate why two-step shunt calibration is required for the De-Sauty bridge-based capacitance sensing and validate whether the selected FET switch works as expected.

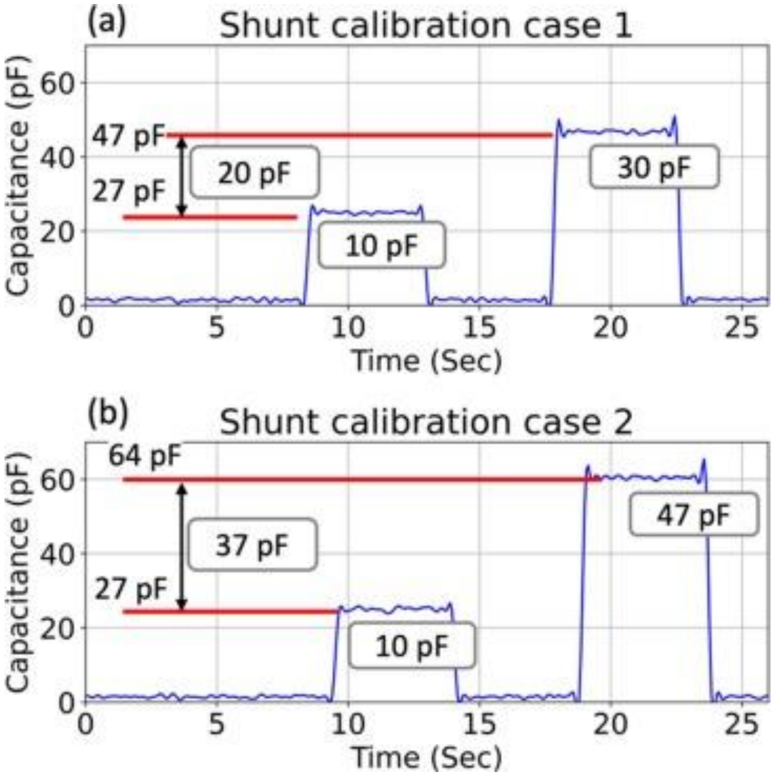

Figure 4.7. FET switch bus validation for the proposed two-step shunt calibration (two example cases for demonstration)

For example, when the first 10 pF shunt capacitor was connected (i.e., 10 pF on and 30 pF off) to the SEC bridge arm in parallel in case 1, a 27 pF capacitance increment was observed as shown in Figure 4.7a, while a 10 pF increment was expected. This implies that an unexpected additional 17 pF parasitic capacitance, which is the difference between the 27 pF observation and 10 pF shunt capacitor, exists in the bridge circuit and lead wires. Similarly, when the second 30 pF shunt capacitor was connected in case 1 (i.e., 10 pF off, and 30 pF on), a 47 pF increment was observed, which still includes the 17 pF parasitic capacitance (i.e., 47 pF – 30 pF = 17 pF). However, the capacitance difference between the two shunt capacitors (i.e., 30 pF – 10 pF = 20 pF) exactly matched with the measurement difference (i.e., 47 pF – 27 pF = 20 pF), implying that two-step shunt calibration process is required to get rid of the parasitic capacitance hidden in the bridge circuit and lead wires. Case 2, using a different pair of shunt capacitors, also showed the same trend results as shown in Figure 4.7b. When 10 pF and 47 pF shunt capacitors were used, the capacitance difference of 37 pF (i.e., 47 pF – 10 pF = 37 pF) exactly matched with the measurement difference (i.e., 64 pF – 27 pF = 47 pF), validating that the selected FET switch worked as expected with good accuracy for the two-step shunt calibration.

Software Development

In addition to the hardware improvement, a new software framework was developed to implement the fully automated bridge balancing, signal amplification, and shunt calibration. The ATmega328P-AU (microchip) was used as an MCU. While the original clock speed is 16 MHz under a 5 V supply, the ATmega328P-AU was downclocked to 8 MHz to work under a 3.3 V supply with lower power consumption.

Figure 4.8 shows the flowchart of the fully automated De-Sauty bridge balancing, amplification, and shunt calibration procedures.

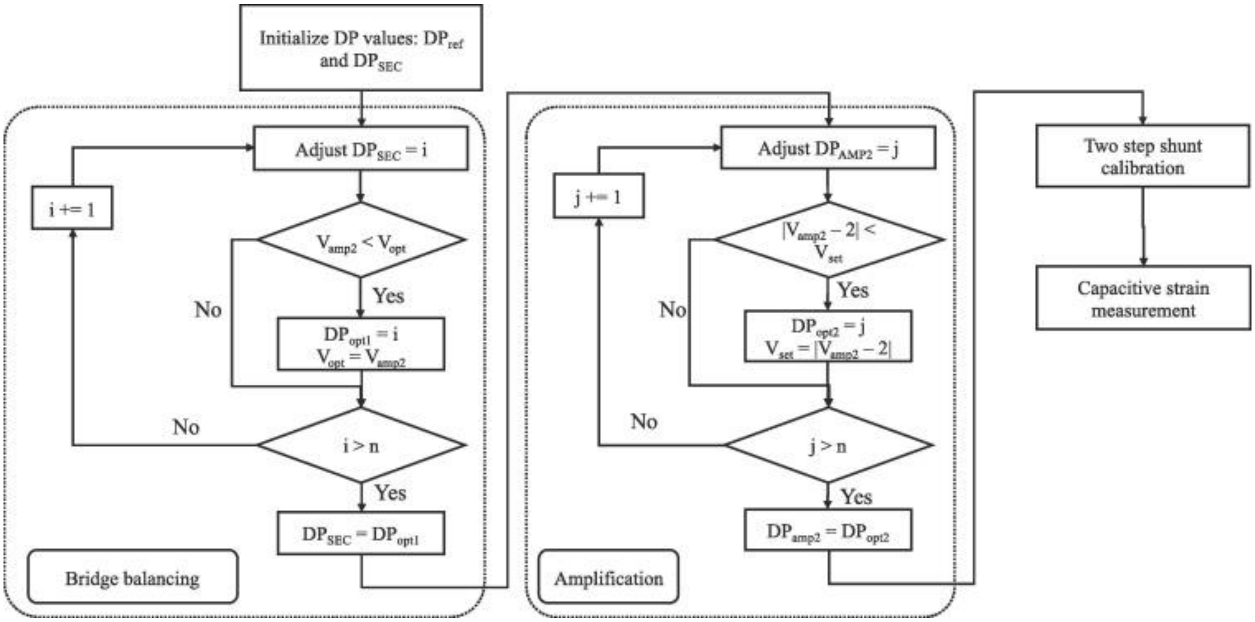

Figure 4.8. Fully automated bridge balancing, amplification and shunt calibration diagram

When powered on, the ATmega328 MCU loads the initial potentiometer values. After initialization, the potentiometer tap on the SEC side changes to *n* steps (i.e., *n* = searching range), while the one on the reference side is fixed. The searching range (i.e., *n* value) can be different depending on the possible capacitance difference between the reference capacitor and SEC. This study used *n* = 50 (out of 256 taps of the selected DP), which was sufficient for covering up to about 5% to 10% capacitance difference. The peak amplitude of the AC signals in the amplification stage significantly varies depending on the bridge balancing status.

$$V_{amp1} = G_1\{V_{REF}\sin(\alpha_1 - V_{SEC}\sin(\alpha_2)) - V_{HPF}\} + V_{REF1} \tag{42}$$

$$V_{amp2} = G_2\{(V_{amp1}) - V_{HPF}\} + V_{REF1} \tag{43}$$

Due to parasitic impedance in the SEC and lead wire, achieving perfect balancing to have exactly the same amplitude and phase between $V_{REF}\sin(\alpha_1)$ and $V_{SEC}\sin(\alpha_2)$ is not possible. An AC component always exists, which represents the difference between the two AC signals from the De-Sauty bridge. Optimal balancing can be achieved when the amplitude difference (between V_{REF} and V_{SEC}) and phase difference (i.e., $\alpha_1 - \alpha_2$) in equation 42 are minimized. The peak voltage levels extracted from a peak-detection circuit of V_{amp1} and V_{amp2} can represent the bridge balancing quality. Once the optimal balancing is achieved, the signal amplification level is adjusted to the desired level. In this study, the amplified signal (V_{amp2}) is adjusted to have a 2 V peak level that may have a sufficient amplification level and margin to the maximum measurable voltage range of Xnode.

In this study, the peak voltage of the second amplifier V_{amp2} is used as an indicator for the bridge balancing quality. The detailed procedures for the proposed automated bridge balancing, amplification, and shunt calibration are summarized as follows:

- Step 1. Potentiometer tab initialized.
- Step 2. Search optimal DP tap (for SEC side) n times: update DP tap for SEC side, compare it with the current V_{amp2} and minimum peak amplitude (V_{opt}), and update V_{opt} and DP_{opt1} if $V_{amp2} < V_{opt}$.
- Step 3. Adjust DP tap for SEC side toDP_{opt1}.
- Step 4. Adjust V_{amp2} amplitude to maximize the sensitivity: update the DP tap for the second amplifier, compare it with the current V_{amp2} and desired peak voltage $V_{amp2\mathrm{out}}$ (i.e., up to 2.4 V, current setup: 2 V), update DP_{opt2} if $V_{amp2} < V_{opt}$.
- Step 5. Adjust DP tap for the second amplifier to DP_{opt2}.
- Step 6. Do two-step shunt calibration.

Figure 4.9 visualizes the automated bridge balancing procedure described above by showing the changes of the AC signals from the De-Sauty bridge (Figure 4.9a) and the first and second amplifiers (Figures 4.9b and 4.9c) while searching the optimal DP taps.

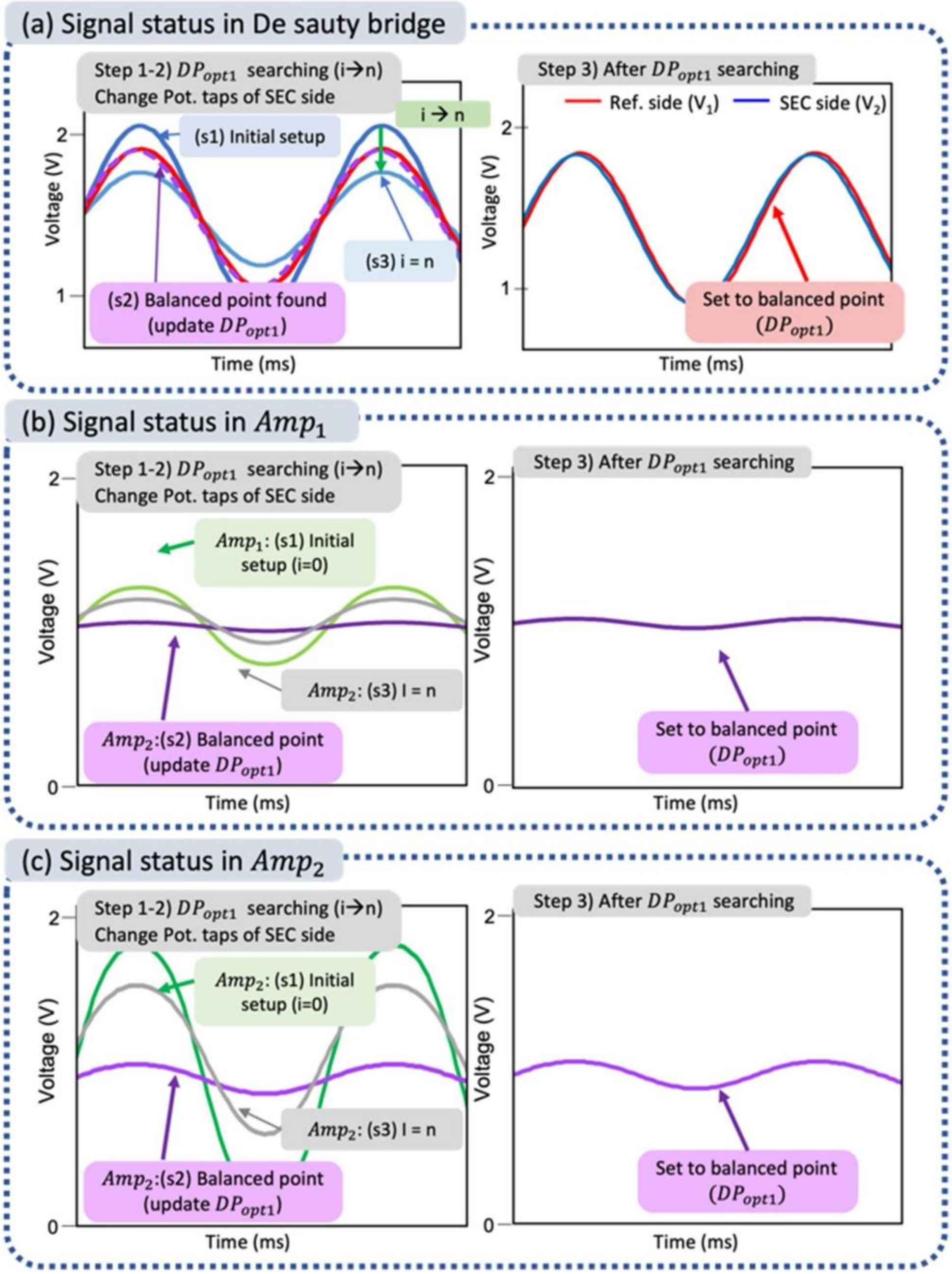

Figure 4.9. Bridge balancing procedure in detail

As shown in the left figure of Figure 4.9a, two signals from the reference side (red line, V_1 in previous Figure 4.2) and SEC side (blue line, V_2 in previous Figure 4.3, s1-initial setup) of the De-Sauty bridge are not matched (i.e., not balanced) in the beginning. Then the amplitude and phase of SEC side's signal (blue) changes according to DP tap changes (i: 0 → n) while updating V_{opt} and DP_{opt1}, as shown with the s2 and s3 in left figure of Figure 4.9a. After that, the SEC side's DP tap is adjusted to DP_{opt1} (i.e., s2 in Figure 4.9) as the optimally balanced setup, because the best match is obtained between the two signals, which is the right figure of Figure 4.9a. Meanwhile, as the balancing status changes (s1-s2-s3), the amplitude of V_{amp2} (AC signal from the second amplifier) changes significantly as shown in the left of Figure 4.9b. The optimal balance case can be determined by identifying the minimum-amplitude case (i.e., s2 in the left figure of Figure 4.9c), which represents the best match between the two signals from the De-Sauty bridge.

In short, the adjustment of SEC side's DP tap to DP_{opt1} will set to the smallest peak amplitude of V_{amp2}. Once the automated balancing is done, the V_{amp2} needs to be adjusted for maximized sensitivity, as discussed in the detailed procedure (steps 4 and 5) described above. Figure 4.10 shows the assembled prototype sensor board for performance validation. Each component has been previously described and consists of basic signal processing circuits, digital components, and peak detection circuits.

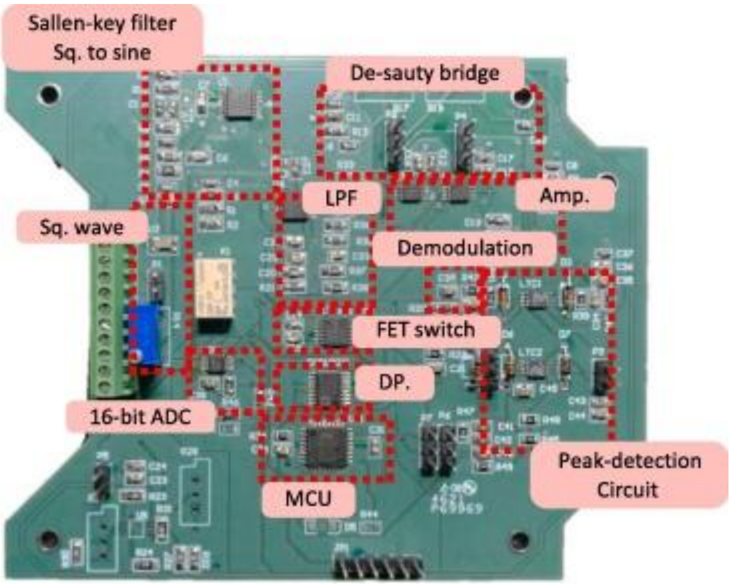

Figure 4.10. Prototype sensor board

Experimental Validation

The performance of the developed sensor board was evaluated through laboratory-scale tests. A static noise test and a cantilever beam free vibration test were conducted for performance validation. Two 3 × 3 in.^{2} (7.6 × 7.6 cm^2) SECs were used for a test having different nominal capacitance (SEC1: 326 pF, and SEC2: 335 pF) shown in Figure 4.11a. Figures 4.11b and 4.11c show the detailed schematic of the test setup.

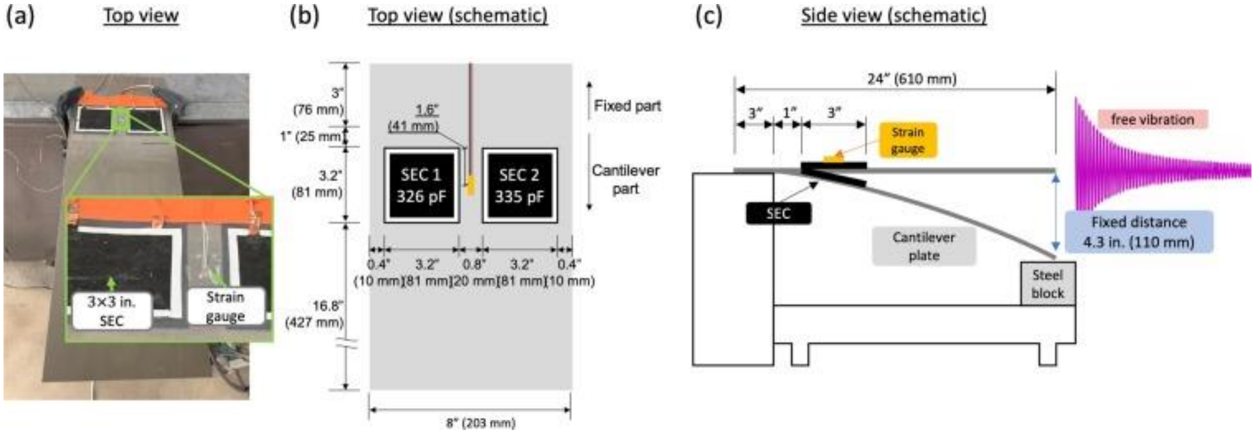

Figure 4.11. Test specimens installed on steel plate cantilever

A 24 × 8 × 0.05 in. (609.6 × 203.2 × 1.3 mm) steel plate was used. Two SECs were installed on the steel plate cantilever for a free vibration test. A foil type strain gauge (OMEGA kFH-3-120-C1-11L3M3R, nominal resistance of 120 ± 0.35 Ω, 2 × 3 mm measurement grid) was installed between the two SECs for comparison. A National Instruments CompactDAQ chassis (cDAQ-9178) was used to collect the voltage output from strain gauge using an NI9235 module and sensor board using NI9234 module. A wired commercial capacitance measurement device PCAP (PCAP02) was used to compare the capacitance sensing performance. The DAQ measurements were sampled at 2 kHz. PCAP measurements were sampled at 110 samples/second.

The free vibration test setup was designed to apply exactly the same vibration history for every test. Figure 4.11c shows the detailed test setup. The cantilever was bended to touch the steel block located below 4.3 in. (110 mm) by pushing the free end point introducing about 400 με as read by strain gauge. The free vibration was generated by releasing the free end. Figure 4.12 shows the strain gauge measurements of two free vibration test results, which match exactly.

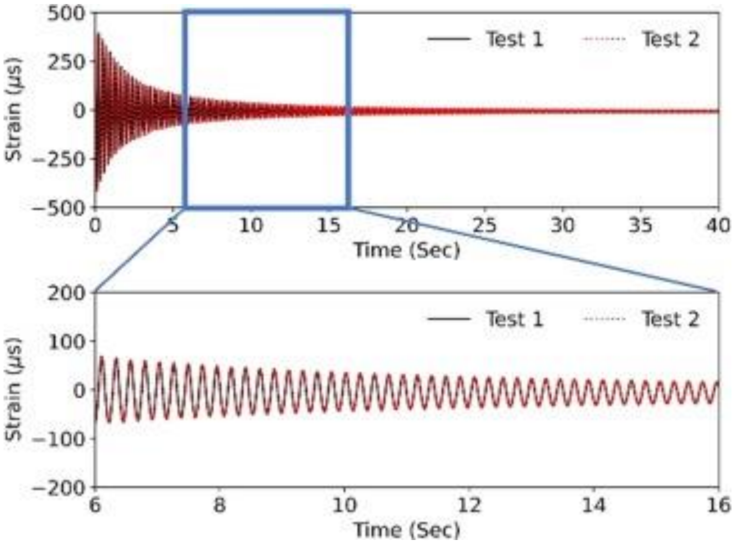

Figure 4.12. Strain response time history from two free vibration tests

Before testing, each SEC was balanced and calibrated to convert the voltage output to absolute capacitance changes. This study selected shunt capacitors as 1 pF and 3 pF to provide a 2 pF difference. Figure 4.13 shows an example of the sensor board output measurement during bridge balancing, amplification, and shunt calibration. The shunt calibration factor for the two SECs are calculated as 0.105 pF/mV for SEC1 and 0.235 pF/mV for SEC2.

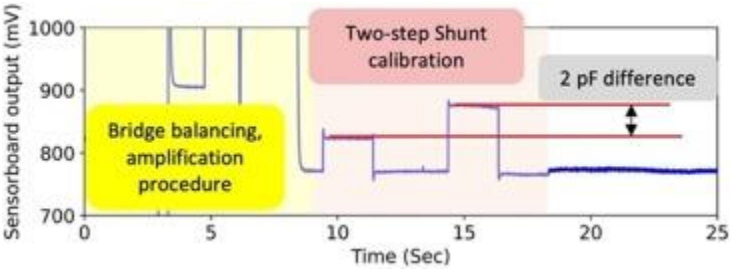

Figure 4.13. Output measurement during automated bridge balancing, amplification, and shunt calibration

The static noise performance of the developed sensor board was evaluated. Considering the high-sensitivity requirement near the microstrain level for SHM applications, the noise performance is critical to capture the ambient structural vibration. The ambient root-mean-square (RMS) noise of the sensor board and PCAP were both measured and compared. The ambient RMS noise of the sensor board was measured as 0.121 pF, and the RMS noise of the PCAP was 0.184 pF at 15 Hz bandwidth. About 34% lower measurement noise than PCAP was achieved from the sensor board in this study. Figure 4.14 shows the ambient noise test results in the time and frequency domains.

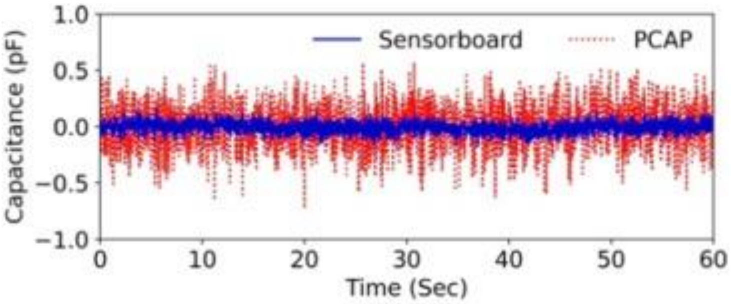

(a) Time history

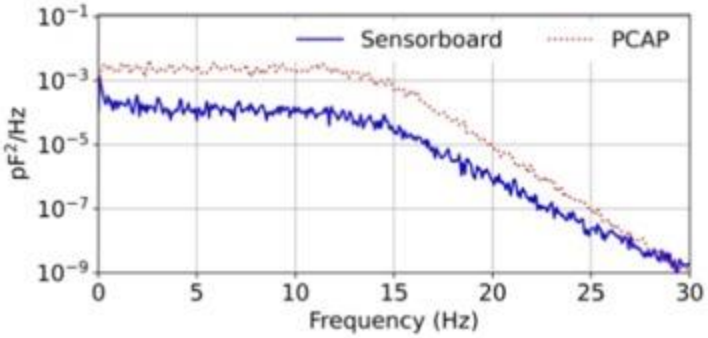

(b) Frequency domain

Figure 4.14. Static noise test results

Free vibration tests were conducted to evaluate the sensor board's performance. Two test cases using two different SECs were conducted and compared with the PCAP measurement. The free-vibration test results from the sensor board connected to the SECs were compared with those from the PCAP measurement. The voltage measurement from sensor board was converted to picofarad (pF) using the calibration coefficient achieved from the previous section.

The dynamic performance of the sensor board was evaluated by free vibration tests. Figures 4.15a and 4.16a show the test measurements from the strain gauge (reference), PCAP, and the new sensor board in the time domain.

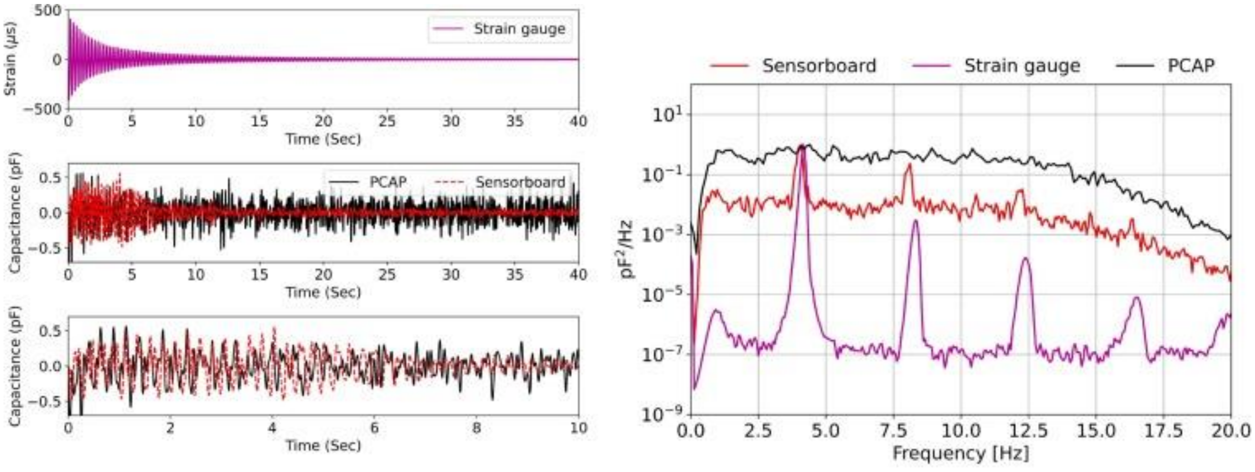

(a) Time history (b) Frequency domain

Figure 4.15. SEC1 test results

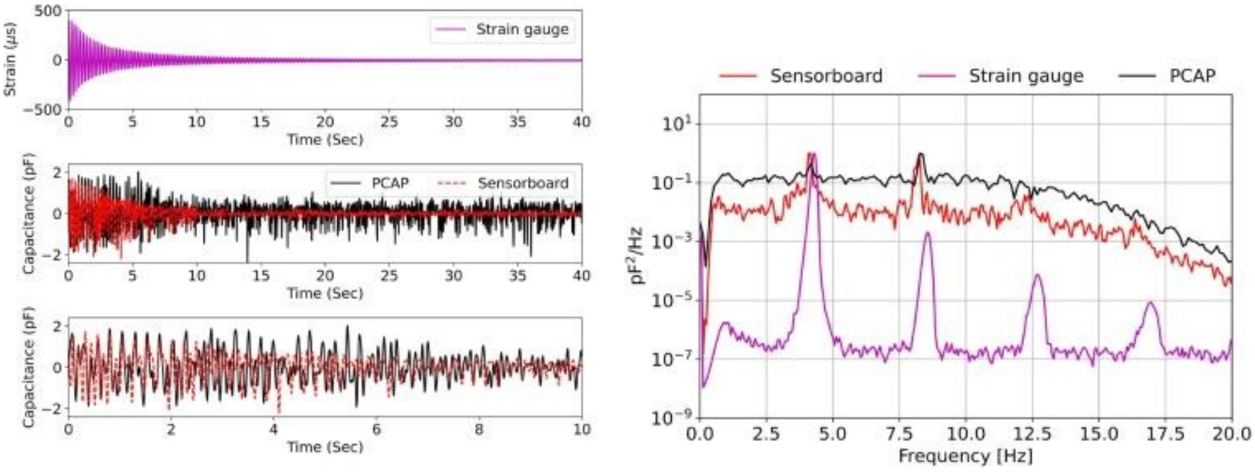

(a) Time history (b) Frequency domain

Figure 4.16. SEC2 test results

The vibration was excited from ±330 με and decayed to ±80 με after 5 seconds. The vibration response was measured for 40 seconds until the strain level reached around ±2 to 3 με. As shown in Figures 4.15 and 4.16, the strain gauge measurements showed clear free-vibration responses and well caught the natural frequency peaks of the cantilever beam, of which the expected first four frequencies are 4.15 Hz, 8.3 Hz, 12.45 Hz, and 16.6 Hz from the eigenvalue analysis, providing the reference information for the test. The test results from the PCAP and new sensor board connected to the SECs showed somewhat noisier measurements than strain gauge data, as expected, due to the SECs' intrinsic characteristic prone to the electromagnetic field noise. However, they showed a very similar trend at the initial stage when the vibration amplitude was large, i.e., around 0 to 5 seconds for both the SEC cases shown in Figures 4.15a and 4.16a. However, the amplitude of the PCAP measurement did not decrease according to the actual vibration amplitude decay due to the high noise floor, while the new sensor board's signal decayed accordingly. Figure 4.15 and 4.16b show the cross PSD (CPSD) of each test case. The CPSDs of different metric measurements were compared based on the capacitance (power) unit (i.e., pF2/Hz) after converting all measurements into picofarad. The PCAP provides the capacitance unit directly, but the sensor board measurements were converted from millivolt to picofarad using the shunt calibration factors that were obtained in a previous section. Also, the strain gauge measurements were converted from microsecond to picofarad with the scale factors (0.001515 pF/µs for SEC1 test and 0.0056 pF/µs for SEC2 test) that were obtained from the time history peak comparison.

While the strain gauge identified multiple clear peaks, including 4.3, 8.4, and 12.9 Hz, the new sensor board identified two to three peaks. Three peaks are clearly identified from the SEC1 case. However, the SEC2 case does not show clear peaks at 12.9 Hz. This can be explained by the intrinsic electrical loss behavior associated with many sensors fabricated from hyper-elastic materials (Pasadas and Jiménez 2016). The PCAP was not able to identify clear peaks due to the high noise floor. The identified frequency peaks have minor differences with the strain gauge measurement caused by differences in the covered geometry area. Consequently, the new sensor board showed better performance compared to the PCAP over the whole frequency range.

Conclusion

This chapter presented the development of the wireless capacitance sensing board. A fully automated wireless capacitive strain sensor board was developed, which can be interfaced with the high-fidelity wireless sensing platform Xnode. A fully automated AC De-Sauty bridge balancing technique was developed with a series of digital circuitries. A low-cost 8-bit microcontroller was employed to control the digital components such as a DP, ADC, and FET bus switch. A peak detection circuit was employed to monitor the high-frequency AC signal effectively using the low-power, 8-bit microcontroller ATmega328P. In addition, an integrated software was newly developed for onboard control of the digital components, allowing fully automated bridge balancing, amplification, and two-step shunt calibration. The performance of the developed hardware and software was validated with the laboratory-scale tests. The developed sensor board successfully balanced the AC De-Sauty bridge, amplified, and was calibrated in a fully automated fashion for high sensitivity capacitive strain sensing. A series of laboratory tests validated that the developed new sensor board outperformed the commercial wired capacitance measurement system PCAP02. The developed sensor board showed about 34% lower measurement noise than the PCAP02 and confirmed that the automated control features worked as designed.

CHAPTER 5: FIELD VALIDATION OF WIRELESS LARGE-AREA STRAIN SENSORS

This chapter is extracted from the following publication:

Taher, S. A., J. Li, J.-H. Jeong, S. Laflamme, H. Jo, C. Bennett, W. Collins, and A. R. Downey. 2022. Structural Health Monitoring of Fatigue Cracks for Steel Bridges with Wireless Large-Area Strain Sensors. *Sensors*, Vol. 22, No. 14.

Overview

This chapter presents the field validation of the wireless large-area strain sensors (WLASS). To validate the integrated wireless fatigue crack monitoring system, a field deployment was conducted on a steel highway bridge that is subject to fatigue damage. Several SEC and cSEC sensors were deployed over fatigue-susceptible regions, and the newly developed wireless capacitive sensing boards were also deployed for measuring the capacitances of the sensor under traffic loads. A modified CGI based on the wavelet transform was developed to process real-world nonstationary traffic-induced bridge response signals, and field results verified that the wireless fatigue crack monitoring system is capable of offering the basis for long-term fatigue crack monitoring on steel bridges.

Problem Statement

Prior studies have demonstrated the effectiveness of the large-area strain sensor, SEC, for fatigue crack monitoring in the laboratory environment. However, the laboratory studies utilized a wired DAQ system and were based on simplifying the traffic loading as a harmonic function, whereas real traffic-induced bridge responses consist of impulsive signals. To fill these gaps in the knowledge and transfer this technology from the laboratory to the field for long-term bridge fatigue crack monitoring, this study presents two critical novelties: (1) by integrating the SEC with the Xnode sensing platform, a WLASS was created to wirelessly collect the large-area strain data to support fatigue crack monitoring and (2) an effective automated algorithm was developed based on the wavelet transform to process the traffic-induced bridge response data consisting of numerous impulsive peak events for monitoring fatigue crack growth.

This study was motivated by the pressing need for reliable SHM of fatigue cracks for civil infrastructure. In particular, distortion-induced fatigue cracks in steel bridges are the focus of this study. Distortion-induced fatigues typically happen at web-gap regions of steel girder bridges where the girder web, flange, and connection plates meet. Figures 5.1a and 5.1b illustrate the mechanism of the distortion-induced fatigue in the girder web of a steel bridge.

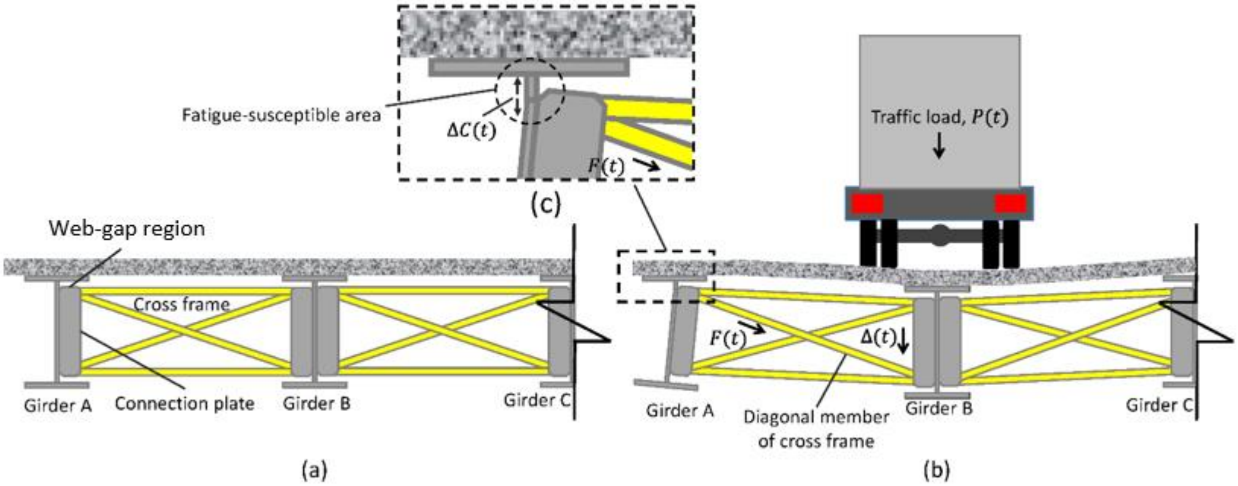

Figure 5.1. Distortion-induced fatigue of steel bridges: (a) girders with no traffic loading, (b) girders with traffic loading, and (c) fatigue crack developed at the web-gap region

A steel bridge consists of cross-frames connected with girders by transverse connection plates. For most steel girder bridges built before the mid-1980s in the United States, the connection plates are not welded to the flanges, creating web-gap regions located between the connection plate and the flanges. As shown in Figure 5.1b, under traffic loading, $P(t)$, adjacent girders face differential displacement, Δt, leading to out-of-plane force, $F(t)$, being exerted on the girder web by the cross-frames through the transverse connection plates. Since the web-gap is flexible, the out-of-plane force, $F(t)$, of the cross-frame causes distortion-induced fatigue and further leads to fatigue cracks around the fatigue-susceptible area (see Figure 5.1c). More details about distortion-induced fatigue cracks can be found in Jajich and Schultz (2003), Berglund and Schultz (2006), and Mahmoud and Miller (2016).

According to the crack-sensing mechanism, in laboratory studies (Kong et al. 2017b, Kong et al. 2018), the CGI was proposed as the ratio between $\Delta C(t)$ and $F(t)$. Because the traffic loading was simplified as a harmonic function, a Fourier transform was used to obtain the magnitudes of both $\Delta C(t)$ and $F(t)$ from noisy measurements. However, in practice, under real-world random traffic events, the field data of $F(t)$ and $\Delta C(t)$ are nonstationary signals consisting of unevenly distributed impulsive components, which are also contaminated by noise and low-frequency drift. As a result, the CGI based on the Fourier transform would no longer be able to extract reliable information for fatigue crack monitoring. To address this challenge, this study developed a modified CGI based on the wavelet transform to process real-world nonstationary traffic-induced bridge response signals. In addition, a WLASS was developed to replace the wired DAQ system used in the laboratory studies, enabling long-term autonomous fatigue crack monitoring in the field. In the next section, the main methodology is presented, including both the hardware and algorithmic aspect of the developed WLASS.

Background of Sensing Hardware

This study aimed to enable wireless sensing with a large-area strain sensor, SEC, for long-term fatigue crack monitoring in field applications. To this end, the Xnode wireless smart sensor platform (Spencer et al. 2017, Fu et al. 2018, Hoang et al. 2020) developed for SHM applications was selected for its flexible interface with external sensors, reliable wireless communication, high sampling rate, sensing resolution, and rugged design. As shown in Figure 5.2a, the Xnode sensor consists of three boards, including a sensor board, a radio and power board, and a processor board, as well as a lithium-ion battery that can be charged using a solar panel.

Figure 5.2. Xnode wireless smart sensor platform: (a) Xnode sensor node and (b) breakout box

The radio board, along with the antenna, offers a line-of-sight communication distance of 3 km (Fu et al. 2019). To enable event-triggered sensing mode, a lower-power trigger accelerometer, ADXL362 by Analog Devices, was adopted in the Xnode (Fu et al. 2018). Through a predefined acceleration threshold, an event-triggered sensing mode can be used to only measure significant vibration events, resulting in improved power efficiency for long-term fatigue crack monitoring. The Xnode sensor network contains sensor nodes responsible for sensing and one gateway node that communicates with personal computers (PCs) and sensor nodes to receive the measured data. In this study, a cellular gateway node equipped with a 4G-LTE modem for data transmission, cloud storage, and remote data retrieval developed in Hoang et al. (2020) was utilized. In addition, the Xnode sensor was equipped with a 24-bit ADC with eight sensing channels. The onboard triaxial accelerometer uses the first three channels to measure accelerations in the x, y, and z directions, while the remaining five channels can be used to measure analog voltage signals from external sensors such as strain gauges, including the SEC used in this study. Thus, to ensure robust connections, a breakout box shown in Figure 5.2b is used to connect the SECs to the Xnode through the connectors.

The five extra channels of the Xnode accept analog voltage signals ranging from 0 to 2.4 V. To achieve wireless sensing for the SEC, as shown in Figure 5.3a, a capacitive sensor board (Jeong et al. 2018a, 2018b) that converts the capacitive large-area strain signal, $\Delta C(t)$, from the SEC to voltage signal was developed, which enables using the SEC with the Xnode wireless sensing platform and enhancing the quality of large-area wireless strain measurement (Jeong et al. 2018b).

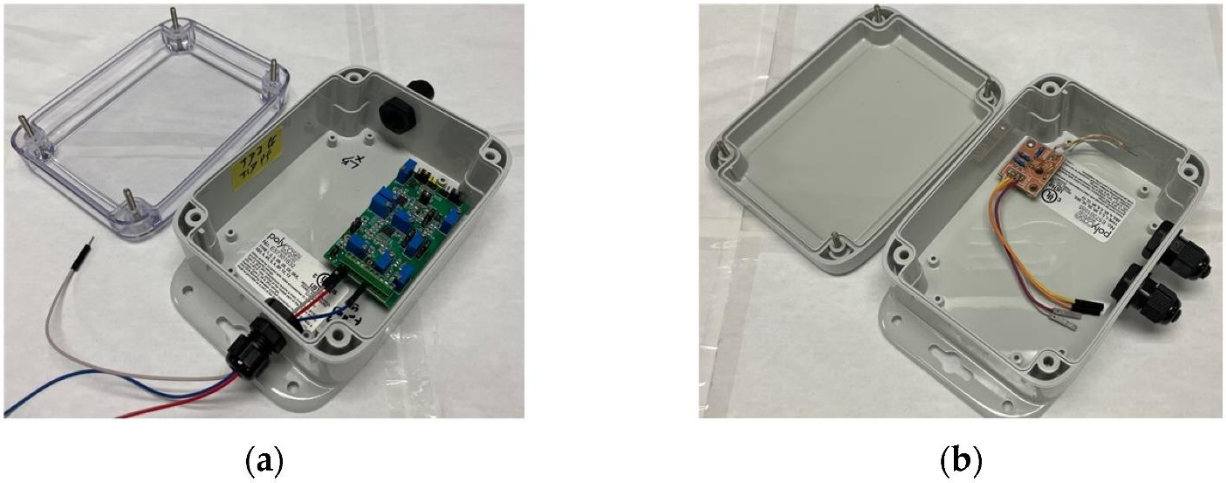
(a) (b)

Figure 5.3. (a) Capacitive sensor board and (b) Wheatstone bridge packaged in a weatherproof enclosure

The capacitive sensor board was designed to use the 3.3 V power supply from the Xnode and receive the $C(t)$ signal from SEC and convert it to a measurable change in voltage, which falls within the input voltage range (0 to 2.4 V) of the external channels. Moreover, a two-step shunt calibration process was included in the capacitive sensor board to carry out accurate and robust onboard calibration for capacitance measurement. More details about the capacitive sensor board can be found in Jeong et al. (2018a, 2018b). In this research, the capacitive sensor board was packaged in a weatherproof enclosure, as shown in Figure 5.3a.

The developed algorithm, which will be discussed in the following section, requires the information of the $\Delta C(t)$ normalized by $F(t)$. Thus, the out-of-plane force, $F(t)$, of the cross-frame is indirectly captured using a foil-type strain gauge. To enable wireless strain sensing with the external analog channels of the Xnode, a DC Wheatstone bridge (Jo et al. 2013) shown in Figure 5.3b was used to indirectly measure the out-of-plane force, $F(t)$, of the web-gap region exerted by the cross-frame. The output signal obtained from the Wheatstone bridge is given in voltage. Thus, the following equation is used to convert the voltage signal to strain (Jo et al. 2013):

$$\Delta V = \frac{GF \times \varepsilon}{4} V_{EXT} \tag{44}$$

where ΔV is the output voltage, GF is the gauge factor of the strain gauge, ε is the strain to indirectly capture the out-of-plane force $F(t)$, and V_{EXT} is the excitation voltage. Here, since the Wheatstone bridge was also powered by the Xnode, the V_{EXT} is equal to 3.3 V. The Wheatstone bridge was also packaged in a weatherproof enclosure (see Figure 5.3b).

The developed WLASS is summarized in Figure 5.4.

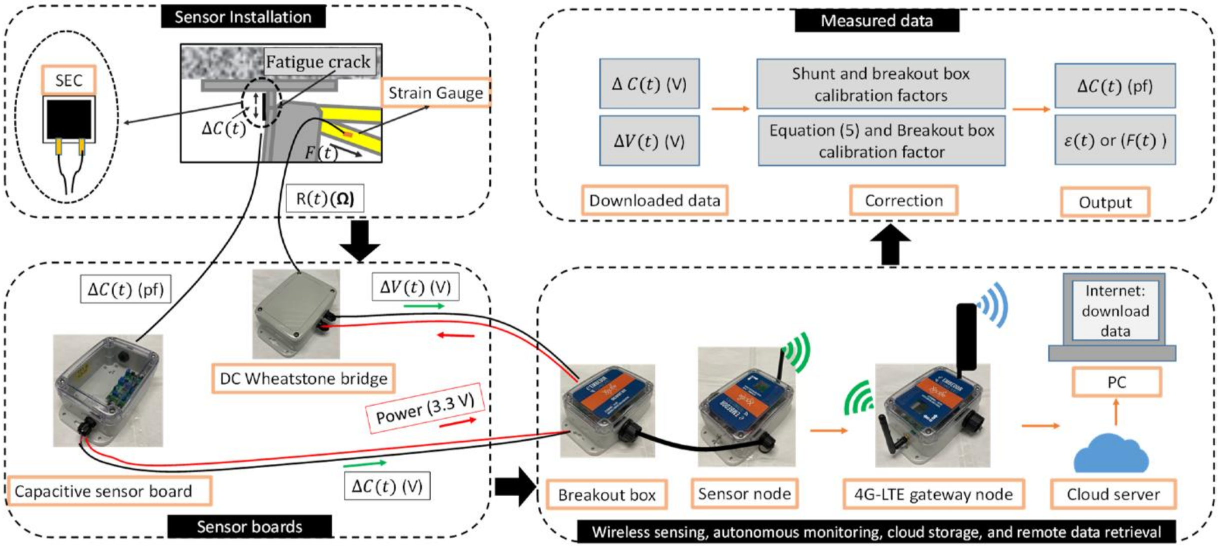

Figure 5.4. WLASS for wireless sensing, cloud storage, and remote data retrieval for fatigue crack monitoring

As illustrated in the figure, the $\Delta C(t)$ and $F(t)$ signals are measured by the SECs and strain gauge through the capacitive sensor board and DC Wheatstone bridge, respectively. The sensor node equipped with the breakout box supplies the 3.3 V power to the capacitive sensor board and the DC Wheatstone bridge, which return voltage signals for the $\Delta C(t)$ and $F(t)$, respectively, to the sensor node. The cellular gateway node communicates with the sensor node to receive measured signals and upload them to the cloud server. The cloud data can be accessed using a PC through the internet and a web browser. Finally, $\Delta C(t)$ and $F(t)$ are obtained by first applying the breakout box factor, followed by the shunt calibration coefficient and the electromechanical model of the SEC, respectively.

WLASS Algorithm for Fatigue Crack Monitoring

The developed algorithm for fatigue crack monitoring is discussed in this section. The algorithm contains three steps: automated traffic event detection, a generalized Morse continuous wavelet transform (GM-CWT) and peak identification, and a modified CGI, to compute the modified CGI in the presence of a nonstationary signal with numerous impulsive peak events due to traffic loading, as explained in this section.

The premise of the algorithm for fatigue crack monitoring is that the initiation and propagation of fatigue cracks introduce an increase in the local strain response around the cracked region, causing it to be out of proportion to the applied loading. In other words, once normalized against the loading, the local strain response would increase if a new crack develops or an existing crack propagates further. As a result, identifying the amplitudes of the large-area strain, $\Delta C(t)$, and the strain-based, indirectly measured out-of-plane force, $F(t)$, under traffic loading is critical to successful crack growth monitoring (see the previous Figure 5.1). In particular, the amplitude of $\varDelta C(t)$ is normalized by $F(t)$ to remove the influence of the changing load amplitude, leading to the CGI.

As shown in Figure 5.5a, both $F(t)$ and $\varDelta C(t)$ data are nonstationary signals and contain impulsive components due to traffic events, as well as noise and low-frequency drift.

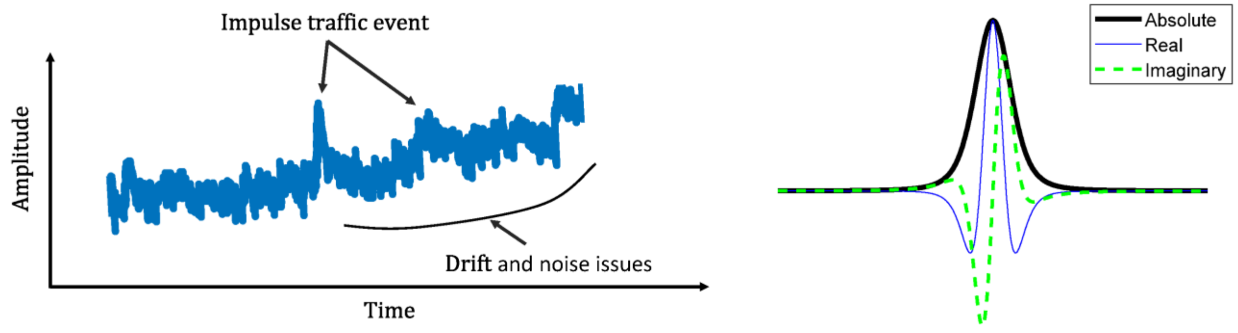

(a) (b)

Figure 5.5. (a) Typical signal under traffic loading using the WLASS and (b) shape of the generalized Morse wavelet with γ = 1.5 and P^2 = 3

As mentioned previously, extracting the amplitude information from those signals based on a Fourier transform and calculating the CGI is challenging. In this study, the CWT designed for processing nonstationary signals (Lilly and Olhede 2009) was adopted to reliably extract the amplitudes corresponding to the impulsive loading events, based on which the modified CGI is proposed. The CWT decomposes a signal into the time-frequency domain, which enables an accurate characterization of the signal's changing energy level over time at various frequencies. The mathematical formula of the CWT for signal $x(t)$ is expressed as follows (Lilly and Olhede 2009, Lilly and Olhede 2012):

$$W(t,s) = \int_{-\infty}^{\infty} \frac{1}{s} \varphi^{*}(\frac{\tau - t}{s}) x(\tau) d\tau \qquad (45)$$

where $W(t,s)$ is a matrix with complex values that carries information about the amplitudes of wavelet coefficients, φ is the wavelet function, in which the asterisk denotes the complex conjugate, and t and s are time and scale parameters, respectively. Note that $x(t)$ can be $\Delta C(t)$ or $F(t)$ in this study. Time-frequency analysis with the CWT for nonstationary signals depends on the wavelet function φ. To this end, the GM-CWT developed in Olhede and Walden (2002), Lilly and Olhede (2009), and Lilly and Olhede (2012) were chosen for their ability to imply various analytic wavelets by adjusting their parameters, which are formulated as follows (Lilly and Olhede 2009, Lilly and Olhede 2012):

$$\varphi_{P,\gamma}(w) = U(w) a_{P,\gamma} \omega^{\frac{P^2}{\gamma}} e^{-\omega\gamma} \qquad (46)$$

where $U(\omega)$ is the Heaviside step function, γ and P^2 are the GM-CWT parameters to control the symmetry and the oscillations of the wavelet, and $a_{p,\gamma}$ is a normalizing constant. By adjusting both (γ,P^2) parameters, various shapes of wavelets can be achieved. Specifically, to extract the amplitudes for the impulse events due to traffic loading, γ = 1.5 and P^2 = 3 are chosen in this study. The shape of the wavelet based on the chosen parameters is shown in Figure 5.5b. The Wavelet toolbox in the MATLAB R2021a program was used in this study, in which L1 normalization was utilized for a more accurate representation of the signal (MATLAB 2021). Compared to other shapes of wavelets, such as the Morlet wavelet, Bessel wavelet, Cauchy wavelets, etc., the selected shape can effectively separate and extract the amplitude information of impulse traffic events. The algorithm is summarized in the following sections.

WLASS Algorithm Step 1

Automated traffic event detection: The impulse traffic events are automatically detected from F(t) to obtain the times when the peak strain events occur. Define $I = [I_1, I_2, \dots, I_n]$, $F = [F_1, F_2, \dots, F_n]$, and $t = [t_1, t_2, \dots, t_n]$, in which F contains the values of the detected peaks, t has the times associated with the peaks, I includes the indices of the detected peaks, and n is the total number of detected peaks. First, the local maxima of time history are identified based on the change of derivatives. Then, the local maxima that exceed a predefined threshold value, h, are retained as the detected peaks. In this study, the $F(t)$ threshold of h = 30 με was selected as the threshold to ensure large enough events were kept. In addition, a minimum peak distance of t_d was also implemented to avoid closely spaced peaks, in which a value between 1 second and 2 seconds is recommended for traffic loads. Here, t_d = 1.3 seconds is assumed.

WLASS Algorithm Step 2

GM-CWT and peak identification: Using the proposed GM-CWT, $|W(t,s)|_C$ and $|W(t,s)|_F$ are computed for Δ*C(t)* and *F(t)* signals, respectively. To identify robust peak values embedded in $|W(t,s)|_C$ and $|W(t,s)|_F$ associated with traffic events for computing the modified CGIs, windows of interest (WOI) based on the detected traffic events in Step 1 are first defined as $\mathrm{WOI}_i = [t_i - t_d, t_i + t_d]$, where $i = 1, 2, \dots, n$. Subsequently, $|W(t,s)|_{Ci}^{max}$and $|W(t,s)|_{Fi}^{max}$, which are the maximum values of $|W(t,s)|_C$ and $|W(t,s)|_F$, respectively, associated with the detected traffic events are obtained within each WOI_i. Note that $|W(t,s)|_{Ci}^{max}$ is obtained using two cases. In Case-1, $|W(t,s)|_{Ci}^{max}$ is computed using the index of $|W(t,s)|_{Fi}^{max}$, the location of $|W(t,s)|_{Fi}^{max}$, by assuming the peak events of $\Delta C(t)$ and $F(t)$ occur at the same time, while $|W(t,s)|_{Ci}^{max}$ for Case-2 is calculated based on the maximum values of $|W(t,s)|_C$ within the WOI_i.

WLASS Algorithm Step 3

The modified CGI: The modified CGI, which is an indicator for monitoring fatigue cracks, is computed for each peak event as follows:

$$CGI_i = \frac{|W(t,s)|^{max}_{C_i}}{|W(t,s)|^{max}_{F_i}} \tag{47}$$

The CGI records the peak average strain under the SEC sensor normalized by the indirect out-of-plane force $F(t)$ under traffic loading. In this study, the mean of CGI_i, $\overline{\mathrm{CGI}}$, and the associated standard deviation based on impulsive traffic events recorded during one to two days with a minimum of two events are computed to show the results of the crack monitoring. Potential crack initiation and propagation are represented by changes in $\overline{\mathrm{CGI}}$. As illustrated in Figure 5.6, $\Delta C(t)$ and $F(t)$ are obtained from the WLASS under traffic loading.

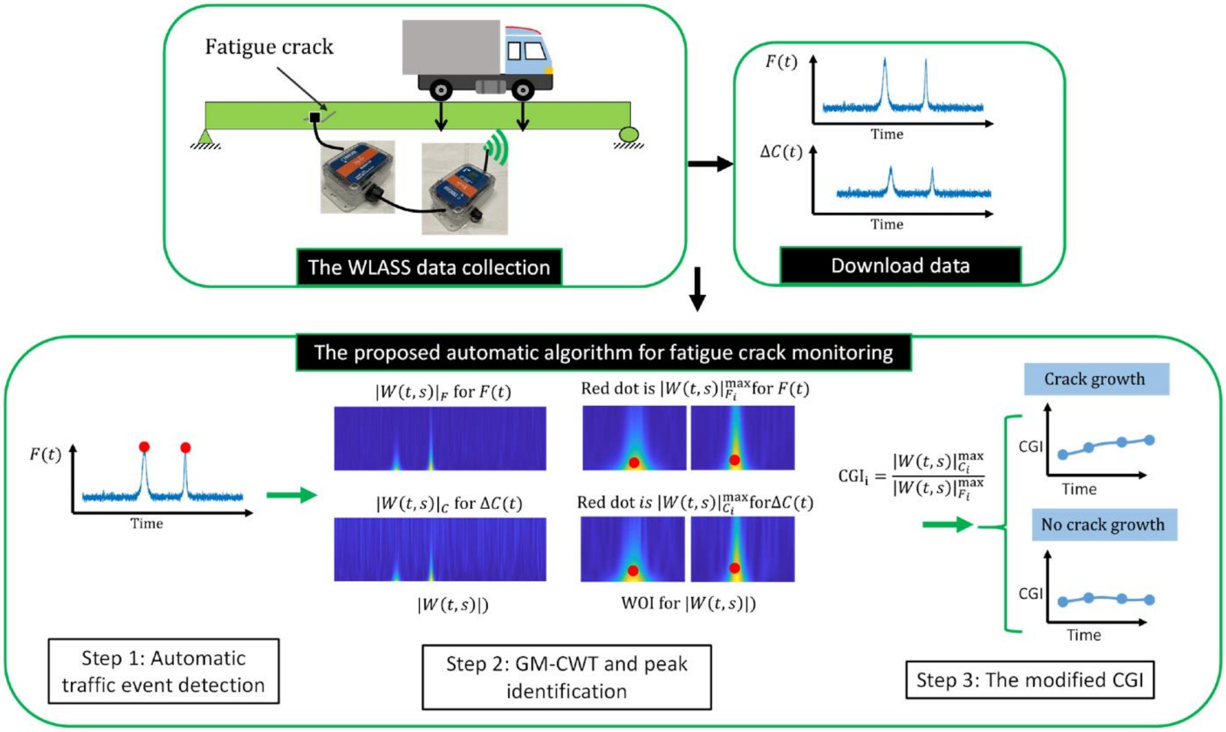

Figure 5.6. Workflow of the automated algorithm for fatigue crack monitoring

Subsequently, the measured data are processed with the proposed algorithm for fatigue crack monitoring. Specifically, using $F(t)$, the impulsive traffic events are automatically detected through Step 1. Next, using the proposed GM-CWT in Step 2, $|W(t,s)|_C$ and $|W(t,s)|_F$ are computed for $\Delta C(t)$ and $F(t)$, respectively. Consequently, the WOIs for $|W(t,s)|_C$ and $|W(t,s)|_F$ are identified based on the peak detections in Step 1, and the peak amplitudes, $|W(t,s)|^{max}_{Ci}$and $|W(t,s)|^{max}_{Fi}$, are estimated within the WOIs. Finally, in Step 3, the modified CGIs are computed based on $|W(t,s)|^{max}_{Ci}$and $|W(t,s)|^{max}_{Fi}$ using equation 47 from Step 3 to monitor crack growth. As illustrated in Figure 5.6, if the crack grows, the CGI would gradually increase. Otherwise, the CGI remains constant if there is no crack growth.

Field Validation for Fatigue Crack Monitoring

Selection of a Fatigue Crack Location and the WLASS Installation

The performance of the WLASS and automated algorithm for fatigue crack monitoring were examined using a field bridge. As shown in Figure 5.7a, the field validation was carried out on a steel highway bridge, designated the 70-105-41732-128 (eastbound) bridge on I-70 near Kansas City, Kansas, located at the intersection with North 57th Street.

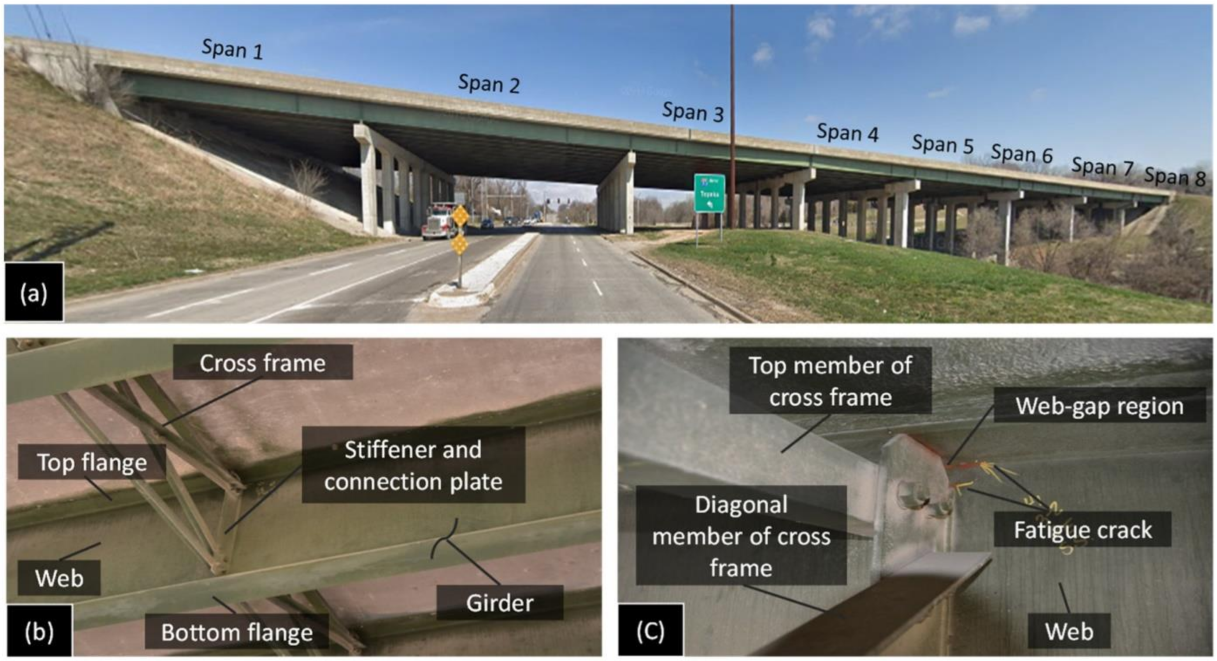

Figure 5.7. I-70 bridge: (a) span layout of the bridge, (b) cross-frame between the adjacent girders, and (c) detail of the web-gap region with distortion-induced fatigue cracks

According to the inspection reports by the Kansas DOT (KDOT), multiple locations on the bridge are subjected to fatigue damage and have existing fatigue cracks, which are mainly distortion-induced fatigue cracks located at the cross-frame-to-girder connections and the web-gap regions. Figure 5.7c shows two sample fatigue cracks in the bridge, with one located at the web-gap region along the weld between the cross frame and girder-to-web connection plate and another one along the weld toe between the girder flange and web. As discussed previously, these cracks are caused by the differential movement between the two adjacent girders, which leads to the out-of-plane force on the girder web by the cross-frame, resulting in the initiation and propagation of the fatigue cracks.

The selection of a fatigue crack location and WLASS installation are discussed in this section. A man-lift truck was used to facilitate access to the steel girders and the WLASS installation (see Figure 5.8).

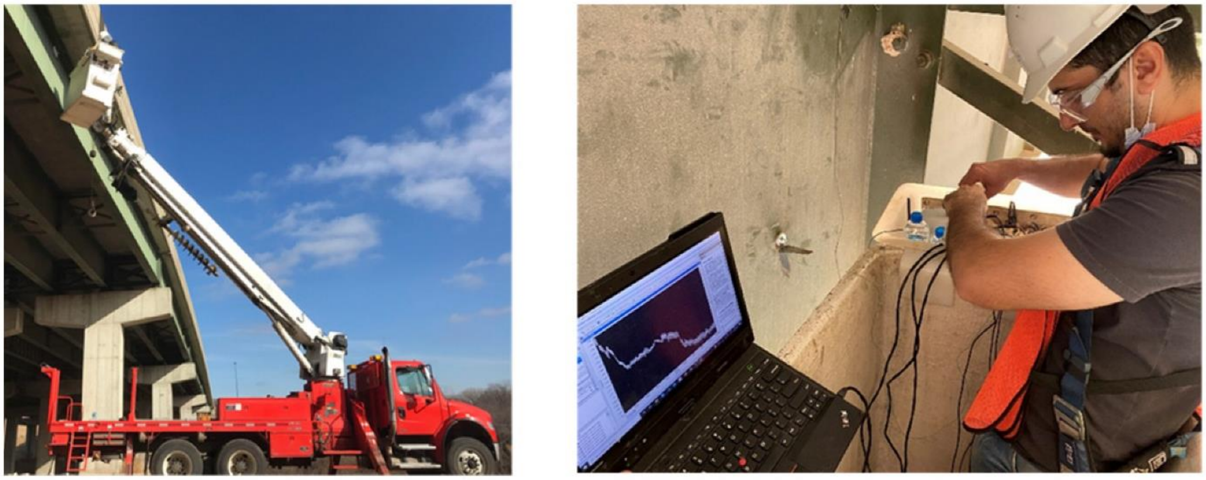

Figure 5.8. Man-lift truck to access the regions with cracks in the bridge girders

The interior side of the exterior girder within Span 3 shown previously in Figure 5.7a was chosen for field validation. In the steel girder, a transverse connection plate connects the cross-frame to the girder web. A distortion-induced fatigue crack due to the differential movement between the two adjacent girders had been growing around the web-gap region along the weld between the transverse connection plate and the girder web, which also propagated into the web, as shown in Figure 5.9a.

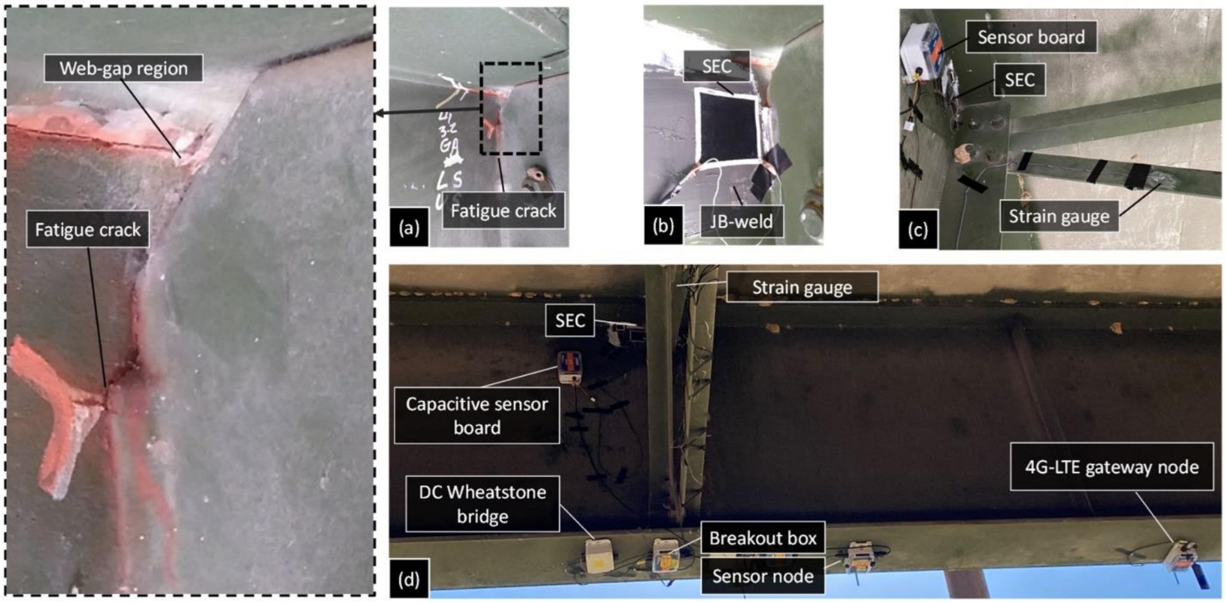

Figure 5.9. Installation of the proposed WLASS: (a) fatigue crack, (b) SEC, (c) strain gauge, and (d) installation of the WLASS

Therefore, this distortion-induced fatigue crack region and the diagonal member of the cross-frame were instrumented with the WLASS as illustrated in Figure 5.9. Particularly, a large-area strain sensor, SEC, was installed on the girder web to cover the fatigue crack and capture the average strain, $\Delta C(t)$, in the cracked region. Meanwhile, a strain gauge was attached to one diagonal member of the cross frame to indirectly measure the out-of-plane force, $F(t)$. The structural surfaces were sanded to remove paint and cleaned up for installing the SEC and the strain gauge. A two-part epoxy (J-B Weld) was used to install the SEC, while adhesive and coating were applied to install the strain gauge on the cross frame (see Figures 5.9b and 5.9c). Subsequently, other components of the WLASS, including the capacitive sensor board, DC Wheatstone bridge, breakout box, wireless sensor node, and the 4G cellular gateway were installed based on the schematic described previously in Figure 5.4. Figure 5.9d provides an overview of the WLASS installation on the steel bridge. The capacitive sensor board was installed close to the SEC to minimize the cable length and hence noise for capacitance measurement, while the DC Wheatstone bridge, breakout box, sensor node, and 4G cellular gateway were attached to the bottom flange as shown in the figure. After completing the installation, AC bridge balancing and shunt calibration was performed for the capacitive sensor board of the SEC (see the previous Figure 5.8). Finally, the WLASS was ready to collect $\Delta C(t)$ and $F(t)$ data (see previous Figure 5.4 for more details).

Data Collection and Processing

To enable energy-efficient, long-term monitoring, the event-triggered sensing mode was used to capture significant traffic loading events and collect meaningful data using the WLASS through a predefined triggering acceleration threshold. In particular, event-triggered sensing was based on the acceleration response at the bottom flange where the sensor node was installed. After monitoring the vibration levels of the bottom flange due to traffic loading for a short period of time, acceleration thresholds between 150 mg and 250 mg were used, such that only significant loading events were measured for long-term fatigue crack monitoring. Figure 5.10 shows an example of raw acceleration measurements in lateral (*x*) and vertical (*z*) directions, large-area strain, $\Delta C(t)$, and cross-frame strain, $F(t)$.

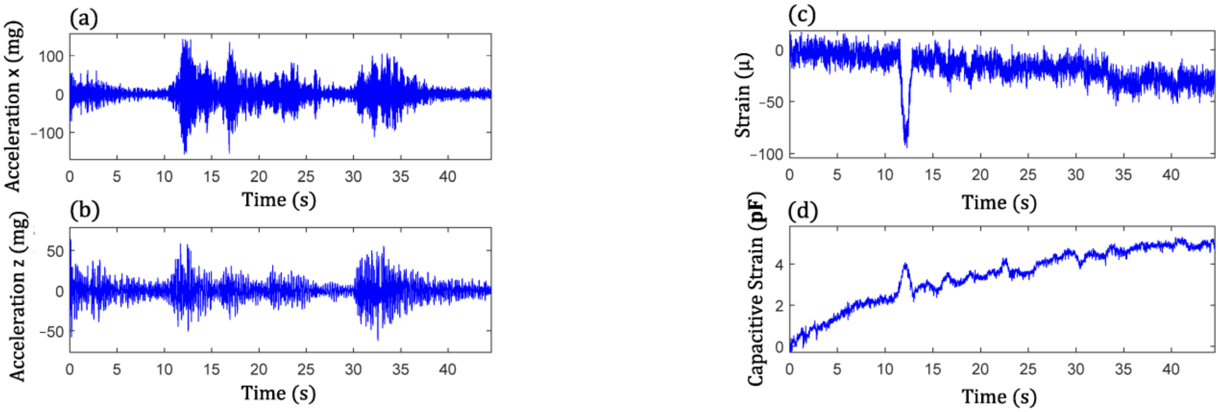

Figure 5.10. Sample data set from the WLASS including: (a) lateral acceleration and (b) vertical acceleration; (c) cross-frame strain, $F(t)$; and (d) large-area strain, $\Delta C(t)$

The acceleration measurements indicated several traffic loading events through high acceleration levels. The acceleration in the longitudinal direction (*y*) is not shown here, since it has a much lower level of vibration compared to other directions. From Figures 5.10c and 5.10d, a large impulsive event due to the traffic loading can be seen clearly between 11 and 13 seconds, which also matches with the first peak acceleration event in both the lateral and vertical directions. Note that the acceleration response of the girder flange in the lateral direction dominated this event with a peak acceleration of around 150 mg, which is also the case for the cross-frame strain $F(t)$, and $\Delta C(t)$ as the first peak dominated the measurement.

GW-CWT Results

Step 2 in the algorithm extracts the signal components of the peak events and is illustrated using two examples. The examples consider both single and multiple traffic events. Figure 5.11 shows the acceleration responses in the lateral and vertical directions for the single traffic event. The high amplitude accelerations in the data are due to the traffic loading.

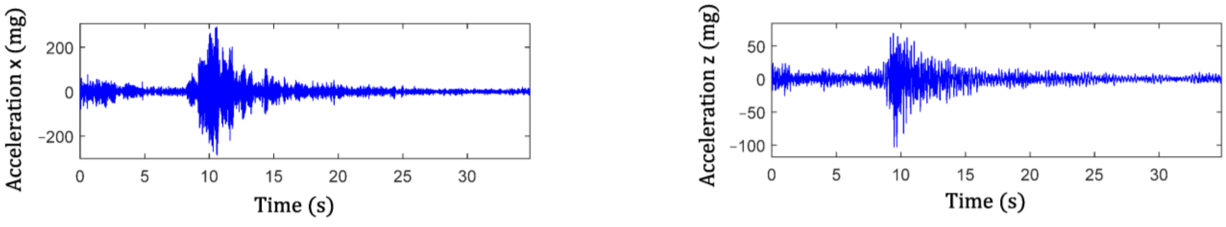

(a) (b)

Figure 5.11. Acceleration measurements containing single impulsive traffic event: (a) lateral direction and (b) vertical direction

Figures 5.12a and 5.12c show the associated cross-frame strain measurement, $F(t)$, and large-area strain, $\Delta C(t)$, signals, respectively.

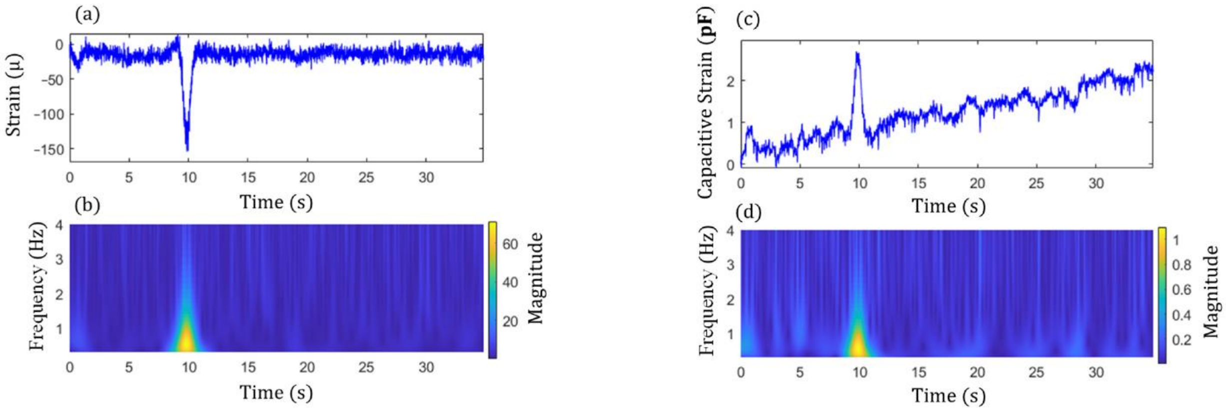

Figure 5.12. Single impulse traffic event: (a) raw data and (b) magnitude, and $|W(t,s)|_F$, of cross-frame strain, $F(t)$, and (c) raw data and (d) magnitude, $|W(t,s)|_C$, of large-area strain, $\Delta C(t)$

For multiple traffic events, the corresponding measurements are shown in Figure 5.13 and Figures 5.14a and 5.14c.

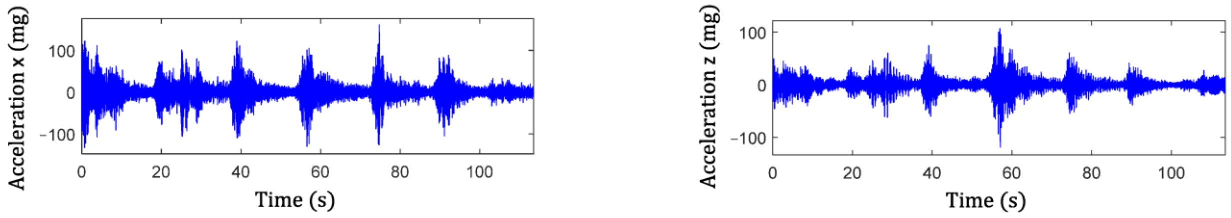

(a) (b)

Figure 5.13. Acceleration measurements containing multiple impulse traffic events: (a) lateral direction and (b) vertical direction

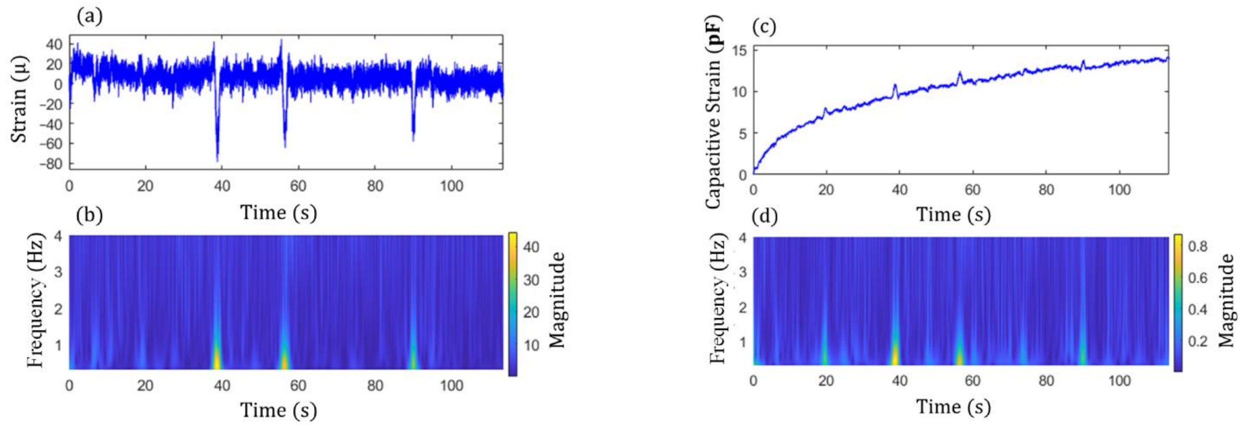

Figure 5.14. Multiple impulse traffic events: (a) raw data and (b) magnitude, $|W(t,s)|_F$, of cross-frame strain, $F(t)$, and (c) raw data and (d) magnitude, $|W(t,s)|_C$ of large-area strain, $\Delta C(t)$

The impulsive events due to the traffic loadings are observed from the signals. Moreover, the impulse events again match with the high amplitude oscillation events of the accelerations for both the single and multiple traffic events. Note that, as shown in the figures, both $F(t)$ and $\Delta C(t)$ are nonstationary and have noise, and $\Delta C(t)$ has significant low-frequency drifts.

Subsequently, the magnitudes of GM-CWT described in Step 2 of the algorithm, $|W(t,s)|_C$ and $|W(t,s)|_F$, were calculated for $\Delta C(t)$ and $F(t)$ for both examples, respectively. The sampling rate was 100 Hz, and the lower and upper cutoff frequencies were chosen as 0.3 Hz and 4 Hz, respectively, for the GM-CWT to remove high-frequency noise and low-frequency drift. As mentioned previously, GM-CWT parameters of $\gamma = 1.5$ and $P^2 = 3$ were chosen to control the symmetry and the oscillations of the wavelet in this study. The results of $|W(t,s)|_F$ and $|W(t,s)|_C$ under the single and multiple traffic, events are shown in Figures 5.12b and 5.12d and Figures 5.14b and 5.14d, respectively. The hot spots in the figures indicate the extracted amplitude information in both the time and frequency domains, which are associated with impulsive traffic events. The second part of Step 2 extracts the amplitude information from $|W(t,s)|_C$ and $|W(t,s)|_F$ using the WOIs, which will be described in the next section.

The results from Step 1 for automated traffic event detection and Step 2 for peak identification in the proposed algorithm are discussed in this section. Automated traffic event detection in Step 1 was performed based on the measured cross-frame strain, $F(t)$, to identify impulsive traffic events for robustly extracting the amplitudes for the GM-CWT results. The cross-frame strain, $F(t)$, was used for this purpose because it indirectly captures the traffic loading and has relatively low noise, hence more clear peaks. Subsequently, the peak detection results were used in Step 2 to find the WOIs for effectively extracting peaks in $|W(t,s)|_C$ and $|W(t,s)|_F$ and computing the modified CGI. As mentioned previously, the cross-frame strain has noise and low-frequency drifts, as shown previously in Figure 5.13a and Figure 5.14a. Thus, detrending, high-pass, and low-pass filtering were first utilized to remove the low-frequency drift and high-frequency noise in the $F(t)$ signal prior to peak detection. Utilizing the strain threshold of $h = 30\ \mu\varepsilon$ and minimum peak distance of t_d = 1.3 seconds, the peaks were automatically detected using Step 1 of the proposed algorithm. The filtered signals with the detected peaks (red asterisks) are shown in Figure 5.15 and Figure 5.16 for both data sets.

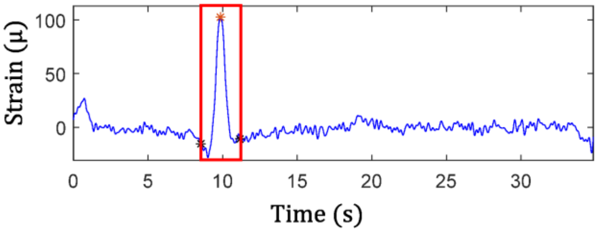

Figure 5.15. Identified traffic events and WOIs from strain, $F(t)$, measurement under a single traffic event

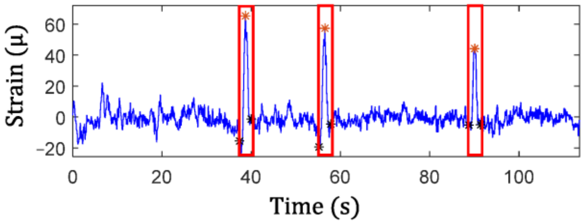

Figure 5.16. Identified traffic events and WOIs from strain, $F(t)$, measurement under (a) single traffic event and (b) multiple traffic events

Subsequently, the WOIs in Step 2 of the algorithm were achieved as $[t_i - t_d, t_i + t_d]$ using the timestamps of the detected peaks, t_i, which are shown in the figures by the red asterisks as well as the rectangular red boxes. The identified WOIs were then applied to the $|W(t,s)|_C$ and $|W(t,s)|_F$ calculated in the previous section to separate the impulsive traffic events and effectively extract $|W(t,s)|_{Ci}^{max}$ and $|W(t,s)|_{Fi}^{max}$ for each event, avoiding the impact of noise and low-frequency drift. The identified WOIs of the $|W(t,s)|_C$ and $|W(t,s)|_F$ are shown in Figure 5.17 and Figure 5.18 for both the single and multiple traffic examples, respectively. Note that the large yellow highlighted regions in the WOIs show the successfully extracted traffic events for $\Delta C(t)$ and $F(t)$.

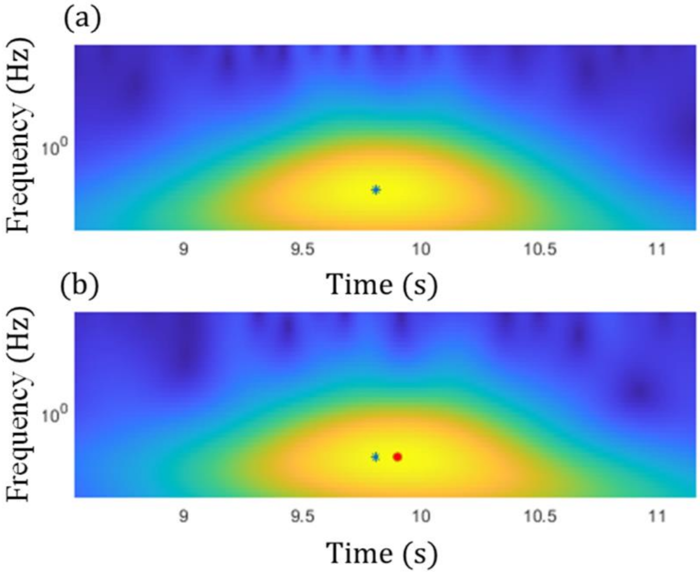

Figure 5.17. Peak identification within the identified WOIs under the single traffic event for (a) strain, $F(t)$, measurement and (b) $\Delta C(t)$ from SEC

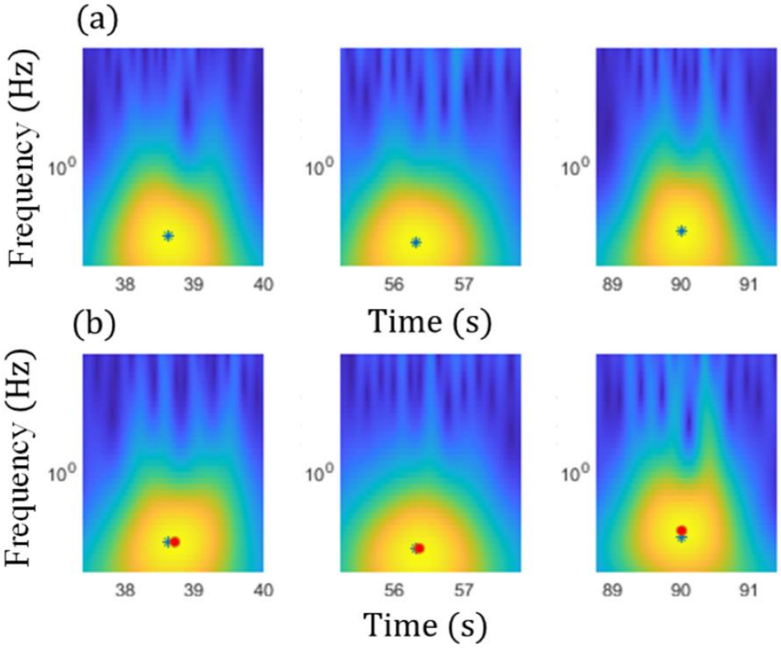

Figure 5.18. Peak identification within the identified WOIs under the multiple traffic events for (a) strain, $F(t)$, measurement and (b) $\Delta C(t)$ from SEC

Based on the WOIs, the $|W(t,s)|_{Ci}^{max}$ and $|W(t,s)|_{Fi}^{max}$ were then extracted within their respective WOIi, and the results are illustrated in the figures. In particular, the blue stars in Figure 5.17a and Figure 5.18a show the $|W(t,s)|_{Fi}^{max}$, which are the maximum peaks in the cross-frame strain, while $||W(t,s)|_{Ci}^{max}$ of $\Delta C(t)$ for Case-1 and Case-2 are shown in blue stars and red dots in Figure 5.17b and Figure 5.18b, respectively. As a result, the modified CGI can be computed for both cases.

The modified CGIs for the selected fatigue crack are presented in this section. Utilizing several acceleration thresholds ranging from 150 mg to 250 mg for event-triggered sensing, data from the bridge were collected using the WLASS from mid-October 2021 to mid-March 2022. A total of 129 data sets were used under the aforementioned strain threshold of $h = 30\ \mu\varepsilon$ and minimum peak distance of t_d = 1.3 seconds defined for peak detection in Step 1 to obtain the modified CGIs, which contain 267 impulse peak events. The modified CGIs for both cases were computed for each impulse peak event using equation 47 based on the WOI. The identified CGIs during the monitoring period for both cases are shown in Figure 5.19. Note that each data point in the figure shows the mean modified CGI, $\overline{\text{CGI}}$, and the associated standard deviation from impulsive traffic events collected during one to two days with a minimum of two events.

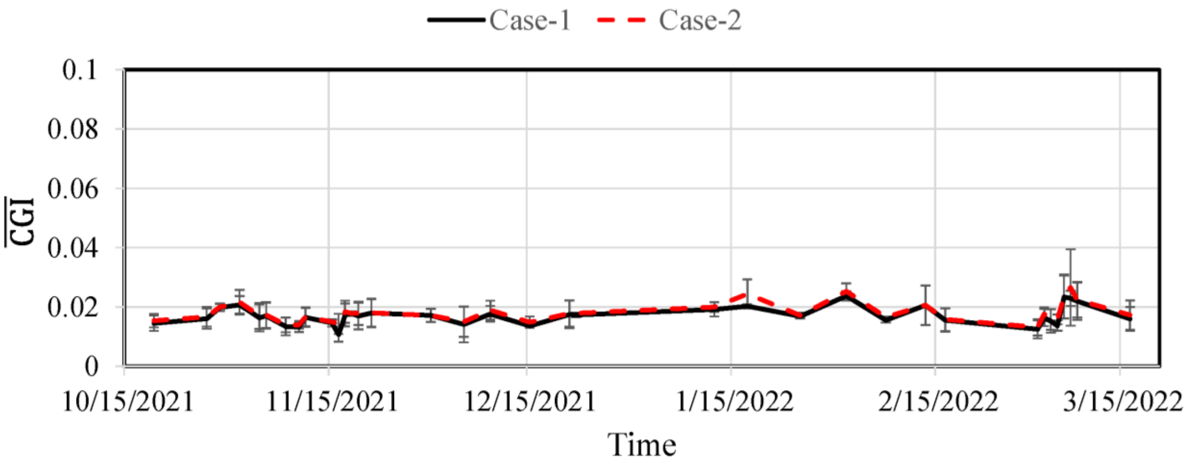

Figure 5.19. Monitored CGI and standard deviation

For both cases, despite some fluctuation possibly attributed to sensor and data acquisition noise and limited data points, the $\overline{\text{CGI}}$ stayed almost constant, indicating that the crack size remained constant during the monitoring period. Moreover, the number of peaks for each $\overline{\text{CGI}}$ data point in Figure 5.19 is shown in Figure 5.20.

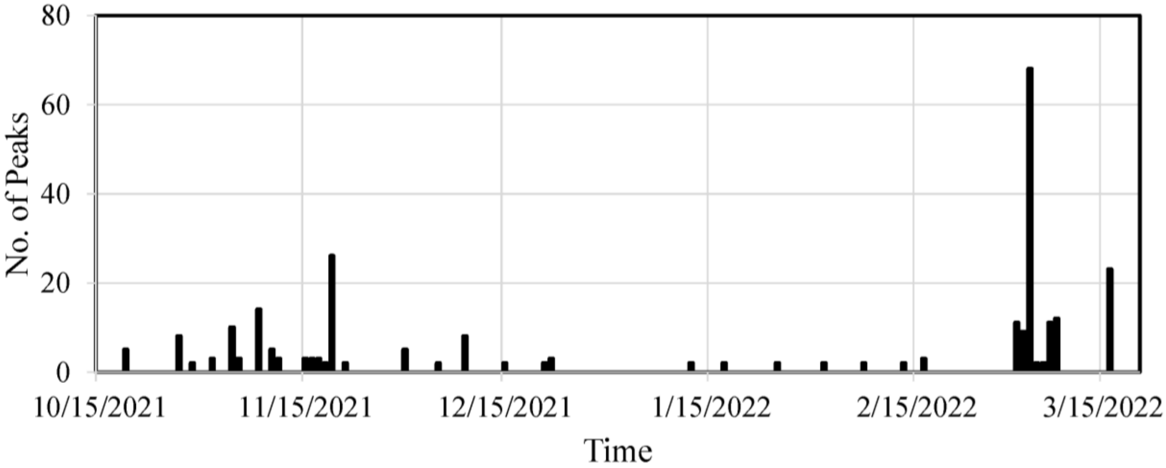

Figure 5.20. Number of peaks for computing the CGI

As shown in the figure, November 19 , 2021; March 4, 2022; and March 16, 2022, recorded the highest number of peaks, including 26, 68, and 23 peaks, respectively. For Case-1, the corresponding $\overline{\text{CGI}}$ values are 0.017, 0.015, and 0.016, respectively, and the standard deviations are 0.0045, 0.004, and 0.004, respectively. For Case-2, the $\overline{\text{CGI}}$ are 0.018, 0.015, and 0.017, respectively, and the standard deviations are 0.004, 0.0035, and 0.005, respectively. Note that those means and standard deviations remained almost constant, indicating no crack growth during the monitoring period.

Final Data Set

The modified CGIs were extracted in the field from mid-October 2021 to mid-March 2024. A total of 168 data sets containing 1,035 impulse events were collected and processed. These CGIs are plotted in Figure 5.21. The field CGIs presented are mean values averaged over one to two days using a minimum of two events. It can be observed that the linear fit of the field CGIs has a positive slope, indicating that the CGIs slightly increased and the fatigue crack propagated further during the monitoring period. Some fluctuations can be attributed to seasonal effects, whereas the magnitude of the crack opening with traffic is expected to vary with the bridge's temperature. This investigation is left to future work. Figure 5.21 also compares the field CGI values against those obtained from the laboratory tests (using a Fourier transform) reported in (Kong et al. 2018), where an array of SECs was used to cover a large fatigue-susceptible region at the bridge girder to cross-frame connection in order to construct a CGI map. The laboratory CGI begins to increase at approximately 7,000 cycles when the crack initiated and then increases linearly with the number of cycles, correlating with crack length. It follows that the field CGI values correspond to an early crack size, as expected. A UT test is planned to detect the crack length covered by the sensor and benchmark the CGI results measured by the cSEC, and we plan to report results in future publications.

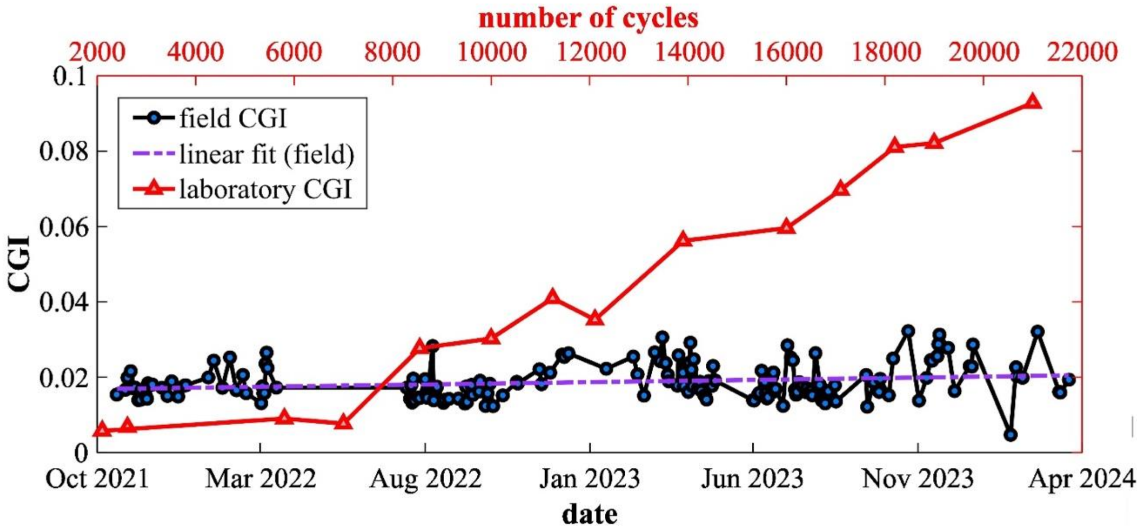

Figure 5.21. Comparison of averaged field CGI with laboratory CGI

Conclusion

This study developed a WLASS and its associated algorithm for fatigue crack monitoring. The WLASS integrates the SEC with the Xnode sensing platform to obtain large-area strain data wirelessly and operates under an event-triggered sensing mode. In particular, the WLASS consists of (1) the SEC; (2) the Xnode wireless smart sensing platform for autonomous trigger-based sensing, wireless data collection, cloud storage, and remote data retrieval; and (3) a capacitive sensor board to interface the SEC with the Xnode for measuring large-area strain. Meanwhile, the developed automated algorithm copes with a large amount of nonstationary field data with numerous impulsive peak events due to traffic loads. The developed algorithm contains an automated traffic event detection, a GM-CWT and peak identification, and a modified CGI for fatigue crack monitoring. A numerical validation was conducted to examine the effectiveness of the GM-CWT of the developed algorithm to extract the peak traffic events. The results indicate that the GM-CWT is more suitable for analyzing nonstationary field traffic-induced signals compared with the traditional Fourier-analysis-based method.

Subsequently, the performance of the developed WLASS and the algorithm was verified through a field deployment on a steel highway bridge in Kansas City, Kansas. Data were collected from mid-October 2021 to mid-March 2022. Peak events due to traffic loadings were successfully identified, and the amplitude information was accurately extracted. Finally, the modified CGIs were obtained using the extracted amplitudes and were presented in terms of mean and standard deviation. As the highest number of daily peaks, 26, 68, and 23 impulsive events were obtained on November 19, 2021; March 4, 2022; and March 16, 2022, respectively. The corresponding $\overline{\text{CGI}}$ were 0.017, 0.015, and 0.016 for Case-1 and 0.018, 0.015, and 0.017 for Case-2, respectively. The mean CGI remained relatively constant during the monitoring period, with a level of fluctuation much lower than that corresponds to actual crack growth observed in the control group based on a large-scale laboratory test, indicating that no crack propagation was detected during the relatively short monitoring period. Future work will be focused on long-term data analysis for fatigue crack monitoring using the WLASS.

CHAPTER 6: CONCLUSION

This report presented the research findings and outcomes from the pooled fund project TPF-5(449): Robust Wireless Skin Sensor Networks for Long-Term Fatigue Crack Monitoring of Bridges (Phase I). The report comprised five chapters, which included an introduction to fatigue crack monitoring on steel bridges, sensing skin technology, laboratory characterization of the sensing skin, development of the wireless capacitive sensing board, and field validation of WLASS.

Chapter 1 focused on a literature review and discussion of the issue of fatigue damage in steel highway bridges in the United States and the challenges associated with fatigue detection and inspection. The state-of-the-art fatigue crack sensing technologies and their limitations were also reviewed, and the research objectives of this project were listed.

Chapter 2 focused on the sensing skin technology and the technological updates that were required to enable the field deployment of a sensing skin for fatigue crack discovery and monitoring. The fabrication process and electromechanical model of a cSEC, multifunctional soft stretchable strain sensor, an electrically isolated SEC, and a printable cSEC were presented. The cSEC is an updated version of the SEC that improved signal stability and sensitivity in order to facilitate field implementation. The multifunctional soft stretchable strain sensor combined optical and capacitive sensing properties through sandwiching a stretchable structural color film between two transparent CNT electrodes. The electrically isolated SEC was engineered by adding an extended polymer matrix of SEBS on both sides of the SEC sensor to act as an integrated isolation layer that minimized capacitance coupling between the SEC and concrete. The printable cSEC was fabricated using a commercial room-temperature-vulcanizing silicone, thus eliminating the need for epoxy to ensure reliable bonding during sensor deployment.

Chapter 3 focused on laboratory characterization of the sensing skin technology. The general sensing performance of the cSEC and the multifunctional soft stretchable strain sensor in terms of linearity, sensitivity, resolution, and accuracy were characterized and evaluated through a series fatigue crack tests conducted on small scale C(T) specimens. It was also found that adding a texture resulted in an overall 69% to 100% increase in gauge factor, 35% to 113% increase in linearity, 222% to 319% increase in the resolution, and 111% to 582% increase in stability compared to untextured SECs. The multifunctional soft stretchable strain sensor combined optical and electrical sensing properties, in which the optical response is to assist inspections while the electrical feedback is to send advance warnings of possible damage. The cSEC was applied to measure angular motion in steel components by deploying the sensor in a folded configuration, yielding an accuracy of 0.416°. The cSEC was also applied to discover and monitor the fatigue crack on fillet welds, and a minimum detectable crack length of 0.48 mm was found through conducting t-tests on the CGI_i^c.

Chapter 4 focused on development of the wireless capacitive sensing board. We developed a fully automated c-strain sensor board for wireless SHM applications, which can interface with the Xnode wireless sensor platform to be used under its 3.3 V power for a measurement range of 0 to 2.4 V. While keeping the basic capacitance measurement framework of the analog c-strain sensor board, a low-cost microcontroller-based automated AC bridge balancing, amplification, and shunt calibration method was developed. In particular, peak-detection circuits and a 16-bit ADC were employed to read the peak voltages of the high-frequency AC signals. DPs, a digital bus switch, and an 8-bit microcontroller were employed to control the AC bridge balancing, signal amplification, and two-step shunt calibration. Embedded software was developed for automated control of the digital components. A prototype of the new sensor board was produced, and the performance was validated via laboratory tests and compared with a commercial wired capacitance measurement system, exhibiting about 34% lower measurement noise.

Chapter 5 focused on field validation of the WLASS. Challenges in field deployment were presented. Importantly, a method had to be developed to assess field performance. We validated the integrated monitoring system through a field deployment on a steel highway bridge. The dedicated DAQ system included a data readout circuit paired with an Xnode for wireless transmission. Data collected in the field showed that the wireless crack monitoring system is capable of collecting data continuously and autonomously from the cSEC and the strain gauge under traffic loading. The data fusion algorithm, GM-CWT, was developed by using a CWT instead of a Fourier transform to detect and isolate vehicular events and improve robustness with respect to noise. By processing the raw measurements using the developed algorithm, fatigue damage and its propagation on steel bridges can be accurately monitored and analyzed over a long time. The linear fit of the field CGI values was found to have a positive slope, indicating that the CGI values slightly increased and the fatigue crack propagated further during the monitoring period. The comparison of field CGI and laboratory CGI showed good agreement and thus demonstrated the success of the field deployment.

Results obtained at the end of this project showed that the developed wireless sensing skin system is a robust and effective solution for long-term fatigue crack monitoring on steel bridges. This outcome fulfilled the overarching objective of the proposed project, which addressed essential development needs uncovered during previous research to achieve more robust, accurate, and flexible crack monitoring using the wireless skin sensor network. The combination of the cSEC technology, automated wireless data acquisition, and intelligent fatigue crack monitoring algorithms provided reliable and accurate detection of fatigue cracks. The field implementation confirmed the system’s capability to operate continuously and autonomously in real-world conditions and to successfully detect and monitor fatigue damage.

This project has demonstrated the potential of this health monitoring system to enhance the safety and longevity of steel bridges by enabling early detection and timely maintenance of fatigue cracks. Future work will focus on commercializing the technology, developing another round of important updates to enable the production of large sensing sheets with integrated flexible electronics, exploring additional field deployments, and potentially integrating this system into broader structural health monitoring programs for infrastructure.

REFERENCES

Ahmed, S., T. Schumacher, E. T. Thostenson, and J. McConnell. 2020. Performance Evaluation of a Carbon Nanotube Sensor for Fatigue Crack Monitoring of Metal Structures. *Sensors*, Vol. 20, No., 16, Article no. 4383.

Allen, R. J., G. S. Booth, and T. Jutla. 1988. A Review of Fatigue Crack Growth Characterization by Linear Elastic Fracture Mechanics (LEFM). Part II—Advisory Documents and Applications within National Standards. *Fatigue & Fracture of Engineering Materials & Structures*, Vol. 11, No. 2, pp.71–108.

Alshoaibi, A. M. and O. Yasin. 2021. Finite Element Simulation of Crack Growth Path and Stress Intensity Factors Evaluation in Linear Elastic Materials. *Journal of Computational & Applied Research in Mechanical Engineering (JCARME)*, Vol. 11, No. 1, pp.139–149.

Amiri, N., G. H. Farrahi, K. R. Kashyzadeh, and M. Chizari. 2020. Applications of Ultrasonic Testing and Machine Learning Methods to Predict the Static & Fatigue Behavior of Spot-Welded Joints. *Journal of Manufacturing Processes*, Vol. 52, pp. 26–34.

ARTBA. 2020. *Bridge Report*. American Road and Transportation Builders Association, Washington, DC. https://artbabridgereport.org/.

ASCE. 2021. *Report Card for America's Infrastructure*. American Society of Civil Engineers, Reston, VA. https://infrastructurereportcard.org/.

Aygun, L. E., V. Kumar, C. Weaver, M. Gerber, S. Wagner, N. Verma, B. Glisic, and J. C. Sturm. 2020. Large-Area Resistive Strain Sensing Sheet for Structural Health Monitoring. *Sensors*, Vol. 20, No. 5, Article no. 1386.

Behera, A. 2022. Chapter 5. Chromogenic Materials. In *Advanced Materials*. Springer International Publishing, New York, NY.

Berglund, E. M. and A. E. Schultz. 2006. Girder Differential Deflection and Distortion-Induced Fatigue in Skewed Steel Bridges. *Journal of Bridge Engineering*, Vol. 11, No. 2, pp. 169–177.

Broek, D. 2012. *The Practical Use of Fracture Mechanics*. Springer Dordrecht, Berlin, Germany.

Brooks, A. C., X. Zhao, and T. N. Pappas. 2008. Structural Similarity Quality Metrics in a Coding Context: Exploring the Space of Realistic Distortions. *IEEE Transactions on Image Processing*, Vol. 17, No. 8, pp. 1261–1273.

Burton, A. R., J. P. Lynch, M. Kurata, and K. H. Law. 2017. Fully Integrated Carbon Nanotube Composite Thin Film Strain Sensors on Flexible Substrates for Structural Health Monitoring. *Smart Materials and Structures*, Vol. 26, No. 9.

Cai, L., L. Song, P. Luan, Q. Zhang, N. Zhang, Q. Gao, D. Zhao, X. Zhang, M. Tu, F. Yang, W. Zhou, Q. Fan., J. Luo, W. Zhou, P. M. Ajayan, and S. Xie. 2013. Super-Stretchable, Transparent Carbon Nanotube-Based Capacitive Strain Sensors for Human Motion Detection. *Scientific Reports*, Vol. 3, Article no. 3048.

Campbell, L. E., R. J. Connor, J. M. Whitehead, and G. A. Washer. 2020. Benchmark for Evaluating Performance in Visual Inspection of Fatigue Cracking in Steel Bridges. *Journal of Bridge Engineering*, Vol. 25, No. 1.

Campbell, L. E., R. J. Connor, J. M. Whitehead, and G. A. Washer. 2021. Human Factors Affecting Visual Inspection of Fatigue Cracking in Steel Bridges. *Structure and Infrastructure Engineering*, Vol. 17, No. 11, pp. 1447–1458.

Casas, J. R. and P. J. S. Cruz. 2003. Fiber Optic Sensors for Bridge Monitoring. *Journal of Bridge Engineering*, Vol. 8, No. 6, pp. 362–373.

Chai, M., J. Zhang, Z. Zhang, Q. Duan, and G. Cheng. 2017. Acoustic Emission Studies for Characterization of Fatigue Crack Growth in 316LN Stainless Steel and Welds. *Applied Acoustics*, Vol. 126, pp. 101–113.

Chen, H., Y. Song, X. Cheng, and H. Zhang. 2019. Self-Powered Electronic Skin Based on the Triboelectric Generator. *Nano Energy*, Vol. 56, pp. 252–268.

Cohen, A. J., M. Kollosche, M. C. Yuen, D.-Y. Lee, D. R. Clarke, and R. J. Wood. 2022. Batch-Sprayed and Stamp-Transferred Electrodes: A New Paradigm for Scalable Fabrication of Multilayer Dielectric Elastomer Actuators. *Advanced Functional Materials*, Vol. 32, No. 43, Article no. 2205394.

Dai, H., E. T. Thostenson, and T. Schumacher. 2015. Processing and Characterization of a Novel Distributed Strain Sensor Using Carbon Nanotube-Based Nonwoven Composites. *Sensors*, Vol. 15, No. 7, pp. 17728–17747.

Dellenbaugh, L., X. Kong, H. Al-Salih, W. Collins, C. Bennett, J. Li, and E. J. Sutley. 2020. Development of a Distortion-Induced Fatigue Crack Characterization Methodology Using Digital Image Correlation. *Journal of Bridge Engineering*, Vol. 25, No. 9.

Dong. X, C. J. Taylor, and T. F. Cootes. 2021. A Random Forest-Based Automatic Inspection System for Aerospace Welds in X-Ray Images. *IEEE Transactions on Automation Science and Engineering*, Vol. 18, No. 4, pp. 2128–2141.

Downey, A., A. L. Pisello, E. Fortunati, C. Fabiani, F. Luzi, L. Torre, F. Ubertini, and S. Laflamme. 2019. Durability and Weatherability of a Styrene-Ethylene-Butylene-Styrene (SEBS) Block Copolymer-Based Sensing Skin for Civil Infrastructure Applications. *Sensors and Actuators A: Physical*, Vol. 293, pp. 269–280.

Farmer, F. M. 1921. The Desirability of Standardization in the Testing of Welds. *Proceedings of the Institution of Mechanical Engineers*, Vol. 100, No.1, pp. 225–288.

Fu, Y., T. Hoang, K. Mechitov, J. R. Kim, D. Zhang, and B. F. Spencer, Jr. 2018. Sudden Event Monitoring of Civil Infrastructure Using Demand-Based Wireless Smart Sensors. *Sensors*, Vol. 18, No.12, Article no. 4480.

Fu. Y, K. Mechitov, T. Hoang, J. R. Kim, D. H. Lee, and B. F. Spencer, Jr. 2019. Development and Full-Scale Validation of High-Fidelity Data Acquisition on a Next-Generation Wireless Smart Sensor Platform. *Advances in Structural Engineering*, Vol. 22, No. 16, pp. 3512–3533.

Gadallah, R., N. Osawa, S. Tanaka, and S. Tsutsumi. 2018. Critical Investigation on the Influence of Welding Heat Input and Welding Residual Stress on Stress Intensity Factor and Fatigue Crack Propagation. *Engineering Failure Analysis*, Vol. 89, pp. 200–221.

Geathers. J, C. J. Torbet. J. W. Jones, and S. Daly. 2015. Investigating Environmental Effects on Small Fatigue Crack Growth in Ti–6242S Using Combined Ultrasonic Fatigue and Scanning Electron Microscopy. *International Journal of Fatigue*, Vol. 70, pp. 154–162.

Glišić, B., Y. Yao, S.-T. E. Tung, S. Wagner, J. C. Sturm, and N. Verma. 2016. Strain Sensing Sheets for Structural Health Monitoring Based on Large-Area Electronics and Integrated Circuits. *Proceedings of the IEEE*, Vol. 104, No. 8, pp. 1513–1528.

Gonchar, A. V., V. A. Klyushnikov, V. V. Mishakin, and M. S. Anosov. 2021. Ultrasonic and Eddy-Current Fatigue Monitoring of Austenitic Steel Welded Joints. *Russian Journal of Nondestructive Testing*, Vol. 57, pp. 570–578.

Gupta, S., Y.-A. Lin, H.-J. Lee, J. Buscheck, R. Wu, J. P. Lynch, N. Garg, and K. J. Loh. 2021. In Situ Crack Mapping of Large-Scale Self-Sensing Concrete Pavements Using Electrical Resistance Tomography. *Cement and Concrete Composites*, Vol. 122, Article no. 104154.

Haagensen, P. J. and S. J. Maddox. 2013. *IIW Recommendations on Methods for Improving the Fatigue Strength of Welded Joints: IIW-2142-10*. Woodhead Publishing, Sawston, Cambridge, United Kingdom.

Hoang, T., Y. Fu, K. Mechitov, F. G. Sánchez, J. R. Kim, D. Zhang, and B. F. Spencer, Jr. 2020. Autonomous End-to-End Wireless Monitoring System for Railroad Bridges. *Advances in Bridge Engineering*, Vol. 1, No. 17.

Holmberg, P. 1995. Automatic Balancing of Linear AC Bridge Circuits for Capacitive Sensor Elements. *IEEE Transactions on Instrumentation and Measurement*, Vol. 44, No. 3, pp. 803–805.

Jajich, D. and A. E. Schultz. 2003. Measurement and Analysis of Distortion-Induced Fatigue in Multigirder Steel Bridges. *Journal of Bridge Engineering*, Vol. 8, No. 2, pp. 84–91.

Jang, S., H. Jo, S. Cho, K. Mechitov, J. A. Rice, S.-H. Sim, H.-J. Jung, C.-B. Yun, B. F. Spencer, Jr., and G. Agha. 2010. Structural Health Monitoring of a Cable-Stayed Bridge Using Smart Sensor Technology: Deployment and Evaluation. *Smart Structures and Systems*, Vol. 6, No. 5–6, pp. 439–459.

Jeong, J.-H., J. Xu, H. Jo, J. Li, X. Kong, W. Collins, C. Bennett, and S. Laflamme. 2018a. Capacitance-Based Wireless Strain Sensor Development. *Proceedings SPIE Vol. 10598: Sensors and Smart Structures Technologies for Civil, Mechanical, and Aerospace Systems 2018*, March 27, Denver, Colorado.

Jeong, J.-H., J. Xu, H. Jo, J. Li, X. Kong, W. Collins, C. Bennett, and S. Laflamme. 2018b. Development of Wireless Sensor Node Hardware for Large-Area Capacitive Strain Monitoring. *Smart Materials and Structures*, Vol. 28, No. 1.

Jo, H., J. W. Park, B. F. Spencer, and H. J. Jung. 2013. Development of High-Sensitivity Wireless Strain Sensor for Structural Health Monitoring. *Smart Structures and Systems*, Vol. 11, No. 5, pp. 477–496.

Kong, X. and J. Li. 2019. Non-Contact Fatigue Crack Detection in Civil Infrastructure through Image Overlapping and Crack Breathing Sensing. *Automation in Construction*, Vol. 99, pp. 125–139.

Kong, X., J. Li, C. Bennett, W. Collins, and S. Laflamme. 2016. Numerical Simulation and Experimental Validation of a Large-Area Capacitive Strain Sensor for Fatigue Crack Monitoring. *Measurement Science and Technology*, Vol. 27, No. 12.

Kong, X., J. Li, W. Collins, C. Bennett, S. Laflamme, and H. Jo. 2017a. A Robust Signal Processing Method for Quantitative High-Cycle Fatigue Crack Monitoring Using Soft Elastomeric Capacitor Sensors. *Proceedings SPIE Vol. 10168: Sensors and Smart Structures Technologies for Civil, Mechanical, and Aerospace Systems 2017*, April 12, Portland, Oregon.

Kong, X., J. Li, W. Collins, C. Bennett, S. Laflamme, and H. Jo. 2017b. A Large-Area Strain Sensing Technology for Monitoring Fatigue Cracks in Steel Bridges. *Smart Materials and Structures*, Vol. 26, No. 8.

Kong, X., J. Li. W. Collins, C. Bennett, S. Laflamme, and H. Jo. 2018. Sensing Distortion-Induced Fatigue Cracks in Steel Bridges with Capacitive Skin Sensor Arrays. *Smart Materials and Structures*, Vol. 27, No. 11.

Kong, X., J. Li, C. Bennett, W. Collins, S. Laflamme, and H. Jo. 2019. Thin-Film Sensor for Fatigue Crack Sensing and Monitoring in Steel Bridges under Varying Crack Propagation Rates and Random Traffic Loads. *Journal of Aerospace Engineering*, Vol. 32, No. 1.

Kowalski, M. and D. Rozumek. 2019. Numerical Simulation of Fatigue Crack Growth in Steel-Aluminium Transition Joint. *Proceedings of the International Conference of Computational Methods in Sciences and Engineering 2019 (ICCMSE-2019)*, Vol. 2186, No. 1, May 1–5, Rhodes, Greece.

Kumar, R. 1992. Review on Crack Closure for Constant Amplitude Loading in Fatigue. *Engineering Fracture Mechanics*, Vol. 42, No. 2, pp. 389–400.

Kumar, R. and V. Moyal. 2013. Visual Image Quality Assessment Technique Using FSIM. *International Journal of Computer Applications Technology and Research*, Vol. 2, No. 3, pp. 250–254.

Kumar, V., B. Acot, L. E. Aygun, S. Wagner, N. Verma, J. Sturm, and B. Glisic. 2021. Detecting, Localizing, and Quantifying Damage Using Two-Dimensional Sensing Sheet: Lab Test and Field Application, *Journal of Civil Structural Health Monitoring*, Vol. 11, pp. 1055–1075.

Kurnyta, A., K. Kowalczyk, M. Baran, M. Dziendzikowski, and K. Dragan. 2021. The Use of Silver Conductive Paint for Crack Propagation Sensor Customization. *2021 IEEE 8th International Workshop on Metrology for AeroSpace (MetroAeroSpace)*, June 23–25, Naples, Italy.

Laflamme, S., H. S. Saleem, B. K. Vasan, R. L. Geiger, D. J. Chen, M. R. Kessler, and K. Rajan. 2013. Soft Elastomeric Capacitor Network for Strain Sensing over Large Surfaces. *IEEE/ASME Transactions on Mechatronics*, Vol. 18, No. 6, pp. 1647–1654.

Li, Z., X. Jiang, and H. Hopman. 2020. Surface Crack Growth in Offshore Metallic Pipes under Cyclic Loads: A Literature Review. *Journal of Marine Science and Engineering*, Vol. 8, No. 5, Article no. 339.

Lilly, J. M. and S. C. Olhede. 2009. Higher-Order Properties of Analytic Wavelets. *IEEE Transactions on Signal Processing*, Vol. 57, No. 1, pp. 146–160.

Lilly, J. M. and S. C. Olhede. 2012. Generalized Morse Wavelets as a Superfamily of Analytic Wavelets. *IEEE Transactions on Signal Processing*, Vol. 60, No. 11, pp. 6036–6041.

Lin, Y.-A., Y. Zhao, L. Wang, Y. Park, Y.-J. Yeh, W.-H. Chiang, and K. J. Loh. 2021. Graphene K-Tape Meshes for Densely Distributed Human Motion Monitoring. *Advanced Materials Technologies*, Vol. 6, No. 1.

Liu, H., J. Yan, M. Kollosche, S. A. Bentil, and S. Laflamme. 2020a. Surface Textures for Stretchable Capacitive Strain Sensors. *Smart Materials and Structures*, Vol. 29, No. 10.

Liu, H., M. Kollosche, J. Yan, E. M. Zellner, S. A. Bentil, I. V. Rivero, C. Wiersema, and S. Laflamme. 2020b. Numerical Investigation of Auxetic Textured Soft Strain Gauge for Monitoring Animal Skin. *Sensors*, Vol. 20, No. 15, Article no. 4185.

Liu, H., S. Laflamme, J. Li, C. Bennett, W. N. Collins, A. Downey, P. Ziehl, and H. Jo. 2021a. Soft Elastomeric Capacitor for Angular Rotation Sensing in Steel Components. *Sensors*, Vol. 21, No. 21, Article No. 7017.

Liu, H., S. Laflamme, J. Li, C. Bennett, W. Collins, A. Downey, P. Ziehl, and H. Jo. 2021b. Investigation of Surface Textured Sensing Skin for Fatigue Crack Localization and Quantification. *Smart Materials and Structures*, Vol. 30, No. 10.

Liu, P., H. J. Lim, S. Yang, H. Sohn, C. H. Lee, Y. Yi, D. Kim, J. Jung, and I.-H. Bae. 2017. Development of a "Stick-and-Detect" Wireless Sensor Node for Fatigue Crack Detection. *Structural Health Monitoring*, Vol. 16, No. 2, pp. 153–163.

Lu, H., P. Dong, and S. Boppudi. 2015. Strength Analysis of Fillet Welds under Longitudinal and Transverse Shear Conditions. *Marine Structures*, Vol. 43, pp. 87–106.

MATLAB. 2021. *Version 9.10.0.1602886 (R2021a)*. The MathWorks Inc., Natick, Massachusetts.

Mantenuto, P., A. D. Marcellis, and G. Ferri. 2014. Novel Modified De-Sauty Autobalancing Bridge-Based Analog Interfaces for Wide-Range Capacitive Sensor Applications. *IEEE Sensors Journal*, Vol. 14, No. 5, pp. 1664–1672.

Mahmoud, H. N. and P. A. Miller. 2016. Distortion-Induced Fatigue Crack Growth. *Journal of Bridge Engineering*, Vol. 21, No. 2.

Matysek, M., P. Lotz, K. Flittner, and H. F. Schlaak. 2008. High-Precision Characterization of Dielectric Elastomer Stack Actuators and Their Material Parameters. *Proceedings SPIE Vol. 6927: Electroactive Polymer Actuators and Devices (EAPAD) 2008*, April 10, San Diego, California.

Mikulski, Z. and T. Lassen. 2019. Fatigue Crack Initiation and Subsequent Crack Growth in Fillet Welded Steel Joints. *International Journal of Fatigue*, Vol. 120, pp. 303–318.

Minardo, A., R. Bernini, L. Amato, and L. Zeni. 2012, Bridge Monitoring Using Brillouin Fiber-Optic Sensors. *IEEE Sensors Journal*, Vol. 12, No. 1, pp. 145–150.

Mottershead, J. E., M. Link, and M. I. Friswell. 2011. The Sensitivity Method in Finite Element Model Updating: A Tutorial. *Mechanical Systems and Signal Processing*, Vol. 25, No. 7, pp. 2275–2296.

Newby, M. 1991. Estimation of Paris-Erdogan Law Parameters and the Influence of Environmental Factors on Crack Growth. *International Journal of Fatigue*, Vol. 13, No. 4, pp. 291–301.

Oh, S. H., T. Y. Ryu, S. H. Park, M. G. Won, S. J. Kang, K. S. Lee, S. H. Lee, M. K. Kim, and J. B. Choi. 2015. Evaluation of J-Groove Weld Residual Stress and Crack Growth Rate of PWSCC in Reactor Pressure Vessel Closure Head. *Journal of Mechanical Science and Technology*, Vol. 29, pp. 1225–1230.

Olhede, S. C. and A. T. Walden. 2002. Generalized Morse Wavelets. *IEEE Transactions on Signal Processing*, Vol. 50, No. 11, pp. 2661–2670.

Pakzad, S. N., G. L. Fenves, S. Kim, and D. E. Culler. 2008. Design and Implementation of Scalable Wireless Sensor Network for Structural Monitoring. *Journal of Infrastructure Systems*, Vol. 14, No. 1, pp. 89–101.

Pasadas, F. and D. Jiménez. 2016. Large-Signal Model of Graphene Field-Effect Transistors—Part I: Compact Modeling of GFET Intrinsic Capacitances. *IEEE Transactions on Electron Devices*, Vol. 63, No. 7, pp. 2936–2941.

Pascoe, J. A., D. S. Zarouchas, R. C. Alderliesten, and R. Benedictus. 2018. Using Acoustic Emission to Understand Fatigue Crack Growth within a Single Load Cycle. *Engineering Fracture Mechanics*, Vol. 194, pp. 281–300.

Peng, J., C. Shi, E. Laugeman, W. Hu, Z. Zhang, S. Mutic, and B. Cai. 2020. Implementation of the Structural SIMilarity (SSIM) Index as a Quantitative Evaluation Tool for Dose Distribution Error Detection. *Medical Physics*, Vol. 47, No. 4, pp. 1907–1919.

Pugno, N., M. Ciavarella, P. Cornetti, and A. Carpinteri. 2006. A Generalized Paris' Law for Fatigue Crack Growth. *Journal of the Mechanics and Physics of Solids*, Vol. 54, No. 7, pp. 1333–1349.

Ren. F., C. Zhu, and M. He. 2020. Moment Tensor Analysis of Acoustic Emissions for Cracking Mechanisms during Schist Strain Burst. *Rock Mechanics and Rock Engineering*, Vol. 53, pp. 153–170.

Ritchie, R. O. 1999. Mechanisms of Fatigue-Crack Propagation in Ductile and Brittle Solids. *International Journal of Fracture*, Vol. 100, pp. 55–83.

Roy, G., B. Panigrahi, and G. Pohit. 2021. Crack Identification in Beam-Type Structural Elements Using a Piezoelectric Sensor. *Nondestructive Testing and Evaluation*. Vol. 36, No. 6, pp. 597–615.

Sakagami, T., Y. Izumi, D. Shiozawa, T. Fujimoto, Y. Mizokami, and T. Hanai. 2016. Nondestructive Evaluation of Fatigue Cracks in Steel Bridges Based on Thermoelastic Stress Measurement. *Procedia Structural Integrity*, Vol. 2, pp. 2132–2139.

Sánchez-Romate, X. F., C. Sbarufatti, M. Sánchez, A. Bernasconi, D. Scaccabarozzi, F. Libonati, S. Cinquemani, A. Güemes, and A. Ureña. 2020. Fatigue Crack Growth Identification in Bonded Joints by Using Carbon Nanotube Doped Adhesive Films. *Smart Materials and Structures*, Vol. 29, No. 3.

Sara, U., M. Akter, and M. S. Uddin. 2019. Image Quality Assessment through FSIM, SSIM, MSE and PSNR—A Comparative Study. *Journal of Computer and Communications*, Vol. 7, No. 3, pp. 8–18.

Servetti, G. and X. Zhang. 2009. Predicting Fatigue Crack Growth Rate in a Welded Butt Joint: The Role of Effective *R* Ratio in Accounting for Residual Stress Effect. *Engineering Fracture Mechanics*, Vol. 76, No. 11, pp. 1589–1602.

Skov, A. L. and L. Yu. 2018. Optimization Techniques for Improving the Performance of Silicone-Based Dielectric Elastomers. *Advanced Engineering Material*, Vol. 20, No. 5, Article no. 1700762.

Solob, A., A. Grbović, Ž. Božić, and S. A. Sedmak. 2020. XFEM Based Analysis of Fatigue Crack Growth in Damaged Wing-Fuselage Attachment Lug. *Engineering Failure Analysis*, Vol. 112, Article no.104516.

Spencer, Jr., B. F., J.-W. Park, K. A. Mechitov, H. Jo, and G. Agha. 2017. Next Generation Wireless Smart Sensors toward Sustainable Civil Infrastructure. *Procedia Engineering*, Vol. 171, pp. 5–13.

Spencer, Jr., B. F., M. E. Ruiz-Sandoval, and N. Kurata. 2004. Smart Sensing Technology: Opportunities and Challenges. *Structural Control and Health Monitoring*, Vol. 11, No. 4, pp. 349–368.

Stoyanov, H., M. Kollosche, S. Risse, D. N. McCarthy, and G. Kofod. 2011. Elastic Block Copolymer Nanocomposites with Controlled Interfacial Interactions for Artificial Muscles with Direct Voltage Control. *Soft Matter*, Vol. 7, No. 1, pp. 194–202.

Sun, J., B. Bhushan, and J. Tong. 2013. Structural Coloration in Nature. *RSC Advances*, Vol. 3 No. 35, pp. 14862–14889.

Taher, S. A., J. Li, and H. Fang. 2021. Earthquake Input and State Estimation for Buildings Using Absolute Floor Accelerations. *Earthquake Engineering & Structural Dynamics*, Vol. 50, No. 4, pp. 1020–1042.

Tikka, J., R. Hedman, and A. Siljander. 2003. Strain Gauge Capabilities in Crack Detection. *4th International Workshop on Structural Health Monitoring*, September 15–17, Stanford, California.

Wang, T., B. Tan, M. Lu, Z. Zhang, and G. Lu. 2020. Piezoelectric Electro-Mechanical Impedance (EMI) Based Structural Crack Monitoring. *Applied Sciences*, Vol. 10, No. 13, Article no. 4648.

Wang, Y., S. Hu, T. Xiong, Y. Huang, and L. Qiu. 2022. Recent Progress in Aircraft Smart Skin for Structural Health Monitoring. *Structural Health Monitoring*, Vol. 21, No. 5, pp. 2453–2480.

Wen, S. and D. D. L. Chung. 2004. Electromagnetic Interference Shielding Reaching 70 dB in Steel Fiber Cement. *Cement and Concrete Research*, Vol. 34, No. 2, pp. 329–332.

Wu, S. C., C. Yu, P. S. Yu, J. Y. Buffière, L. Helfen, and Y. N. Fu. 2016. Corner Fatigue Cracking Behavior of Hybrid Laser AA7020 Welds by Synchrotron X-Ray Computed Microtomography. *Materials Science and Engineering: A*, Vol. 651, pp. 604–614.

Yan, J., A. Downey, A. Cancelli, S. Laflamme, A. Chen, J. Li, and F. Ubertini. 2019. Concrete Crack Detection and Monitoring Using a Capacitive Dense Sensor Array. *Sensors*, Vol. 19, No. 8, Article no. 1843.

Yao, Y. and B. Glisic, B. 2015. Detection of Steel Fatigue Cracks with Strain Sensing Sheets Based on Large Area Electronics. *Sensors*, Vol. 15, No. 4, pp. 8088–8108.

Yu, J., P. Ziehl, B. Zárate, and J. Caicedo. 2011. Prediction of Fatigue Crack Growth in Steel Bridge Components Using Acoustic Emission. *Journal of Constructional Steel Research*, Vol. 67, No. 8, pp. 1254–1260.

Yu, J., P. Ziehl, F. Matta, and A. Pollock. 2013. Acoustic Emission Detection of Fatigue Damage in Cruciform Welded Joints. *Journal of Constructional Steel Research*, Vol. 86, pp. 85–91.

Yu, L., Z. Tian, P. Ziehl, and M. ElBatanouny. 2016. Crack Detection and Evaluation in Grout Structures with Passive/Active Methods. *Journal of Materials in Civil Engineering*, Vol. 28, No. 4.

Yue, Y. and J. P. Gong. 2015. Tunable One-Dimensional Photonic Crystals from Soft Materials. *Journal of Photochemistry and Photobiology C: Photochemistry Reviews*, Vol. 23, pp. 45–67.

Zolfaghari, A., A. Zolfaghari, and F. Kolahan. 2018. Reliability and Sensitivity of Magnetic Particle Nondestructive Testing in Detecting the Surface Cracks of Welded Components. *Nondestructive Testing and Evaluation*, Vol. 33, No. 3, pp. 290–300.

THE INSTITUTE FOR TRANSPORTATION IS THE FOCAL POINT FOR TRANSPORTATION AT IOWA STATE UNIVERSITY.

InTrans centers and programs perform transportation research and provide technology transfer services for government agencies and private companies;

InTrans contributes to Iowa State University and the College of Engineering's educational programs for transportation students and provides K–12 outreach; and

InTrans conducts local, regional, and national transportation services and continuing education programs.

INSTITUTE FOR TRANSPORTATION

IOWA STATE UNIVERSITY

Visit **InTrans.iastate.edu** for color pdfs of this and other research reports.